Single Molecule Microscopy

Investigations of Highly Oriented Mesoporous Silica Channels, Photophysics of New Fluorescent Rylene Derivatives and Synchronous Emission on Silver Nanowires

Eva Melari Davies

aus

München, Deutschland

2013

Erklärung

Diese Dissertation wurde im Sinne von §7 der Promotionsordnung vom 28. November 2011 von Herrn Prof. Dr. Christoph Bräuchle betreut.

Eidesstattliche Versicherung

Diese Dissertation wurde eigenständig und ohne unerlaubte Hilfe erarbeitet.

München, den 06.06.2013

————————————————-

Eva Melari Davies

Dissertation eingereicht am	13.06.2013
1. Gutachter:	Prof. Dr. Christoph Bräuchle
2. Gutachter:	Prof. Dr. Jens Michaelis
Mündliche Prüfung am	23.07.2013

Summary

Single-molecule spectroscopy (SMS) and microscopy (SMM) were successfully used to perform studies in three different topics: First, the photophysical properties of new rylene derivatives were characterized regarding their applications in single-molecule studies and membrane labeling. Second, the behavior of dye molecules incorporated as guests into the channels of a highly ordered mesoporous silica material (host-guest material) were investigated. And third, the unique optical properties of silver nanowires, which are caused by the collective oscillation of free electrons, were investigated by using correlated wide-field fluorescence and transmission electron microscopy.

The results of the three main topics in this thesis are summarized as follows:

Highly Fluorescent Water-Soluble Rylene Derivatives: Single-Molecule Studies of Photophysical Properties and Applications for Membrane Labeling

New photostable rylene dyes for applications in single-molecule studies and membrane labeling have been synthesized in the group of Prof. Klaus Müllen (Mainz) and their photophysical properties were characterized in our laboratory. Three of the dyes differ in the number of polyethylene glycol
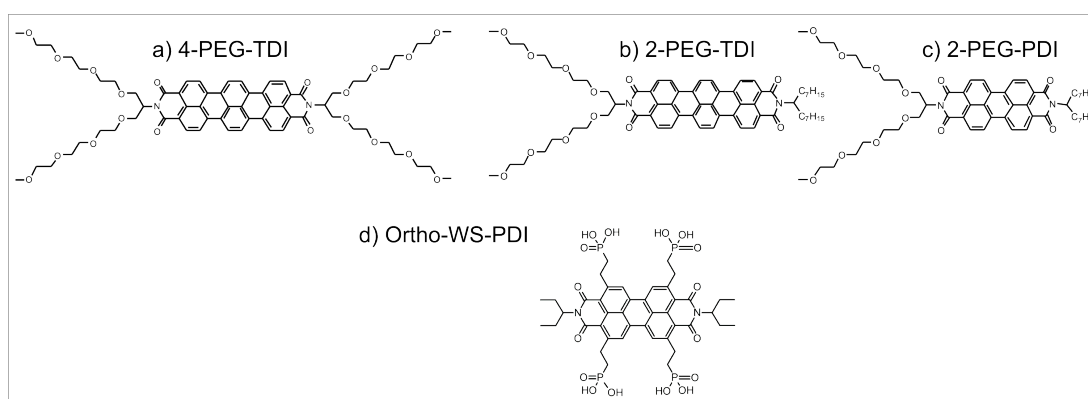

Figure 1: Chemical structure of (a) 4-PEG-TDI, (b) 2-PEG-TDI, (c) 2-PEG-PDI, and (d) Ortho-WS-PDI.

(PEG) chains attached at the *peri*-region of the core structure which is either a perylene derivate (PDI) or a terrylene derivate (TDI) (Figure 1a-c). One perylene and one terrylene dye is modified with two PEG chains, and another terrylene derivate has four PEG chains. The results of single-molecule experiments showed that the terrylene dye with four PEG chains (4-PEG-TDI) formed soluble nonfluorescing H-aggregates in water, so that the absorption bands were blue-shifted with respect to those of the fluorescing monomeric form. The presence of a surfactant such as Pluronic P123 led to the disruption of the aggregates due to the formation of monomers in micelles and a strong increase in fluorescence was observed. Application for labeling cell membranes can be considered for this dye since it adsorbs in a similar way as monomer to a lipid bilayer. This causes fluorescence of the adsorbed dye molecules and thus illumination of the membrane. Furthermore, a single-molecule study of all three rylene dyes in polymeric films of polymethyl methacrylat (PMMA)

showed excellent photostability with respect to photobleaching, far above the photostability of other common water-soluble dyes, such as Oxazine-1, Atto647N, Cy5, Alexa647 and Rhodamin6G. Especially 4-PEG-TDI seems to be a promising dye for membrane labeling due to its high photostability and its strong fluorescence when attached to the membrane.

Another strategy to achieve water-soluble perylenediimide derivatives was to functionalize the *ortho*-position of the core which was demonstrated for the first time using phosphonate derivatives in a Murai-type alkylation reaction. The results of the single-molecule experiments revealed a much higher absorption coefficient and higher quantum yield of fluorescence compared to most commonly used water-soluble PDI derivatives for bioapplications.

In summary, most rylene derivatives have high chemical, thermal, and photochemical stabilities. Owing to these properties, they should also be excellent biological probes. However, most of them are not soluble in water and form nonfluorescing aggregates in aqueous medium. To tackle this problem new rylene derivatives were synthesized in the group of Prof. K. Müllen via the introduction of hydrophilic moieties at the *peri*-position (for example 4-PEG-TDI) or at the *ortho*-region (for example Ortho-WS-PDI; Figure 1d). In our experiments ultrahigh quantum yields of the *peri*-functionalized dyes could be obtained by means of the introduction of polyacrylates or branched glycol chains that are able to suppress the aggregation of the rylene cores. One of these compounds (4-PEG-TDI) formed strongly fluorescent monomers in lipophilic environments and is therefore an interesting dye molecule for labeling cell membranes. In addition, a new functionalization method of the *ortho*-position of rylene derivatives was successfully used to achieve water-soluble, non-aggregating and photostable perylenediimide derivatives (Ortho-WS-PDI). These molecules were incubated with HeLa cells and showed the pathway of endosomes by an increased dye concentration around the perinuclear region.

Highly Oriented Mesoporous Silica Channels: Synthesis Strategies, Host-Guest Interactions and Application in Electrophoresis

In the core part of this thesis, a novel synthesis method for large-pore, well-aligned 2D hexagonal mesoporous silica thin films was developed in close cooperation with Bastian Rühle from the group of Prof. Thomas Bein (LMU). The alignment was achieved by confinement in poly(dimethylsiloxane) (PDMS) microgrooves without the necessity of additional forces (such as electric fields). The influence of various experimental conditions including the way the grooves were filled, surface modification at the solid/liquid interfaces, and the height-to-width ratio of the microgrooves on mesopore alignment was described. With this technique, highly oriented mesoporous silica channels could be obtained at a length scale of several millimeters. For a nondestructive, detailed, and wide-ranging structural characterization of the as-synthesized mesochannel silica network single-molecule spectroscopy was applied. Highly photostable terrylene derivatives, such as As-TDI (Figure 2a), were incorporated into the channels at concentrations suitable for single-molecule microscopy. A maxi-
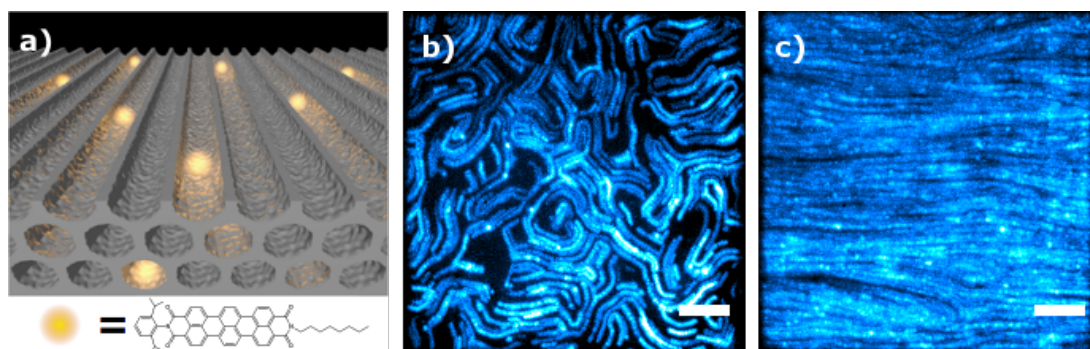

Figure 2: (a) Schematic representation of the highly oriented silica mesopores and the chemical structure of the incorporated As-TDI molecules. (b-c) Maximum projections of the individual frames of movies recorded with a wide-field fluorescence microscope showing the diffusional pathways of single fluorescent As-TDI molecules in (b) purely oriented and (c) well-oriented mesochannels. Scale bars are 5 μm.

mum projection of individual frames recorded with a fluorescence microscope immediately gave a global overview (map) of the pore structure (Figure 2b and c)), thus providing direct feedback for tuning synthesis conditions. In addition, deeper insights into the real nanoscale structure of the mesoporous silica framework were obtained through high-resolution single-molecule tracking experiments. The high spatial accuracy of the experiments allowed for the direct observation of dead ends and jumps of single dye molecules between individual channels in the mesoporous silica host. Nevertheless, due to the low concentration of defects, the diffusion could be described as a 1D random walk where the molecules diffuse along the highly oriented, parallel channels and sometimes switch from channel to channel through small defects. Template removal and calcination of the aligned films resulted in an increased defect concentration; however, the overall order of the structures remained intact.

Furthermore, the controlled movement of single molecules in highly oriented, template-filled meso-

porous silica thin films under the influence of an electric field was demonstrated in electrophoresis experiments. Moreover, a model for the structure of the host and for single-molecule diffusion of charged and uncharged species was proposed. The velocity of the charged molecules increased with increasing electric field strength and could therefore be directly influenced by an external stimulus. By applying an electric field diagonally to the aligned pores, molecules which were located in the mesopores showed a directed movement along the mesoporous silica channels, however, some of them disappeared through defects into the solution outside the sample and followed the diagonal field lines. In the reverse way molecules on their diagonal path in solution entered the sample through defects and moved then along the pore directions in the sample. Furthermore, the application of the mesoporous host material for separation of differently charged molecules in an electrophoresis experiment was demonstrated.

Finally, a strategy to incorporate biomolecules such as labeled DNA molecules into the highly oriented mesopores was developed and the behavior of the DNA molecules was obtained with a wide-field fluorescence microscope. However, due to limits during the measurements, such as high background fluorescence and immobility of the molecules, an improvement of the pore functionalization is necessary.

In Summary, single-molecule microscopy was a helpful tool to optimize the synthesis conditions of the aligned host material and revealed the real structure of the mesochannels with their defects and heterogeneities, which cannot be assessed with bulk methods. The alignment of such mesoporous material is of great importance for applications, such as catalysis, lab-on-a-chip techniques or electrophoresis. The latter was also successfully demonstrated in this thesis and showed the controlled movement and separation of charged fluorophores within the highly ordered silica mesopores. To separate DNA molecules of different length in such aligned channel systems, it is important to find an ideal functionalization strategy in a future work, which preserves the structure of the pores and enhances the affinity between the host and the guest molecules.

Synchronous Emission On Silver Nanowires: Structural and Optical Characterization

Crystalline silver nanowires were synthesized using a seedless, surfactantless wet-chemical fabrication developed by Caswell et al. Investigations of such silver nanowires were performed by using correlated wide-field fluorescence and transmission electron microscopy. While emission of single entities on silver nanostructures is well studied, our wide-field fluorescence images presented *synchronous* emission from different distinct positions along some of the investigated silver nanowires (about 35 %). Figure 3 represents schematically the coupled emission of a silver nanowire, which is excited with visible light (e.g. 633 nm).
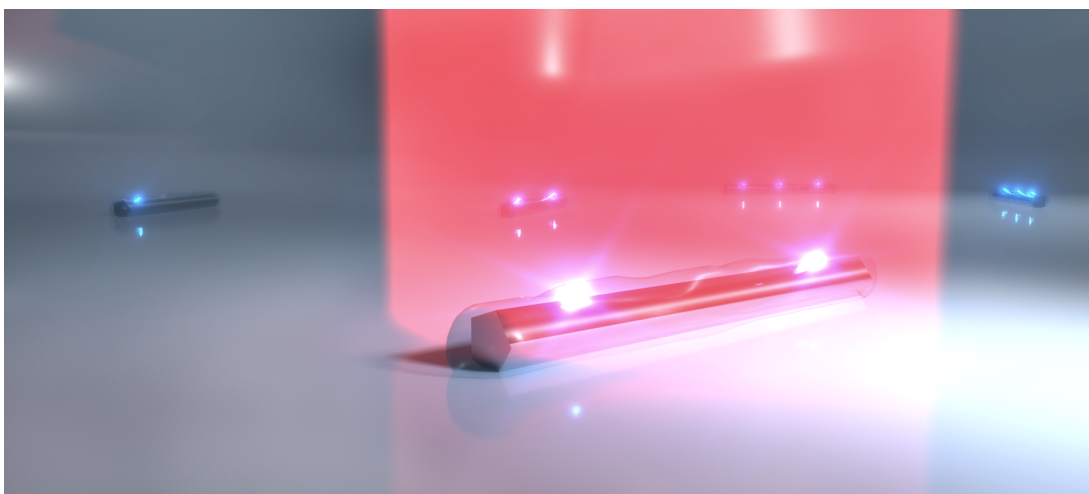

Figure 3: Schematic representation of the synchronous emission of silver nanowires excited with 633 nm.

The sites of emission are separated spatially by up to several micrometers. Nanowires emitting in such cooperative manner were also investigated with transmission electron microscopy in the group of Prof. Christina Scheu (LMU). In particular, analyzing the chemical composition of the emissive areas using energy-dispersive X-ray spectroscopy led to the model that the active emissive centers are small silver clusters generated photochemically and that individual clusters are coupled via surface plasmons on the nanowire.

Contents

1 Introduction

Two decades ago most investigated systems in biology, physics and material science were investigated with ensemble techniques. In these techniques the subject under investigation, for example a specific type of molecule, is investigated in large number quantities and only mean values can be obtained about e.g. an observed property of these molecules. To ensure a correct understanding of the investigated material, it is, however, often important to regard in addition single entities, such as single cells or single molecules. The study of single entities allow to resolve the averaging in the ensemble techniques and to get a distribution of values for the property under investigation instead of just a mean value. Thanks to the rapid development of single-molecule methods with its sensitive detectors, it is possible to detect the fluorescence signal of even a single molecule as emitter. In order to be able to detect single molecules efficiently, it is of great help to synthesize fluorophores having the following advantageous characteristics: high fluorescence quantum yield, high chemical and thermal stability as well as good photostability. To investigate biological systems with such fluorophores as markers, they additionally should be water-soluble. Although, there are a large number of water-soluble chromophores commercially available today, most of them show low fluorescence quantum yields and/or low photochemical stabilities. Rylene derivatives, however, are well-known for their exceptional photophysical and photochemical stability as well as for their high fluorescence quantum yield. Unfortunately, most of them are not soluble in water. Hence, strategies to achieve fluorescent dyes, which are water-soluble and photostable are of fundamental importance. Within the scope of this thesis, the photophysics of new water-soluble rylene fluorophores are characterized regarding their applications in single-molecule studies and membrane labeling.

Furthermore, by incorporating photostable fluorophores into the material of interest, they can act as nanoreporters of the so called host-guest systems and, for example map out the structure of promising materials in nanotechnology. Analysis with single-molecule microscopy reveals unprecedented details of the host structure, e.g. the formation of the pores, the connectivity of the channel system, dead ends as well as insights into the heterogeneity and the mechanistic details of molecular diffusion. For applications, such as catalysis, lab-on-a-chip techniques or electrophoresis the alignment of the channels, is of great importance. The core part of this thesis presents a new approach, where the synthesis of highly oriented silica mesochannels was optimized by giving an immediate feedback of the orientation of the channels with the help of single-molecule microscopy. Furthermore, single-molecule electrophoresis is demonstrated in such highly aligned inorganic mesopores. The results show once more how important single-molecule microscopy can be to understand various details of host-guest systems. In addition, single-molecule microscopy can complete the findings of other well suited characterization techniques, e.g. transmission electron microscopy.

After using single-molecule microscopy to investigate host-guest systems, important insights into

the emission characteristics of silver nanowires is demonstrated by using correlative single-molecule microscopy and transmission electron microscopy. A thorough understanding of the optical, structural and chemical properties of the metal is essential for the development of customized plasmonic systems for nanotechnology applications.

This thesis is structured in four main chapters besides this introduction.

In **Chapter 2** the theoretical background and experimental setup is discussed. The first section presents the phenomenon of fluorescence and describes basic measurements to characterize and quantify fluorescence in particular with regard to single fluorescent molecules. The second section describes the principles and techniques of single-molecule microscopy (SMM) and the experimental setups used in this work. In a third section the analysis of single-molecule data, especially how single molecules are tracked within highly oriented mesoporous silica channels, is explained. The last section in this chapter displays the basics of diffusion theory.

Chapter 3 describes two studies about the functionalization and characterization of rylene derivatives for applications in single-molecule studies and membrane labeling. The aim in these studies is to achieve highly fluorescent, water-soluble dyes. The demands on new water-soluble rylene derivatives as membrane markers are explained and single-molecule studies of the photostability are performed to compare the new dyes to other well-established fluorescent molecules.

In **Chapter 4**, we will take advantage of a bright long living fluorophore to apply single-molecule microscopy for the characterization of highly oriented mesoporous silica channels. The chapter, which is the core of this thesis, consists of four sections. The first section introduces the materials with their different synthesis strategies and formation mechanisms, known from literature, in order to gain macroscopic ordering and mesopore alignment. Moreover, chemical functionalization of the pore walls is of great importance regarding interactions with guest molecules. To characterize host-guest interactions, single-molecule microscopy is a powerful technique as mentioned above. It will be shown that SMM complements other characterization techniques of mesoporous materials, such as X-ray diffraction (XRD), transmission electron microscopy (TEM) and scanning electron microscopy (SEM). In the following section, the knowledge that SMM provides for a thorough understanding of the microscopic structure of the host systems is applied. The section explains how SMM is used to optimize the synthesis conditions, that lead to highly oriented silica mesopores. Furthermore, it presents a detailed description about the influence of various experimental conditions on mesopore alignment. In addition, the section describes the results of high-accuracy single-molecule experiments which allow to assess the real structure of the mesoporous channels with their defects and dead ends and gives dynamical information about the guests. The third section is based on an extended study demonstrating the controlled movement of charged single molecules within highly oriented mesopores under the influence of an electric field. In the last section, a loading strategy of DNA molecules into the highly oriented mesopores is demonstrated for electrophoresis experiments.

Finally, in **Chapter 5** studies of silver nanowires are presented. First, plasmonics in metals are introduced and the experimental setup of a transmission electron microscope (TEM) is explained. Subsequently, a study about optical and structural properties of silver nanostructures is described. It demonstrates the investigation of silver nanowires by using a combination of SMS and TEM. Fluorescence measurements performed with a wide-field microscope show a coupled emission attributed to plasmonic coupling through the wire. The chemical composition of the emissive areas along the wires are presented using energy-dispersive X-ray (EDX) spectroscopy.

2 Single-Molecule Spectroscopy (SMS)

Parts of this chapter summarize general information from actual publications, reviews and text books to put our experimental data into a broader context. They do not intend to describe our own data.

The concept that a single molecule can act as a direct reporter of its environment was pioneered in 1989 by Moerner and Orrit, who were the first reporting on the optical detection of single fluorophores in a solid matrix at liquid-helium temperatures [1, 2]. Since then, Single-molecule microscopy (SMM) was continuously improved (e.g. adapting it to room temperature) and now plays a role in various fields such as chemistry, biology, physics and material science [3–7]. It can reveal a variety of different information, which are otherwise hidden in the ensemble averaging, e.g. conformational changes [8, 9] and individual reaction rates of single molecules [10, 11]. Furthermore, the behavior of fluorescent dye molecules in porous materials (host-guest interactions) allows to draw conclusions about the properties of the host [12] as well as insights into the heterogeneity and the mechanistic details of molecular diffusion. Even the pathway of virus entry into the cell [13] and the movement of single motor proteins on actin filaments [14] have been demonstrated by single-molecule microscopy. Recently, the ergodic theorem could be confirmed experimentally with single-molecule experiments [15]. This powerful fluorescence based method is also used throughout this work.

In the following, the theoretical background which is fundamentally important for this thesis is introduced. First, the phenomenon of fluorescence is presented. Afterwards, the basic principles of SMM are discussed and the main techniques used for studies in this thesis are explained in detail. In addition, the analysis of single-molecule experiments, e.g. single particle tracking, how to generate and analyze a trajectory and the basic knowledge of the diffusion theory are displayed.

2.1 Fluorescence

Fluorescence is the spontaneous emission of light by an individual molecule after absorption of a photon. This process continues as long as photons are absorbed and is explained briefly with the Jablonski diagram (Figure 2.1) conceived by Alexander Jablonski in the 1930s.

  Usually a molecule is in the electronic ground singlet state (S_0). By stimulation of the molecule with light, it can be excited to an higher vibrational level, oftentimes of the first electronic excited singlet state (S_1). From there, the molecule undergoes vibrational relaxation to the lowest vibrational
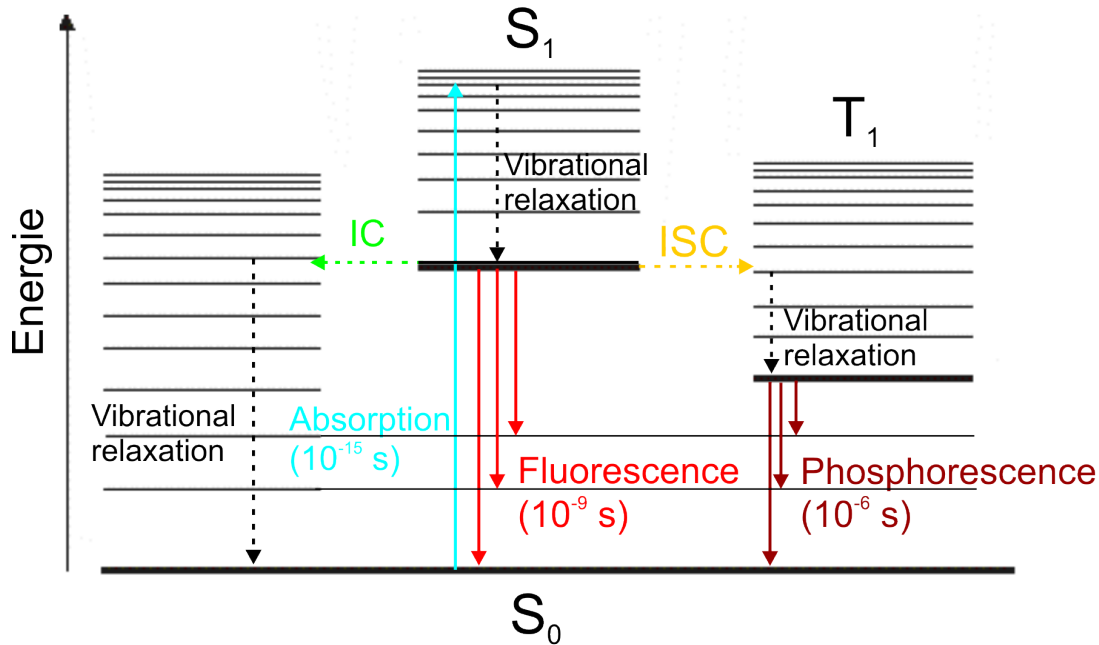
Figure 2.1: Jablonski diagram. Schematic representation of the electronic and vibrational energy levels. S_0 is the electronic ground singlet state and represents the energy of a molecule that is not being excited by light. S_1 is the first excited singlet state, whereas T_1 is the lowest triplet state. Dashed black arrows display vibrational relaxation for each electronic state. After exciting a molecule from the electronic singlet ground state S_0 to the first excited singlet state S_1, vibrational relaxation to the lowest vibrational level of (S_1) occurs. From there the molecule has three ways to return to the electronic ground singlet state: By emission of fluorescent light, by radiationless internal conversion (IC) or by intersystem crossing (ISC). Figure adapted from [16].

level of (S_1). Subsequently, the molecule has three ways to return to the electronic ground singlet state: (1) By emission of fluorescent light, (2) by radiationless internal conversion (IC) or (3) by intersystem crossing (ISC). Fluorescent light on a timescale of 10^{-9} s and radiationless internal conversion (IC) are followed by vibrational relaxation (which occurs on a timescale of 10^{-12} s) to reach the lowest energy level (S_0). With a much lower probability the excited molecule can transit to the triplet state (T_1) by intersystem crossing (ISC). To reach the ground state from there, the electron needs to reverse its spin, otherwise the transition is unlikely and forbidden by quantum theory [16]. This process is called phosphorescence and occurs on a timescale of 10^{-6} s or longer. In addition to the listed ways, how an excited molecule can return to the electronic ground state, the vibrational energy of a fluorophore can also be transferred to nearby molecules via direct radiationless interactions (this process is called "quenching"). Of all possibilities, fluorescent light is the most wanted process regarding fluorescence microscopy. The emitted light has always less energy, i.e. a higher wavelength than the absorbed light. This property is particularly important for microscopy, to separate the emission of the sample from the excitation. A typical absorption and emission spectrum of an organic fluorescent dye molecule (here for a terrylene diimide (TDI) derivative in chloroform) is depicted in Figure 2.2.
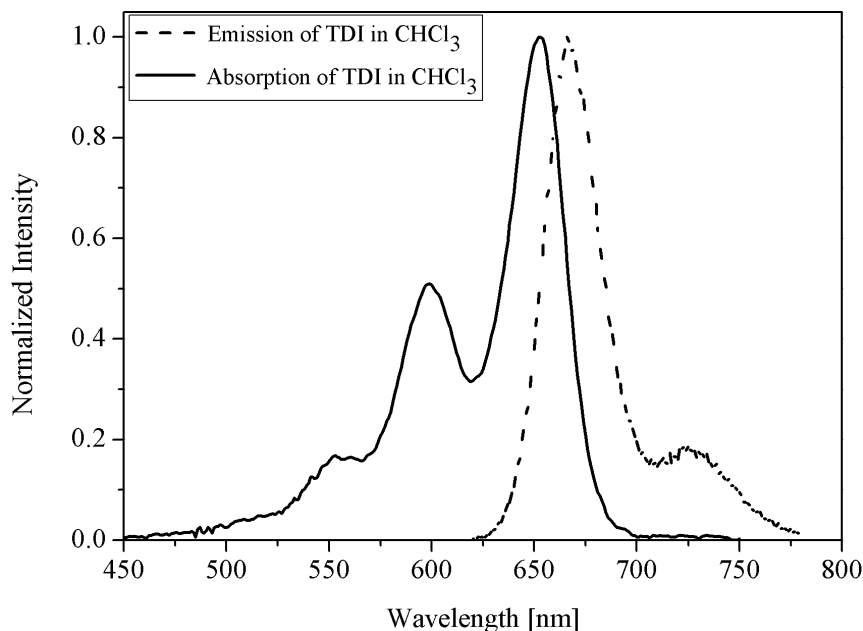
Figure 2.2: Absorption and emission spectrum of a terrylene diimide derivative in chloroform. The dye was excited at 633 nm and has its absorption maximum at 650 nm. The maximum of the emission peak is at 670 nm.

The respective absorption and emission spectra result from the relative positions of the energy states in the Jablonski diagram shown above. For most fluorophores, the emission is the mirror image of the $S_0 \rightarrow S_1$ absorption. Furthermore, the absorption and emission bands are broadened compared to an idealized system, where the absorption and emission lines are as narrow as possible. The broadening is caused by: (1) the molecules immediate surroundings (e.g. solvent molecules, thermal fluctuations in a solid matrix) and (2) the ensemble averaging effect of slightly different, statistically distributed fluorescence spectra. The latter can be suppressed by higher dilution of the dye molecules. However, at room temperature the spectrum of a single molecule is still broadened due to homogenous broadening and resembles the ensemble spectrum. This can be eliminated by performing experiments at low temperatures. From the spectra, various characteristica of fluorophores can be obtained such as the molar extinction coefficient ϵ_λ. It is a measure of the probability that a fluorophore will absorb a photon. Using the Beer-Lambert Law:

$$\epsilon_\lambda = \frac{A}{c \cdot l} \tag{2.1.1}$$

where A is the absorbance (determined from the absorption spectrum), c the concentration of the fluorophore and l the length of the sample, the molar extinction coefficient can be calculated at a specific wavelength. Another parameter to characterize fluorescence is the quantum yield Φ_f. This parameter describes the probability that the relaxation from S_1 will occur under emission of a photon. It is defined as the ratio between the fluorescent rate k_f and the sum of all relaxation rates

including the radiationless relaxations $k_{radless}$ explained above:

$$\Phi_f = \frac{k_f}{k_f + k_{radless}} \qquad (2.1.2)$$

It follows that the ideal dye molecules for SMS should have a quantum yield near 1. Moreover, the lifetime of the excited state before the molecule may undergo an irreversible reaction to form a non-fluorescing species (this process is called photobleaching) can be investigated. In addition, the number of total emitted photons (TEP) and the total time of fluorescence emission (called survival time (ST)) before photobleaching are important parameters and characterize the fluorescence capability and the photostability of a fluorescent dye. In Chapter 3 we will present studies encompassing the characterization of photophysical properties of single molecules.

2.2 Principles and Techniques

Nowadays, there are different types of microscopes available for single-molecule experiments, such as confocal, total internal reflection fluorescence (TIRF) or wide-field epi-fluorescence microscopes. All these techniques are based on the detection of fluorescence light, which can provide an excellent signal-to-noise (or signal-to-background) ratio.

In the following the principles of single-molecule microscopy are explained and a detailed description of both setups, the wide-field epi-fluorescence and the confocal microscope which have been mainly used in this work, is given.

2.2.1 Wide-Field Fluorescence Microscopy

Fluorophores are excited with a laser beam at $632.8 \, \text{nm}$ (He-Ne gas Laser; Coherent) or at $532 \, \text{nm}$ (diode pumped solid-state Laser; Cobolt Samba TM Laser). The laser intensities can be regulated by optical density (OD) filter wheels (OD 0-2, Thorlabs) and the laser bandwidth is narrowed down by respective laser line filters (Laser Components GmbH). Lens L1 ($f = 50 \, \text{nm}$; Thorlabs) is an achromatic lens and couples the light into an optical multimode fibre (0.6 mm in diameter; Optronics GmbH), which is shaken by a motor to eliminate interference patterns. A second achromatic lens L2 ($f = 50 \, \text{mm}$; Thorlabs) paralyzes the light. To prevent photobleaching in sample areas outside the region of interest (ROI) a quadratic aperture was home-build, which reduces the size of the circular laser beam. The image is then focused on the back focal plane of the microscope objective by the achromatic wide-field lens L3 ($f = 200 \, \text{mm}$; Thorlabs) inside the epi-fluorescence microscope (Eclipse TE200; Nikon). The sample is illuminated in wide-field mode by a parallel beam exiting the objective in a quadratic area of about $30 \, \mu\text{m}$ times $30 \, \mu\text{m}$ corresponding to the image of the quadratic aperture on the sample. It can be also illuminated by a built-in white light lamp of the microscope adjusted for Köhler illumination in transmission mode. The light is then guided by using the switchable mirror to a digital camera for focus alignment or by using a white light source to an ocular. Since the concentration of the fluorescent dye molecules is kept very low ($\leq 10^{-10} \, \text{M}$) single

molecules can be detected by their individual fluorescence spots imaged on the EM-CCD camera. The imaging is done with an oil-immersion objective with a high numerical aperture (*NA* 1.4; CFI Plan Apochromat 100x; Nikon), to collect high amounts of the light emitted by a single molecule. The numerical aperture is defined as:

$$NA = n \sin \alpha \qquad (2.2.1)$$

with n being the refractive index of the medium (here e.g. oil) in which the objective lens is working, and α the half collection angle of the objective. It follows that the higher the *NA*, the higher is the light collection efficiency of the objective and thus, the number of the collected photons. The emitted fluorescence is gathered by the objective lens L4 and then passes a dichroic mirror (dual line beamsplitter 532/633; AHF Analysentechnik) to separate it from the exciting laser wavelength. The emission light exits the microscope through a tube lens L5 ($f = 160\,\text{mm}$) and passes lens L6 ($f = 150\,\text{mm}$) before a dichroic mirror splits the fluorescence light into two separate parallel beams. To ensure equal lengths of both pathways, mirrors were placed in both beam paths. Band-pass filters in both beams (typically 675/250 and 560/40 for the green channel and 730/140 for the red channel, AHF Analysentechnik) are used to block remaining incident laser light. Lens L7 guides both beams to the latter lens L8 ($f = 200\,\text{mm}$), which forms in combination with lens L6 a telescope. This leads to a magnification of the image by a factor or 1.33, i.e. by using a 100x objective the image has a total magnification of 133. The fluorescence signals are focused onto the CCD chip with a small lateral shift between each other and detected by a back-illuminated, cooled electron multiplying charge-coupled device (EMCCD) camera in frame transfer mode (iXon DV897, 512×512 pixels; Andor). One pixel on the camera corresponds to a sample size of $154\,\text{nm}$, according to measurements using a USAF test-pattern (Melles Griot).

Microscope

White light lamp

Sample

Objective L4
100x
NA = 1.4

Excitation pathway

Quadratic aperture

Back focal plane

Lens L2 (f = 50 mm)

Dichroic mirror

Wide-field lens L3
(f = 200 mm)

Fibre shaken by a motor

Switchable
mirror

Ocular or
Digital camera

Optical multimode fibre
(0.6 mm in diameter)

Tube lens L5 (f = 160 mm)

Detection pathway

Lens L1 (f = 50 mm)

Lens L6 (f = 160 mm)

Mirror

Dichroic mirror

Laser line filter

Mirror

Mirror

Filter wheel (OD 0-2)

560/40
and
675/250

Band-pass filter

730/140

Lens L7
(f = 150 mm)

He-Ne gas laser
632,8 nm
max. 75 mW
or
diode pumped solid-state laser
532 nm
max. 100 mW

Lens L8
(f = 200 mm)
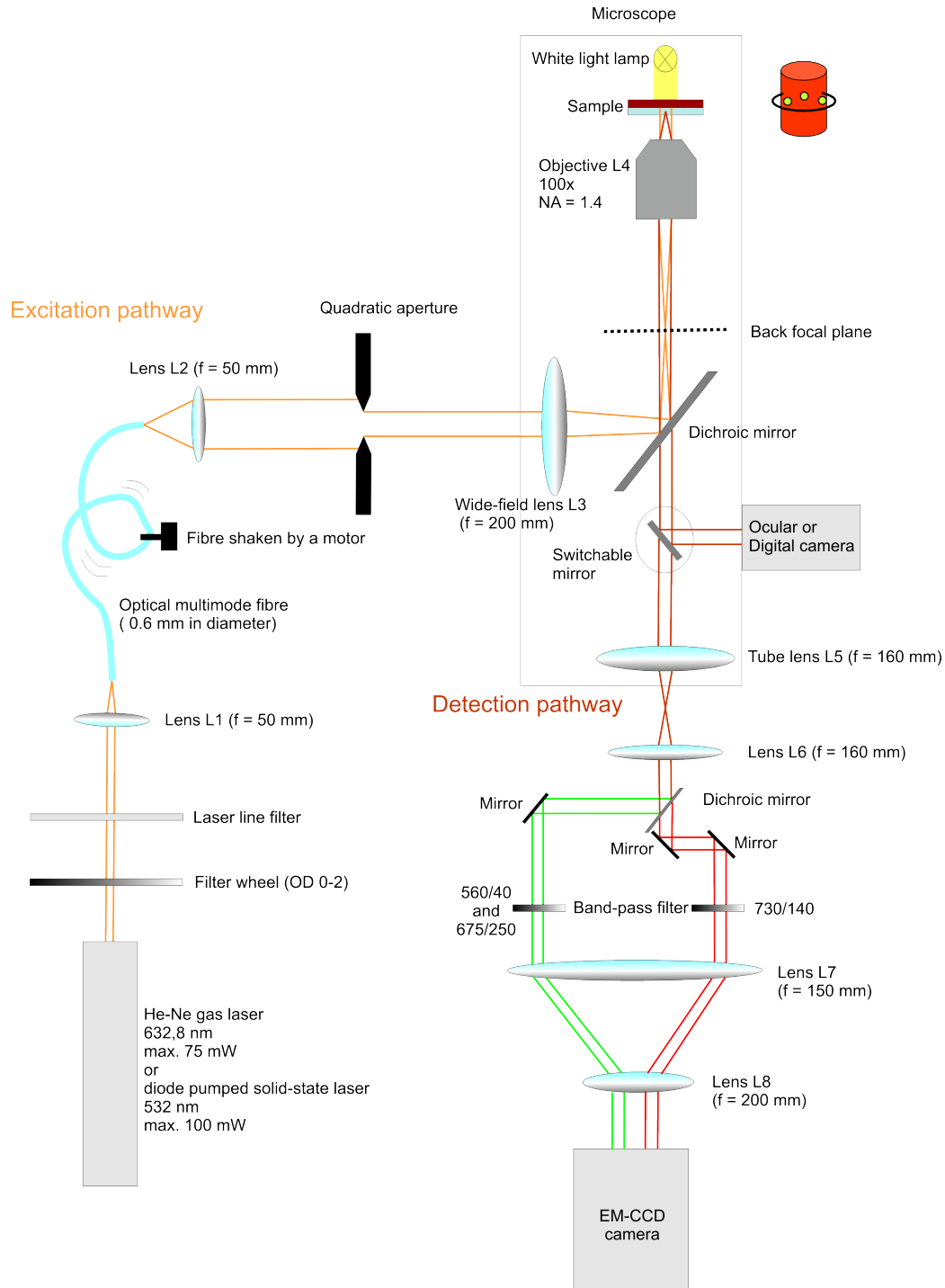
EM-CCD
camera

Figure 2.3: Schematic setup of the wide-field epi-fluorescence microscopy used in this work. The fluorescence light is collected in an epi-fluorescence setup through the same objective and is separated from the excitation light through a dichroic filter and a fluorescence filter. The EM-CCD camera then detects the fluorescence signals. Figure adapted from Reference [17].
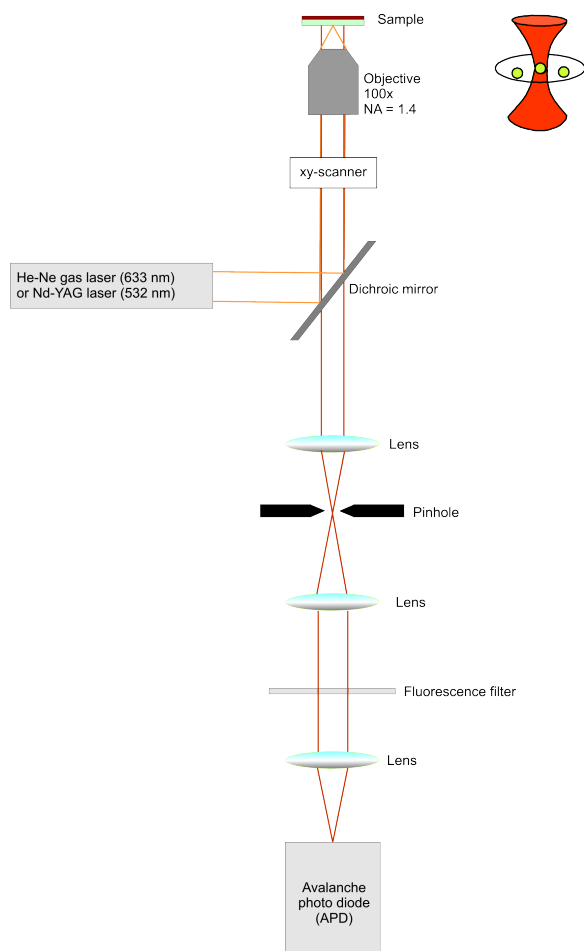
Figure 2.4: Schematic setup of a laser scanning confocal microscope. The fluorescence light is collected and separated from the excitation light through a dichroic filter and a fluorescence filter. The APD detects the number of photons. Figure is adapted from Reference [18].

2.2.2 Laser Scanning Confocal Microscopy (LSCM)

The scheme of a laser scanning confocal microscope (LSCM) (Figure 2.4) is relatively similar to a wide-field microscope. However, there are some important differences. For example with a LSCM the background of a sample can be minimized using a small diffraction limited detection volume created by a confocal aperture (pinhole) in front of the detector. With this a threefold better axial resolution can be achieved. The shape of the confocal volume is ellipsoid and depends on the wavelength, the NA of the objective, and on the refractive index of the medium between the objective and the object. For a 633 nm laser-line, the confocal volume is of roughly 300 nm in the focal plane and 900 nm along the optical axis. Compared to a wide-field microscope, it is possible to record the spectrum of a selected single molecule or the orientation of single molecules. In addition, by stacking 2-D optical sections collects in series, a 3-D reconstruction of the sample can be generated. However, with a LSCM only one point of the sample is observed by scanning the sample at the focal

plane. It is therefore not possible to detect the complete sample at the same time. The observation of one 512×512 pixel image requires a time from 1 to 64 seconds, depending on the integration time.

For the photophysical studies of new dye molecules in Chapter 3 the following setup based on a commercial ZEISS LSM 410 confocal laser scanning microscope was used: The single dye molecules were excited with a He-Ne laser (633 nm) or with an Nd-YAG laser (532 nm). A high-numerical aperture oil-immersion objective (ZEISS 40×1.3 NA oil) was used to illuminate the sample and to collect the fluorescence light. The fluorescence emission of the fluorophores excited with 633 nm were separated from the excitation laser beam using a emission filter (HQ655/150 AHF Analysentechnik). Additionally, red-shifted fluorescence was separated from backscattered laser light by a combination of a dichroic mirror (Q640 LP AHF Analysentechnik), a notch filter (633 nm Notch Kaiser), and an emission filter (HQ730/140 AHF Analysentechnik). The fluorescence signal was detected by an avalanche photodiode (APD, EG&G SPCM-AQ 141). The fluorescence emission of the dyes, excited with 532 nm, was separated from the excitation laser beam using a combination of emission filters (LP 532 and LP 540, AHF Analysentechnik).

2.3 Single-Molecule Tracking (SMT)

Fluorescence emission of single molecules appears as diffraction limited spots (airy disc pattern) on the detector. By tracking these signals, important information about host-guest systems can be received. The position of a single molecule can be determined by fitting a so-called point spread function (PSF). This function can be described by a first order bessel function [19] and be approximated well by a two-dimensional Gaussian distribution (Figure 2.5a) [20–22]:

$$I = A_0 e^{\frac{-(x-x_0)^2}{2\sigma^2}} e^{\frac{-(y-y_0)^2}{2\sigma^2}} \tag{2.3.1}$$

where I is the recorded fluorescence intensity, A_0 is the amplitude of the signal, x_0 and y_0 are the coordinates of the peak position and σ^2 is the radial variance of the 2D Gaussian and linked to the width ω of the Gaussian curve in the following way: $\omega^2 = 2\sigma^2$. Further, the width is linked to the full width at half maximum ω_{FWHM} as follows: $\omega_{FWHM} = \omega\sqrt{ln4}$.

The position accuracy, which is defined as the region in which the true molecule centre can be found with a probability of 68 % [23] corresponding to the standard deviation of the fit of the x_0 and y_0-position, needs to be clearly distinguished from the resolution of the microscope that describes the smallest distance Δd of two objects that can still be distinguished from one another (see Figure 2.5b). The distance Δd is roughly equal to the full width at half maximum of the signal and is given by Abbe's law and the Rayleigh criterion:

$$\Delta d = 0.61 \frac{\lambda}{NA} \tag{2.3.2}$$

It follows that the higher the NA, the smaller the minimum distance Δd of two objects that can be resolved. By using visible light (e.g. 633 nm), the lateral resolution is about 300 nm. SMM,
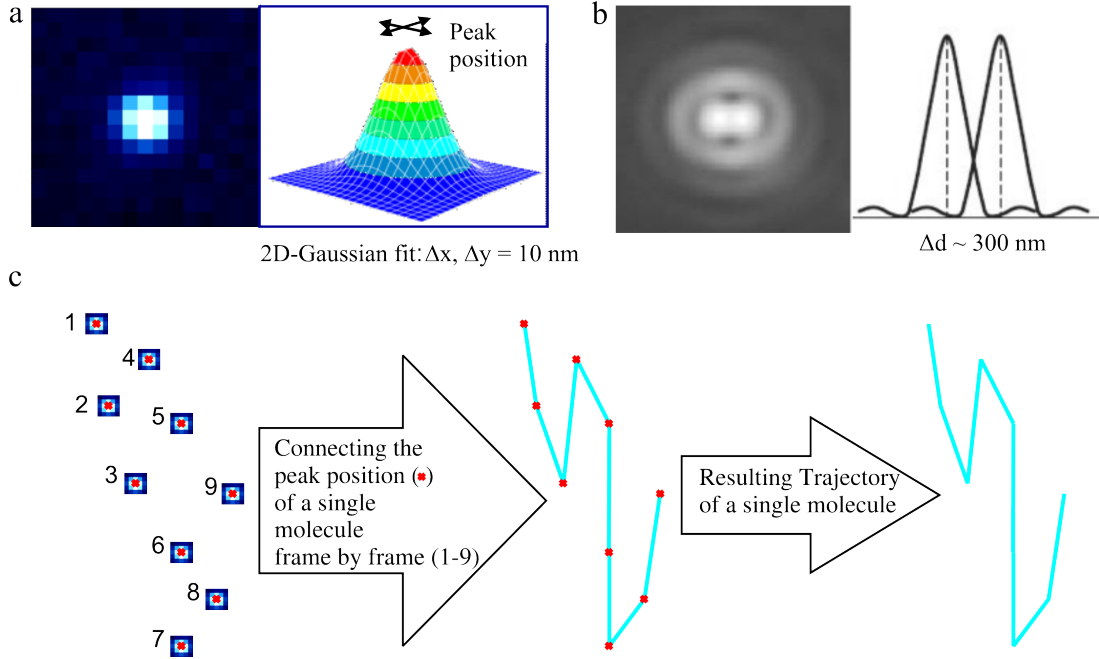
Figure 2.5: (a) The fluorescence intensity distribution of a single molecule can be fitted by a two-dimensional Gaussian curve according to the equation. The peak position x_0 and y_0 can be determined with an accuracy down to typically 10 nm or less. (b) Demonstration of the Rayleigh criterion which describes the smallest distance Δd of two objects that can still be resolved by the optical system. (c) Connecting the peak position of a single molecule frame by frame gives the single-molecule trajectory.

however, overcomes this resolution limit, since the samples in the following studies are prepared on a single-molecule level, meaning a very low fluorescent dye concentration (of about $10^{-10} - 10^{-11}$ M). Hence, the probability of two molecules coming closer to each other than 300 nm is very low.

The position accuracy depends on the photon noise, the error due to the finite pixel size of the detector, and the background. Moreover, it depends on the fluorescence intensity of the single molecule since Δx is inversely proportional to the square roote of the number of collected photons. Thus, in SM experiments one tries to get as many photons as possible from a single fluorescent molecule. This can be achieved by the use of the proper optical system as described in section 2.2.1, as well as by using molecules with high fluorescent quantum yield and high photostability so that they can be excited with high excitation intensities. With this the position of a single fluorescent molecule can be determined with an accuracy of typically 10 nm or less.

After determining the position of a single molecule in each frame, the peak positions are connected frame by frame to create a single-molecule trajectory (Figure 2.5c). From single-molecule trajectories, a useful parameter to characterize the diffusion of molecules, can be calculated. This parameter is called the mean square displacement (MSD) and is discussed in the following section.

2.4 Diffusion Theory

Diffusion is a three-dimensional irregular movement of molecules in matter. The individual path of each molecule is referred to as a "random walk". This phenomenon was observed for the first time by the Scottish botanist Robert Brown in 1827 [24]. Honoring this discovery, today the terms diffusion, random walk and "Brownian" motion are often used synonymously. To simplify, the molecules are assumed to move along only one direction (the x coordinate) and to perform steps of identical length d in either the forward or backward direction. Afterwards, these considerations are transferred to two and three dimensions. (The presentation of the theory is according to Reference [23, 25–28].)

The mean kinetic energy $<E_{kin}>$ of a molecule or particle is dependent on the mass m and the mean velocity $<v_x>$ along the x-axis according to the kinetic gas theory:

$$\langle E_{kin} \rangle = 1/2m \left\langle v_x^2 \right\rangle \tag{2.4.1}$$

According to the equipartition principle a molecule possesses an energy E of $1/2k_B T$ per degree of freedom. Therefore, the mean kinetic energy $<E_{kin}>$ along the x-axis is:

$$\langle E_{kin} \rangle = 1/2k_B T \tag{2.4.2}$$

with the Boltzmann constant k_B. The Combination of both Equations 2.4.1 and 2.4.2 gives the mean velocity of a molecule or particle in vacuum with no collisions with other molecules or particles at a given temperature as follows:

$$\left\langle v_x^2 \right\rangle^{1/2} = (k_B T/m)^{1/2} \tag{2.4.3}$$

In general the velocity of the molecule will be affected by the collisions but its average velocity will remain constant as long as the temperature is fixed. In the following, the idealized behavior of a random walk is explained:

The first assumption is that the steps d of a "random walker" in both directions ($+d$ and $-d$) are equally probable. Furthermore, the direction of a given step should in no way affect the direction of a subsequent one, i.e. the sequences of events are uncorrelated. The entire traveled distance x is disassembled into n steps of the length d with a velocity of $\pm v_x$. The mean time between these steps is τ. However, we cannot say where exactly the molecule will be after n steps, but we can predict the probability according to the randomness of the process. Therefore, a large number of random walks has to be considered, all starting at the same point at $t = 0$ and $x = 0$. To characterize the diffusion of molecules microscopically, the mean square displacement (MSD) $\left\langle r(t = n\tau)^2 \right\rangle$ is a useful parameter. It is defined as the mean value of the squared distances after n steps between the start point of a molecule and its end position, corresponding to time $t = n\tau$. All times of the individual steps are summed to give the total time t. Thus, the MSD increases with the number of steps n. This can be also interpreted as a spread of the ensemble and thus, can be described by the standard

deviation σ of x:

$$\sigma = \sqrt{\langle x^2 \rangle - \langle x \rangle^2} \tag{2.4.4}$$

Moreover, identical molecules, starting from the same point, have an expected value of the displacement which is $\langle x \rangle = 0$. Therefore only $\langle x \rangle^2$, the mean square displacement (MSD), remains to be determined. After n steps a molecule has the position [25]:

$$x(n) = x(n-1) \pm d \tag{2.4.5}$$

The square of this distance is:

$$x(n)^2 = x(n-1)^2 \pm 2x(n-1)d + d^2 \tag{2.4.6}$$

Thus gives the MSD after n steps:

$$\langle x(n)^2 \rangle = \langle x(n-1)^2 \rangle + \langle \pm 2x(n-1)d \rangle + \langle d^2 \rangle = \langle x(n-1)^2 \rangle \pm d^2 \tag{2.4.7}$$

with the assumption of a equal probability for forward and backward steps, the term $\langle \pm 2x(n-1)d \rangle$ is zero. From $x(0) = 0$ for all molecules, it follows that:

$$\langle x(0)^2 \rangle = 0, \langle x(1)^2 \rangle = d^2, \langle x(2)^2 \rangle = 2d^2, ..., \langle x(n)^2 \rangle = nd^2 \tag{2.4.8}$$

This explains why the MSD increases directly proportional to the number of steps n and to the total time t. With $t = n\tau$ it follows:

$$\langle x(t)^2 \rangle = \frac{t}{\tau}d^2 = \frac{d^2}{\tau}t \tag{2.4.9}$$

Replacing the time of each single step τ and the step length d with the diffusion coefficient D analogue to the macroscopic Fick's Law [25],

$$D = \frac{d^2}{2\tau} \tag{2.4.10}$$

the MSD for normal Brownian diffusion in one dimension is given as follows:

$$\langle x(t)^2 \rangle = MSD(t) = 2Dt \tag{2.4.11}$$

This equation can be transferred to two dimensions by regarding the diffusion of a molecule in the x and y-direction ($r^2 = x^2 + y^2$) or to three dimensions by regarding the x, y, z-direction ($r^2 = x^2 + y^2 + z^2$). The MSD for normal Brownian diffusion in $k =$1, 2 or 3 dimensions is then defined as:

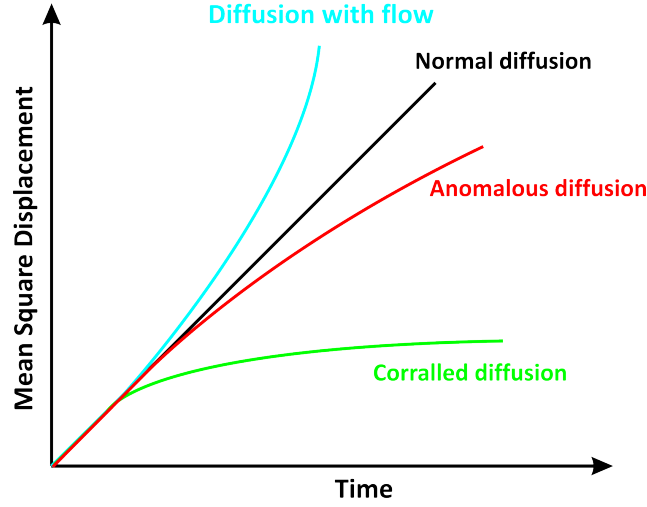$$\langle r(t)^2 \rangle = MSD(t) = 2kDt \tag{2.4.12}$$

Figure 2.6: Mean square displacement (MSD) as a function of time t for normal diffusion (black), anomalous diffusion (red), diffusion with flow (cyan) and corralled diffusion (green) [27].

However, these equations describe the diffusion of molecules with an ideal behavior (Brownian diffusion). In reality, there are often deviates due to interactions, barriers, bonds or active transport by currents or other forces. Figure 2.6 shows the MSD curves of the different types of diffusion and the respective equations are given in the following [27]:

Anomalous diffusion:

$$\langle r(t)^2 \rangle = 2kDt^{\alpha} \tag{2.4.13}$$

Diffusion with flow:

$$\langle r(t)^2 \rangle = 2kDt + (vt)^2 \tag{2.4.14}$$

Corralled diffusion:

$$\langle r(t)^2 \rangle = \langle r_c^2 \rangle \left[1 - A_1 exp\left(\frac{-4A_2 Dt}{\langle r_c^2 \rangle}\right)\right] \tag{2.4.15}$$

with $0 < \alpha < 1$ [28] in Equation 2.4.13 and the velocity v in Equation 2.4.14, the corral size $\langle r_c^2 \rangle$ in Equation 2.4.15 and A_1, A_2 which are constants determined by the corral geometry [26].

Two types of diffusion presented here occur in this thesis. "Normal diffusion" within highly oriented mesoporous channels and "Diffusion with flow" by applying an electric field to the mesoporous channels (see Chapter 4). In order to investigate the diffusion behavior of single molecules with a wide-field microscope, movies of many images in time series (i.e. frames) are collected. Subsequently, the position of the molecules r in the focal plane, i.e. $r = [x, y]$, assuming z indicates the out of

plane position, are determined in each individual frame and connected frame-by-frame to give a SM trajectory according to [23]:

$$\langle r(\tau)^2 \rangle = \frac{1}{N} \sum_{i=1}^{N} (r(t+\tau) - r(t))^2 \tag{2.4.16}$$

where t is the specific time origin and N the number of time origins over which the MSD is averaged for each specific timelag τ.

The SM trajectory gives multitude of information ranging from the pathway of the molecule (e.g. within silica mesopores and thus, the structure of the host) to the diffusion coefficient. A straight-forward method to obtain information regarding the mobility of a single molecule is, as explained above, to calculate the mean squared displacement (MSD) *versus* time, according to the Einstein-Smoluchowski equation 2.4.12. In the case of highly oriented silica mesopores (see chapter 4), where fluorophores can only travel along the aligned pores, a one-dimensional movement with $k = 1$ will be described. Molecules moving in the plane of a thin mesoporous film will be treated as 2-dimensional systems with $k = 2$. As the wide-field microscope produces only a 2-dimensional projection of a 3-dimensional system, the number of dimension will be $k = 2$ here as well. The diffusion constant D will be obtained from the linear part of the MSD versus time plot by fitting the data-points with a line.

After having introduced the basics of single-molecule microscopy and diffusion theory, in the following chapters publications of my thesis and unpublished work will be presented. In these chapters the basic ideas and concepts presented above are used. Where necessary more background specific to the investigated subject will be given. All chapters stand by themselves and consist of an experimental procedure, results and discussion.

3 New Photostable Rylene Derivatives for Single-Molecule Studies

Parts of this chapter are based on the articles "Photophysics of New Photostable Rylene Derivatives: Applications in Single-Molecule Studies and Membrane Labeling" by Melari Davies, Dr. Christophe Jung, Philipp Wallis, Tobias Schnitzler, Dr. Chen Li, Prof. Dr. Klaus Müllen, and Prof. Dr. Christoph Bräuchle, published in *ChemPhysChem*, 12(8):1588-1595, 2011
and "Ortho-Functionalized Perylenediimides for Highly Fluorescent Water-Soluble Dyes" by Glauco Battagliarin, Melari Davies, Dr. Stephan Mackowiak, Dr. Chen Li, and Prof. Dr. Klaus Müllen, published in *ChemPhysChem*, 13(4): 923-926, 2012.

3.1 Introduction: Highly Fluorescent Water-Soluble Dyes

Dyes have always been used by men for the design of its environment, e.g. the coloration of textiles and consumer goods [29–32]. Until the 19th century dyes were obtained from minerals, animals or plants by expensive procedures. Nowadays, a large variety of synthetic dyes, such as "functional dyes", are commercially available and serve for a wide range of applications, e.g. liquid-crystal displays, laser, solar-energy converters or bioimaging. For the latter application, fluorescence microscopy has been one of the most popular and powerful tools in the last years [13, 14, 33–44]. Among the fluorescence techniques single-molecule spectroscopy (SMS) can directly reveal dynamics and mechanistic behavior of biomolecules, which is a significant advantage in comparison with conventional ensemble averaging methods [14, 35–40]. Hence, SMS has become a common method to study the dynamical behavior of labeled proteins, virions, drugs, and other bioparticles [13, 41–44]. Since most of the bioprocesses are studied in water or buffer solutions, the interest in new water-soluble fluorescent dyes for labeling biosystems increased over the last few years continuously [33, 34, 45].
There are commercially available fluorescent dyes such as Oxazine-1, Atto647N, Cy5, Alexa647 and Rhodamin6G that are water-soluble, have a large absorption coefficient, a high fluorescence quantum yield and a good chemical stability, but their photostability is limited. However, for SMS measurements it is important to have dyes with a high photostability in order to collect a large amount of information during the experiment. In addition, such dyes should absorb and fluoresce above 600 nm to reduce the background from the autofluorescence of living cells [33, 34, 45]. Rylene derivatives are well-known for their exceptional photophysical and photochemical stability as well as for their high fluorescence quantum yield [46]. However, most of them are not soluble
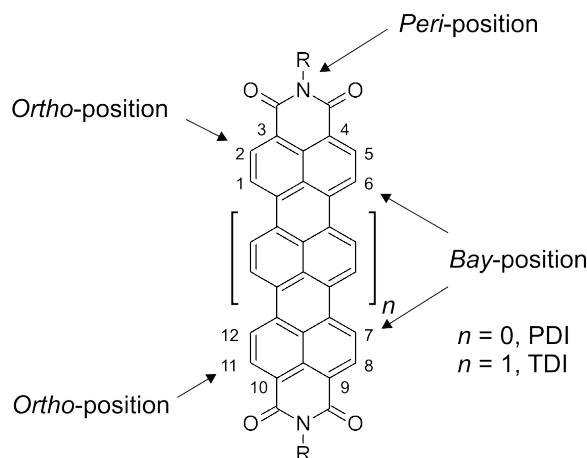
Figure 3.1: Chemical structure of the unsubstituted rylene chromophore illustrating the *peri-* and *bay-*positions. With $n = 0$ the core of a perylenediimide (PDI) derivative is demonstrated. By adding a naphthalene unit (with $n = 1$) the core of a terrylenediimide (TDI) derivative results.

in water [33, 34]. This problem can be tackled by specific functionalization of the rylene scaffold. Charged groups can be introduced at the *peri-* or the 1,6,7,12-positions (*bay-*positions) of the rylene core (Figure 3.1). The substituents have a strong impact on the resulting solubility as well as optical properties, such as HOMO/LUMO energies (HOMO and LUMO are acronyms for highest occupied and lowest unoccupied molecular orbital) and absorption wavelengths. In this way rylene chromophores can be functionalized for the desired applications, e.g. single-molecule investigations or biolabeling [47, 48]. Moreover, the extension of the aromatic system along the long molecular axis from perylene- (PDI, $n = 0$) to terrylenediimide (TDI, $n = 1$) depicted in Figure 3.1 induces a bathochromic shift of about 100 nm per additional naphthalene unit [49]. PDIs absorb at a wavelength in the range around 500 nm, whereas TDIs absorb in the range around 600 nm.

In previous publications charged terrylenediimide derivatives were investigated for applications in biology [33, 34, 50, 51]. All these rylene derivatives were modified with ionic sulfonyl or pyridoxy side groups to provide solubility in aqueous media. However, these derivatives are mostly dissolved as aggregates in aqueous solution. One of these compounds, WS-TDI (structure shown in Figure 3.2d), is a highly photostable dye and forms strongly fluorescent monomers in lipophilic environments. These properties make WS-TDI an interesting dye molecule for the labeling of cell membranes [33]. However, according to our experience, charged dyes are generally not as photostable as comparable uncharged dyes. Therefore, new uncharged rylene derivatives were synthesized in the group of Prof. Müllen and are used to pursue a new strategy.
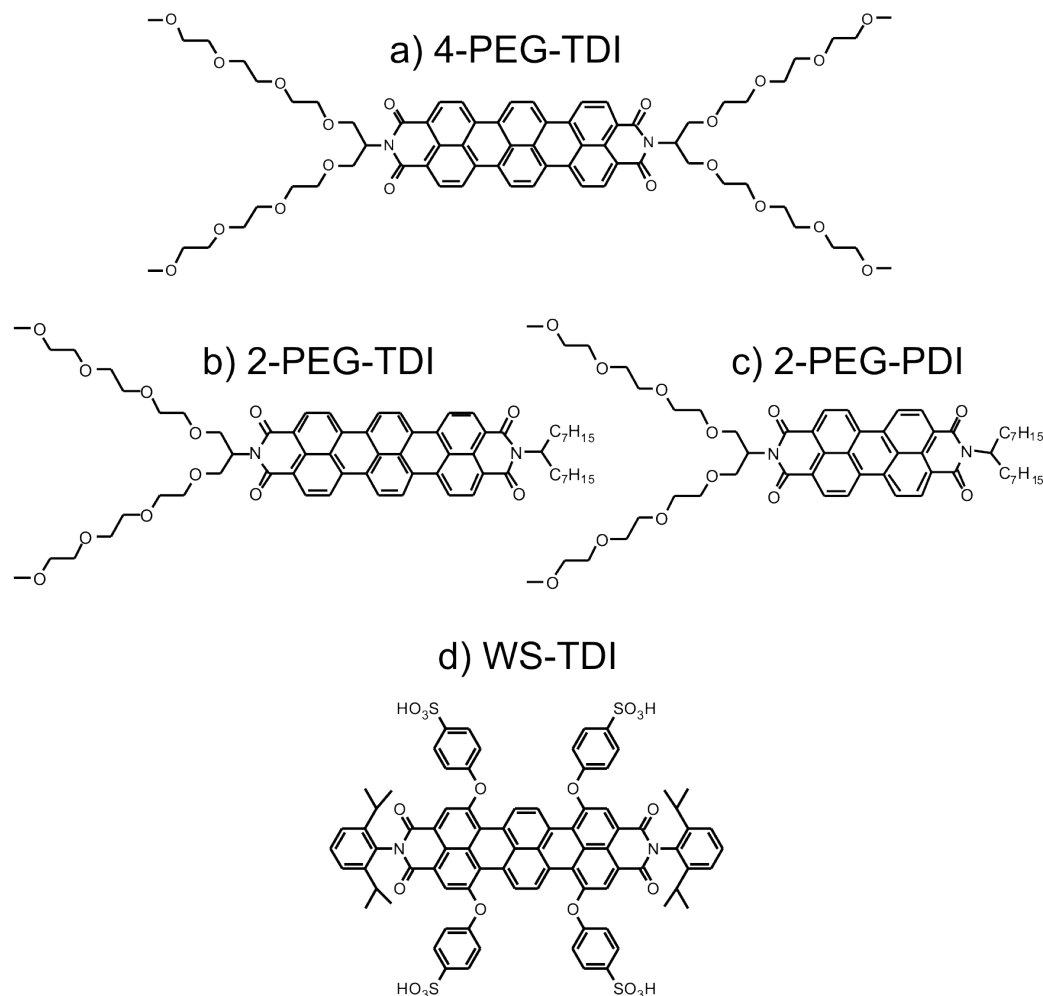
Figure 3.2: Structure of the rylene derivatives: (a) 4-PEG-TDI, (b) 2-PEG-TDI, (c) 2-PEG-PDI and (d) WS-TDI (this dye was investigated in detail in Reference [33]).

3.2 Photophysics of New Photostable Rylene Derivatives

In this section the characterization of the photophysical properties and the aggregation behavior of three new rylene dyes is reported. The chemical structures of the dyes, which differ in the number of polyethylene glycol (PEG) chains and the core, are given in Figures 3.2a-c and are abbreviated with 4-PEG-TDI, 2-PEG-TDI and 2-PEG-PDI, respectively.

The following experiments show the dependence of the absorption and the fluorescence spectra on the extent of aggregation and thus, on the solvent used [33, 34]. Moreover, a single-molecule study of the photostability is conducted to compare the new dyes to other well-established dyes. 4-PEG-TDI is the most promising species out of these three dyes due to its fluorescence properties and the ambivalent nature of this molecule, which offers additional interest as membrane labeling dye compared to WS-TDI.

3.2.1 Absorption and Emission Spectra

Absorption and emission spectra of the new rylene derivatives were measured in the different solvents chloroform, ethanol and water. The absorption and emission spectra of 2-PEG-PDI and 2-PEG-TDI in $CHCl_3$ are shown in Figure 3.3. Their absorption and emission spectra are comparable in their shapes. This is due to the fact that the structure of these dyes are similar and differ only in the core region that determines the spectral region as explained above. The shift from a perylene core, which has a smaller conjugated system than a terrylene core, is typically large [52] (in our case 125 nm).

The absorption bands of 2-PEG-PDI range from $420-550$ nm with a maximum at 528 nm and
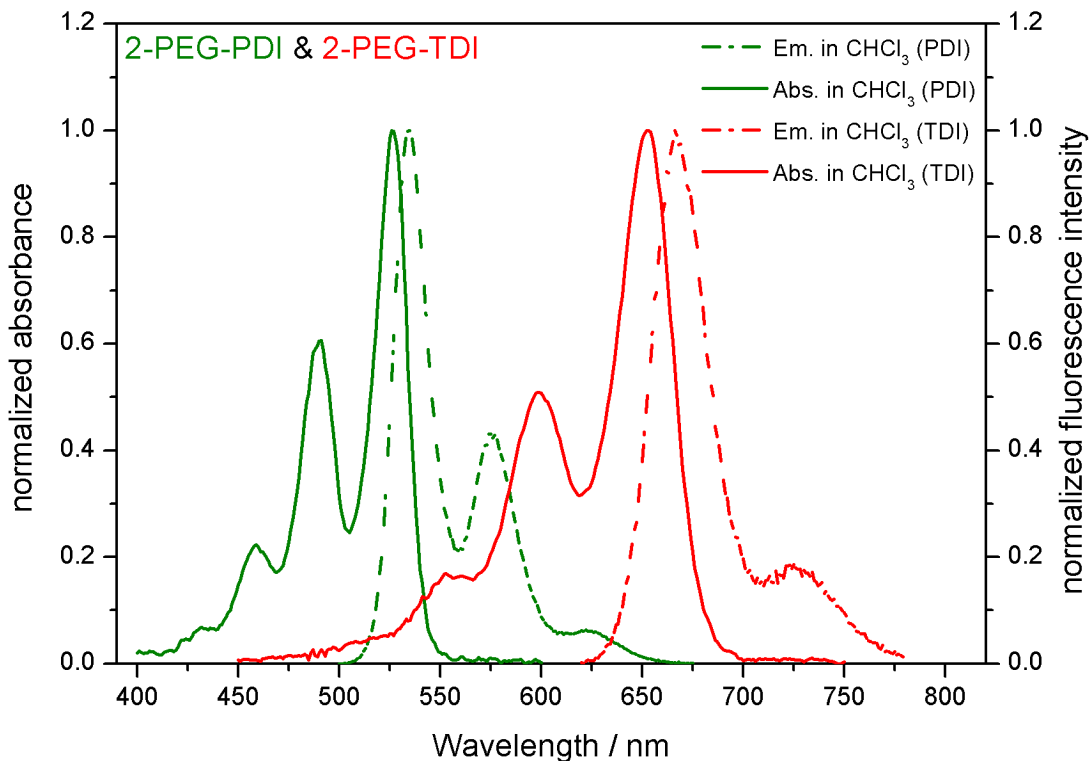
Figure 3.3: Absorption and emission spectra of 2-PEG-PDI (green) and 2-PEG-TDI (red) in $CHCl_3$.

the molar absorption coefficient at this wavelength amounts to approximately $99\,129\,\mathrm{M}^{-1}\,\mathrm{cm}^{-1}$. The absorption spectrum shows three vibrational bands and the fluorescence spectrum is mirror shaped. The Stokes shift of fluorescence emission is 9 nm, while the quantum yield of fluorescence is $\Phi_f = 0.84$ in $CHCl_3$. The 2-PEG-TDI spectra show equally shaped bands but red-shifted. Here the absorption bands are localized in the region from $520-700$ nm with a maximum at 653 nm and the molar absorption coefficient at this wavelength amounts to approximately $130\,327\,\mathrm{M}^{-1}\,\mathrm{cm}^{-1}$. This spectrum again shows three vibrational bands and in a similar way the fluorescence spectrum is mirror shaped. The Stokes shift of fluorescence emission is 22 nm. The quantum yield of fluorescence is $\Phi_f = 0.21$ in $CHCl_3$. Both dyes, 2-PEG-PDI and 2-PEG-TDI, are not soluble in water because of the $\pi\pi$-stacking of the hydrophobic cores. So only 2-PEG chains compared to the big hydrophobic

core are not enough to allow water solubility.

In contrast to the abovementioned dyes, 4-PEG-TDI is modified on both ends of the core, each with two PEG chains. Due to these four PEG chains this dye is soluble in water however, not as solvated monomer dye molecules, but as aggregates, as shown below. The spectra for this dye in different solvents are presented in Figure 3.4a. Compared to 2-PEG-TDI the further PEG chains in the
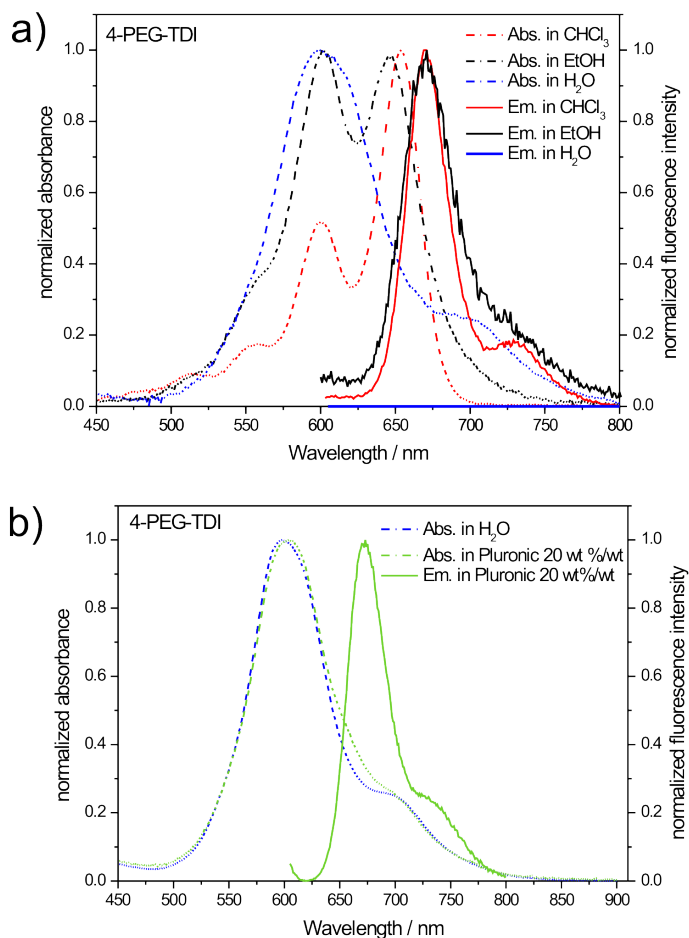
Figure 3.4: Absorption and emission spectra of 4-PEG-TDI (a) in different solvents, (b) in water and in the presence of $20\,\text{wt}\%/\text{wt}$ Pluronic P123.

structure of the 4-PEG-TDI molecule do have only a weak influence on the terrylene chromophore core. This is shown by the absorption bands which are in the same range as those for 2-PEG-TDI. In CHCl$_3$ the absorption maximum for 4-PEG-TDI appears at $653\,\text{nm}$ and the molar absorption coefficient at this wavelength amounts to approximately $129\,620\,\text{M}^{-1}\,\text{cm}^{-1}$. The Stokes shift of fluorescence emission is $17\,\text{nm}$, while the quantum yield of fluorescence is $\Phi_f = 0.19$. Thus, these data are very similar to those of 2-PEG-TDI. However, in EtOH the absorption spectrum consists of

two main bands at the wavelengths of 601 nm and 647 nm. The Stokes shift of fluorescence emission is 23 nm and the quantum yield in EtOH is $\Phi_f = 0.03$. The absorption spectrum measured in EtOH displays in a sense a "transition" between the spectrum measured in CHCl$_3$ and in H$_2$O. With water as solvent the absorption spectrum reduces to a band at 601 nm with a small shoulder at 700 nm. Furthermore, nearly no fluorescence signal is observed in the region of the former fluorescence spectrum. Depending on the environment 4-PEG-TDI forms aggregates in polar media, such as water. It is known that strong intermolecular forces are responsible for self-association of dyes in solution [53, 54]. 4-PEG-TDI is a relatively rigid molecule with a large planar π–electron system with hydrophobic nature and therefore, has a strong tendency to aggregate in polar solvents. Previous studies have already characterized aggregates of $\pi\pi$–stacked perylenediimide dyes [52] and terrylenediimide dyes like WS-TDI in aqueous solution [34], which has a similar π–electron system as 4-PEG-TDI. In contrast to monomeric species, aggregates in solution exhibit distinct changes in absorption and fluorescence properties. Two known species of dye aggregates exist: H- and J-aggregates. In H-aggregates, the absorption maximum is blue-shifted with respect to the isolated chromophore and the fluorescence is normally quenched [34]. In contrast, J-aggregates show fluorescence and the absorption and emission maxima are red-shifted [55]. In our analysis, we observe a strong blue-shifted absorption spectrum for 4-PEG-TDI. This indicates that 4-PEG-TDI forms H-aggregates in water. In addition a small part of the 4-PEG-TDI molecules may also form J-aggregates which can be responsible for the red-shifted shoulder in the absorption spectrum at 700 nm. However, these aggregates show low fluorescence intensity. Furthermore, previous studies have shown the effect that the fluorescence intensity increased dramatically with high surfactant concentrations, for example, with the nonionic block copolymer surfactant poly(ethylene oxide)-poly-(propylene oxide)-poly-(ethylene oxide) (Pluronic P123) [34]. Experiments showed that P123 forms micelles with a concentration above 0.04 wt%/wt, which leads to an incorporation of the dye molecules into the micelles so that most of the molecules are present in a monomeric form associated with the hydrophobic micelles [34]. Herein, we could observe a similar increase of fluorescence intensity of 4-PEG-TDI in the presence of 20 wt%/wt Pluronic (Figure 3.4b). The corresponding quantum yield of fluorescence is equal to 0.03. Also in this case micelles are formed which incorporate monomeric 4-PEG-TDI molecules and this leads to fluorescence of the dye. All spectral and photophysical data are summarized in Table 3.1.

Table 3.1: Photophysical parameters for 2-PEG-PDI, 2-PEG-TDI and 4-PEG-TDI in different solvents.

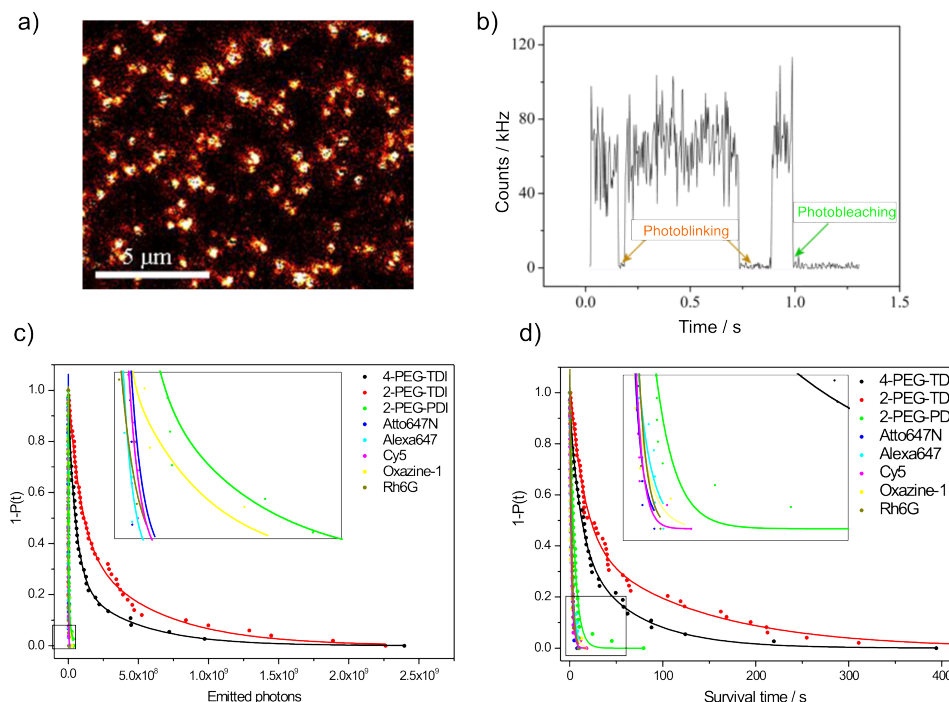| Fluorophore	Solvent	λ_{abs}^{max}[nm]	λ_{em}^{max}[nm]	ϵ^{max}[M$^{-1}cm^{-1}$]	Φ_f
2-PEG-PDI	CHCl$_3$	528	537	99129	0.84
2-PEG-TDI	CHCl$_3$	653	675	130327	0.21
4-PEG-TDI	CHCl$_3$	653	670	129620	0.19
	EtOH	647/601	670		0.03
	Pluronic 20%	603	667		0.03
	Pluronic 10%	603	667		0.01
	H$_2$O	601			

Figure 3.5: (a) Fluorescence image of single 4-PEG-TDI molecules embedded in PMMA. (b) A typical fluorescence intensity trajectory. The molecule shows blinking behavior and undergoes irreversible photobleaching. (c) Accumulated probability distributions of the TEP for, 4-PEG-TDI (black), 2-PEG-TDI (red), 2-PEG-PDI (green), Atto647N (blue), Alexa647 (cyan), Cy5 (magenta), Oxazine-1 (yellow) and Rhodamin6G (olive). The curves cannot be fitted with a single exponential decay. Instead, two-component decays were used and are shown as solid lines. (d) The same evaluation for the ST with biexponential fits shown as solid lines.

3.2.2 Single-Molecule Studies

To investigate the photostability of single molecules, they have to be immobilized. One way is to dissolve highly diluted solutions in a polymer and spin-coat a thin film of the polymer onto a substrate. This leads to a separation of the molecules so that on average only a single-molecule is in the confocal spot of the laser beam. Scanning the laser beam across the sample allows single molecules to be detected by their fluorescence (for details, see Section 3.2.5).

Figure 3.5a shows a typical example of a confocal fluorescence image of individual 4-PEG-TDI molecules embedded in a PMMA film. A typical fluorescence intensity trajectory is depicted in Figure 3.5b. It shows blinking events at 0.2 and 0.7 s and one-step photobleaching after 1 s. From such a fluorescence intensity trajectory, the number of total emitted photons (TEP, area under the function as integral over time in Figure 3.5b corrected by detection efficiency of the setup; see Section 3.2.5) and the survival time (ST, time to the irreversible photobleaching) can be extracted. These two parameters characterize the fluorescence capability and the photostability of a fluorescent dye.

In our single-molecule studies we observed the fluorescence intensity trajectories of at least 40 single molecules for each dye. The resulting distributions of TEP and ST for eight different dyes embedded in PMMA are plotted in Figures 3.5c,d. Molski [56] developed a formalism to calculate the TEP and ST and showed that those distributions are well approximated by either mono- or multiexponential distributions. A biexponential function was successfully fitted to the data and plotted in the graphs. It can be characterized by an average TEP and ST, as described in Section 3.2.5. It should be mentioned that the photobleaching mechanisms and the multiexponential decays are not fully understood on a molecular level so far [57]. However, mulitexponential decays typically are observed when more than one mechanism is present.

The average TEP for 2-PEG-PDI in PMMA is calculated to be $5.3 \pm 2 \times 10^6$, and the average ST gives $4.3 \pm 2.1\,\text{s}$. The comparison of TEP and ST of the two terrylene derivatives shows that the average TEP of 2-PEG-TDI with $280 \pm 50 \times 10^6$ is approximately 1.8 times higher than the average TEP of 4-PEG-TDI. In addition the ST of 2-PEG-TDI ($80 \pm 23\,\text{s}$) is 2.4 times longer than the ST of 4-PEG-TDI. The corresponding averaged TEP and ST data are summarized in Table 3.2 together with some data from the literature [34] and the measured data of the commercially available dyes Oxazine-1, Atto647N, Cy5, Alexa647, and Rhodamine6G. All data were measured in PMMA in order to have the same conditions for a comparison.

Table 3.2: Averaged TEP and ST parameters of different dyes in spin-coated PMMA.

Fluorophore	TEP ($\times 10^6$) in PMMA	ST [s] in PMMA
2-PEG-TDI	280 ± 50	80 ± 23
4-PEG-TDI	160 ± 60	33 ± 12
WS-TDI	110 ± 14 [34]	61 ± 4 [34]
2-PEG-PDI	5.3 ± 2.0	4.3 ± 2.1
Oxazine-1	2.9 ± 1.4	1.5 ± 0.8
Atto647N	1.5 ± 1.0	1.6 ± 0.1
Cy5	1.3 ± 0.9	1.9 ± 0.1
Alexa647	0.9 ± 0.2	2.2 ± 1.0
Rhodamin6G	0.7 ± 0.3	2.2 ± 0.1

By comparing the data one has to take in account that ST includes breaks due to blinking and that the blinking activity is higher for charged dyes than for uncharged dyes. So, for example, WS-TDI has a longer ST than 4-PEG-TDI whereas TEP shows the inverse relationship for the two dyes. For single-molecule experiments the TEP value is more important and we therefore, concentrate on this value. Under these considerations our results clearly show that terrylene derivatives with PEG chains are more useful than with anionic sulfonyl side groups. Moreover, the less PEG chains the better is the photostability. Combining all these informations, a trend for higher TEP of the terrylene dyes can be given: WS-TDI<4-PEG-TDI<2-PEG-TDI. Furthermore, the data in Table 3.2 clearly show that the terrylene derivatives are much more photostable than the commercially available dyes Oxazine-1, Atto647N, Cy5, Alexa647 and Rhodamin6G; roughly by a factor of 100 regarding their TEP values.

3.2.3 Membrane Labeling

We now turn to the point of membrane labeling with the terrylene derivatives. Only 4-PEG-TDI out of the three new pegilated rylene dyes is water-soluble, however, only as aggregates. This behavior is similar to that of WS-TDI described in [34]. Although the aggregation in water is not desirable for labeling of single biomolecules like proteins, it offers a great possibility to label membranes without creating any background. The fluorescence of 4-PEG-TDI in aqueous solution is strongly quenched, whereas the molecules which have a high tendency to attach and incorporate into membranes show a strong fluorescence. Therefore, the membrane will fluoresce bright whereas the solution is dark. This was already shown for WS-TDI [33]. However, 4-PEG-TDI is even more photostable than WS-TDI regarding the TEP and this has an additional advantage. We investigated the ability for
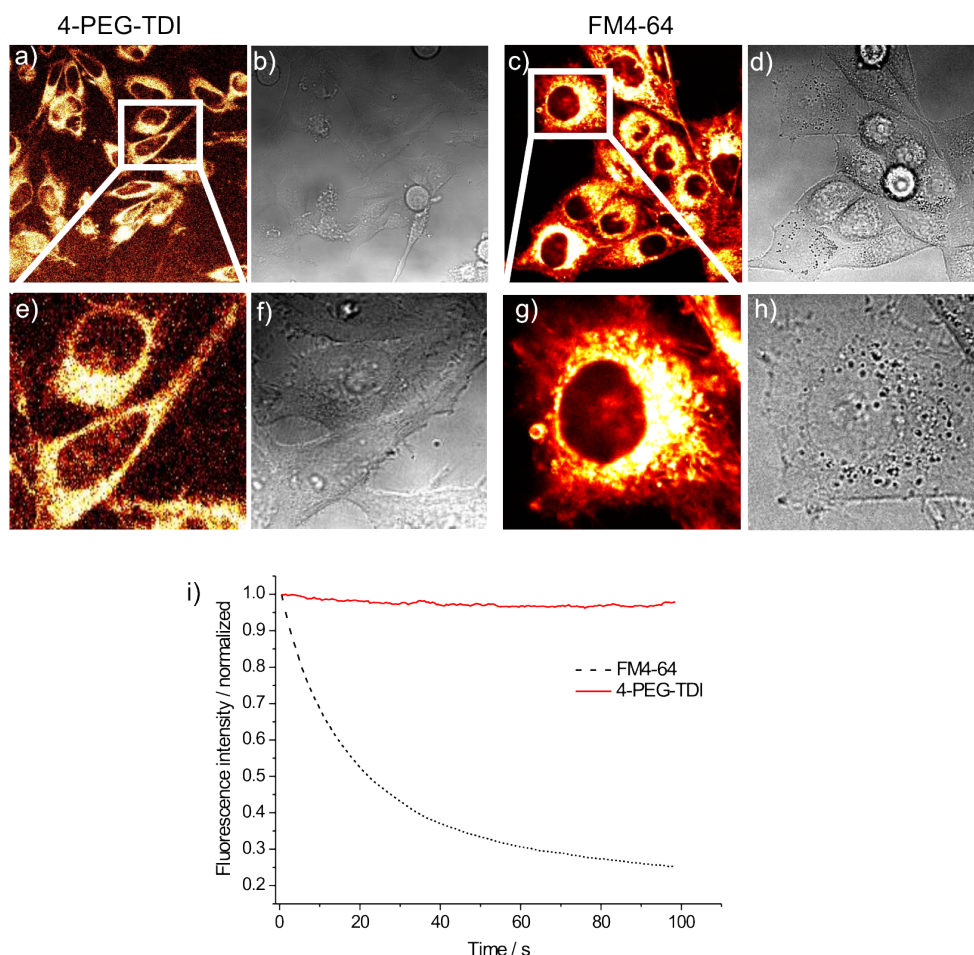

Figure 3.6: (a), (e) Fluorescence images of HeLa cells loaded with 4-PEG-TDI with their corresponding transmission images (b) and (f). (c), (g) Fluorescence images of HeLa cells loaded with FM4-64 and their corresponding transmission images (d) and (h). (i) Plot of the normalized fluorescence intensity as a function of time for 4-PEG-TDI (red line) and FM4-64 (black dots).

labeling HeLa cells with 4-PEG-TDI. This is shown in Figure 3.6. Furthermore, we observed that the cells are alive for many hours similar to the experiments with the other TDI derivatives [33]. By comparing the labeling of HeLa cells with 4-PEG-TDI and FM4-64 (this dye is well-known for its specific labeling of membranes, endosomes and mitochondria [58, 59]) we see that both dyes label the same cell compartments in a similar way (Figures 3.6). However, our movies clearly show that the photostability of 4-PEG-TDI is much higher than that of FM4-64, which results in a much longer observation time (Movies P1 and P2 on the Supplementary CD). The intensity curves for the two dyes also indicate the superior imaging capabilities of the 4-PEG-TDI dye due to its high photostability (see Figure 3.6i).

3.2.4 Conclusion

Three new photostable rylene dyes for applications in single-molecule studies and membrane labeling have been synthesized and their photophysical properties were characterized. These dyes differ in the number of polyethylene glycol (PEG) chains attached to the core structure which is either a perylene derivate or a terrylene derivate. One perylene and one terrylene dye is modified with two PEG chains, and another terrylene derivate has four PEG chains. The results show that the terrylene dye with four PEG chains (4-PEG-TDI) forms soluble nonfluorescing H-aggregates in water, so that the absorption bands are blue-shifted with respect to those of the fluorescing monomeric form. The presence of a surfactant such as Pluronic P123 leads to the disruption of the aggregates due to the formation of monomers in micelles and a strong increase in fluorescence. Application for labeling cell membranes can be considered for this dye since it adsorbs in a similar way as monomer to a lipid bilayer. Furthermore, a single-molecule study of all three rylene dyes in polymeric films of PMMA showed excellent photostability with respect to photobleaching, far above the photostability of other common water-soluble dyes, such as Oxazine-1, Atto647N, Cy5, Alexa647 and Rhodamin6G. Especially 4-PEG-TDI seems to be a promising dye for membrane labeling with its high photostability.

3.2.5 Experimental Part

The synthesis of the new rylene derivatives and the UV-Visible measurements were performed in the group of Prof. K. Müllen (Mainz).

Synthesis of the Dyes: The ambiphilic perylenediimide **1** (2-PEG-PDI) was synthesized by imidization of the monoanhydride **2** [60] with the branched alkoxyamine 3 [61]. Compounds **2** and **3** were dissolved in toluene and stirred at 90°C under argon for 16 h (Figure 3.7). The raw product was purified by preparative thin layer chromatography followed by a final GPC purification step.
The TDI derivatives **4** (2-PEG-TDI) and **5** (4-PEG-TDI) were synthesized by a similar approach (Figure 3.8). The alkyl-substituted TDI **6** [62] was saponified with KOH in 2-methyl-2-butanol yielding a mixture of terrylene mono- **7** and dianhydride **8**. The crude product mixture was used directly after precipitation for condensation with **3**. The resulting TDI compounds **4** and **5** were
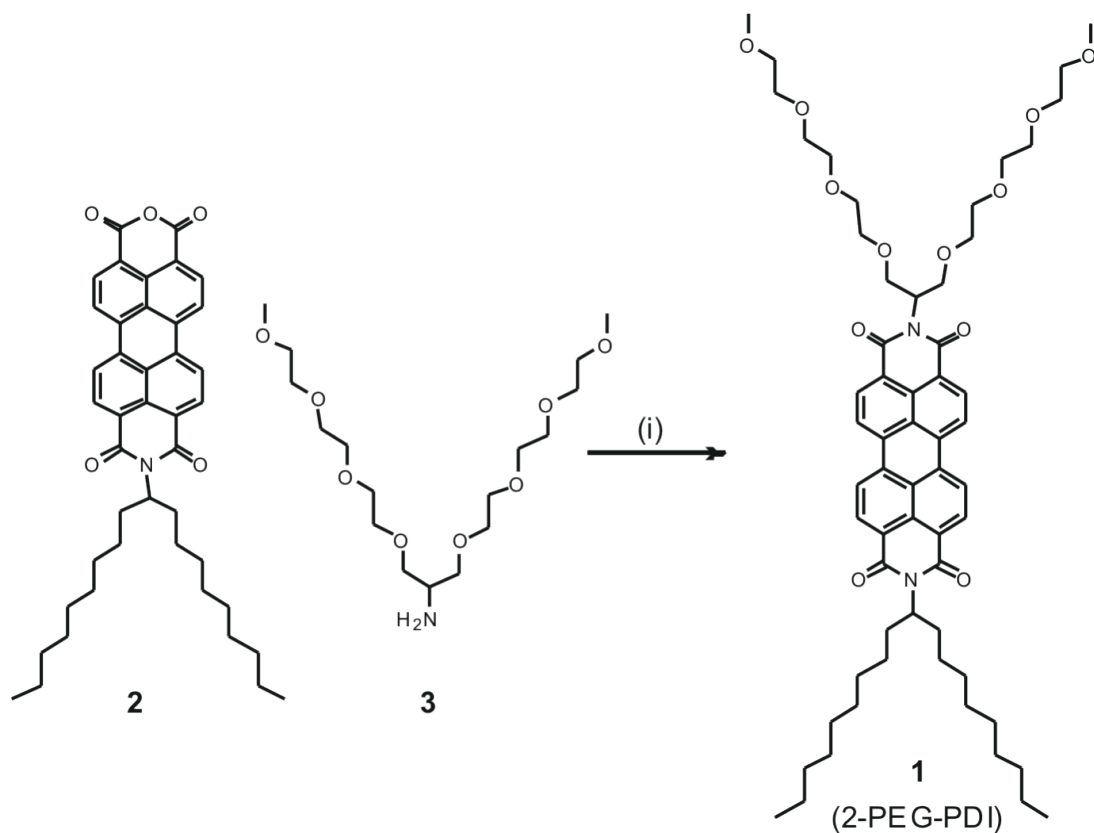
Figure 3.7: (i) toluene, $90°C$, 16 h.

purified by preparative thin layer chromatography and GPC.

$^1H-$ and ^{13}C NMR spectra as well as FD-MS, ESI-MS, IR, UV/Vis and fluorescence analysis of the three new dyes can be found online in the Supporting Information.

UV-Visible Absorption and Fluorescence Spectroscopy: UV/Visible measurements were performed with a Cary 50 Conc spectrophotometer (Varian), and fluorescence spectra measurements were done with a F900 luminescence spectrometer (Edinburgh Analytical Instruments). Quantum yields of fluorescence were measured by comparing the fluorescence intensity of the sample to that of optically dilute solutions of Cy5 in ethanol ($\Phi_f = 0.29$) [33] or Rhodamin6G (R6G) solutions in ethanol ($\Phi_f = 0.95$) [63]. In the quantum yield experiments, changes in the absorption coefficient upon addition of Pluronic P123 were compensated by shifting the excitation wavelength to keep the total absorption of the sample constant. Excitation wavelengths varied between 486 and 600 nm.

Confocal Microscopy: To investigate the photostability on a single-molecule level, the dyes were fixed in a polymer matrix (poly-(methylmethacrylate), PMMA). Thin polymer films (thickness

Figure 3.8: (i) KOH (60 equiv), 2-methyl-2-butanol, $50°C$, 15 min.; (ii) zinc acetate, imidazole, $90°C$, 16 h.

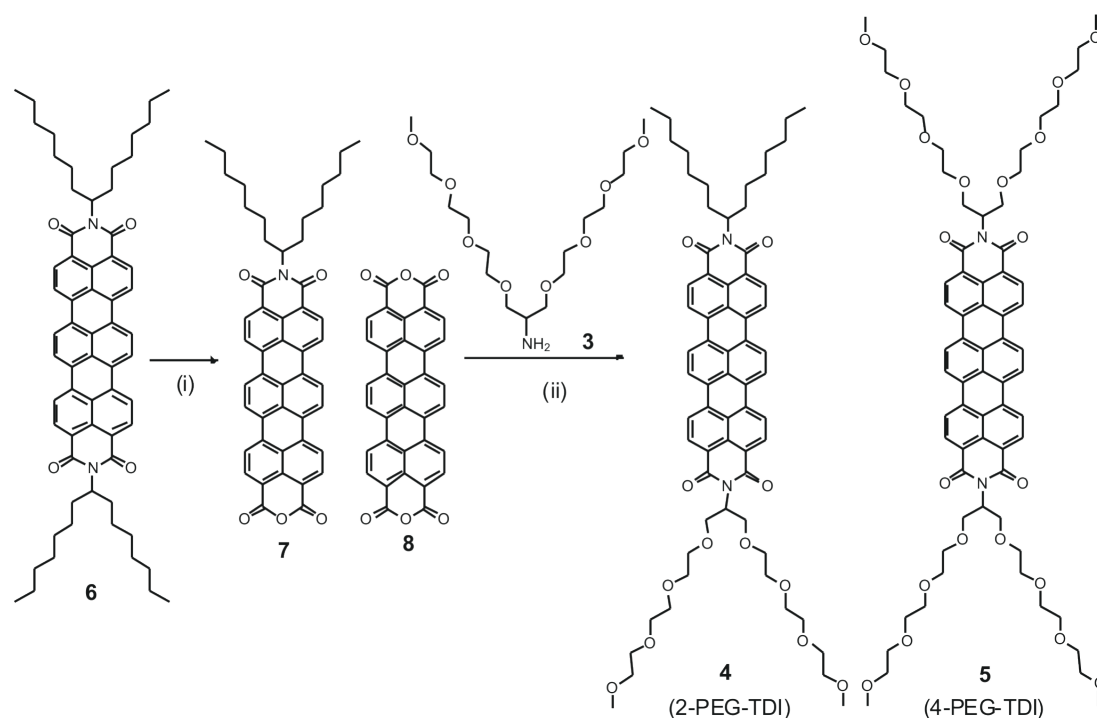$100 – 200\,$nm) were prepared by spin-coating fluorophores in polymer solutions at a concentration of $10^{-10}\,molL^{-1}$ (1 min at 3000 rpm, 2 wt%/wt PMMA in chloroform). In addition to the photostability of the three new dyes, the photostability of Oxazine-1 (Lambdachrome), Atto647N (Atto Tech), Cy5, Alexa647 (Molecular Probes) and Rhodamin6G (Lambdachrome) were also investigated. 2-PEG-PDI and Rhodamin6G were excited with a Nd-YAG laser (532 nm). 4-PEG-TDI, 2-PEG-TDI, Oxazine-1, Atto647N, Cy5 and Alexa647 were excited with a cw He-Ne laser (633 nm) and showed the maximum of fluorescence emissions at approximately 675 nm. A modified scanning confocal microscope (ZEISS LSM 410) was used to visualize fluorescence of the individual dye molecules. High spatial resolution and detection efficiency were achieved with a high-numerical aperture oil-immersion objective (ZEISS 40×1.3 NA oil). Using circular polarized excitation light, all in-plane molecular absorption dipoles are excited with the same probability. The fluorescence emission of 2-PEG-PDI and Rhodamin6G were separated from the excitation laser beam using a emission filter (HQ655/150 AHF Analysentechnik). Red-shifted fluorescence was separated from backscattered laser light by a combination of a dichroic mirror (Q640 LP AHF Analysentechnik), a notch filter (633 nm Notch Kaiser), and an emission filter (HQ730/140 AHF Analysentechnik). The fluorescence signal was detected by an avalanche photodiode (APD, EG&G SPCM-AQ 141). The excitation power at the entrance of the objective was set to $22\,\mu$W. With the confocal setup, the laser beam could be positioned over individual molecules, and their fluorescence intensities were recorded with time. Two photostability parameters could be automatically extracted from the fluorescence time

trajectories of individual molecules by a custom-written LabView program: the number of detected photons before photobleaching as the integral over a time trace and the survival time, which is the total duration of the time trace until photobleaching. The total detection efficiency of our experimental setup is estimated to be 2.5 % and was used to calculate the total number of emitted photons.

Data Analysis: The analysis of the photostability parameters was based on calculating the probability distributions of the number of total emitted photons (TEP) before photobleaching and of the survival times (ST) [56]. Analyzing probability distributions instead of histograms allows a more precise analysis, avoiding the loss of information due to binning of the histogram. Mono- and biexponential decays can also be better distinguished. The distributions in TEP and ST are well approximated by a multiexponential function, S(t), which is defined by characteristic decay parameters:

$$S(t) = \sum_{i=0}^{n} A_i exp \frac{-t}{\tau_i} \tag{3.2.1}$$

where τ_i is the decay time and A_i is the amplitude of the individual components. The number of exponential components was determined by the decrease in the reduced χ^2 of the fit function. A minimum two-fold decrease in the reduced χ^2 of the fit was required to justify an additional exponential decay in the model function [64]. For all results presented herein, a biexponential function was found to give the best fit with the exception of TDI, where a monoexponential was sufficient to fit both the TEP and the ST. For comparison of the photobleaching behavior between the different dyes, an average TEP or ST, represented by $\langle\tau\rangle$, was defined as:

$$\langle\tau\rangle = \sum_{i=0}^{n} A_i \tau_i \tag{3.2.2}$$

Live-Cell Measurements: HeLa cells (HeLa ACC57, DSMZ, Braunschweig, Germany) were grown in Dulbecco's modified Eagle's medium (DMEM) supplemented with 10% fetal calf serum at $37°C$ in 5% CO_2 humidified atmosphere. Cell culture, fetal calf serum, and PBS buffer were purchased from Invitrogen GmbH (Karlsruhe, Germany). Dye-uptake experiments were conducted in HeLa cells at $37°C$. Solutions ($C \approx 10^{-6} mol L^{-1}$) of 4-PEG-TDI, and N-(3-triethylammoniumpropyl)-4-6-[4-(diethylamino)phenyl]-hexatrienylpyridinium dibromide (FM 4–64 styryl dye, Molecular Probes) were added to the cells adherent on the surface of a cover glass. After an incubation time of about 60 min, the solutions were washed three times with PBS buffer to remove the excess of dye. The fluorescence signal from labeled HeLa cells was monitored by epi-fluorescence microscopy with a wide-field imaging setup. The dye was excited with a He-Ne laser (NEC) at 633 nm. The excitation power was set to 2 mW at the entrance of the microscope. The laser beam was expanded and focused onto the back-focal plane of a microscope objective (Nikon Plan Apo 100 × /1.4 oil; the microscope stand was a Nikon eclipse TE200). Fluorescence was collected by the same objective, separated from backscattered laser light with a combination of filters (dicroic mirror 640 nm cutoff

and band-pass BP730/140 AHF), and imaged onto a back-illuminated CCD detector (Andor, iXon DV897). Movies were recorded with a resolution of 154 nm per pixel and an integration time of 500 ms per frame for the measurements with HeLa cells.

3.3 Ortho-Functionalized Perylenediimides for Highly Fluorescent Water-Soluble Dyes

As indicated above, the development of successful strategies to achieve water-solubility and preserve high fluorescence quantum yields is of fundamental importance. Fluorescent probes for biological applications can be successfully synthesized via the introduction of hydrophilic moieties either at the *peri-* (for example 2-PEG-PDI) or in the *bay*-region, that is, 1,6,7,12-positions (such as WS-PDI) of the perylene core (Figure 3.9) [65, 66]. In the first case it was demonstrated that such properties can be obtained by means of the introduction of polyacrylates or branched glycol chains that are able to suppress the aggregation of the PDI cores. Ultrahigh quantum yields could be obtained, but the absence of sites available for bioconjugation limits their use in biological application. Among bay-functionalized PDIs, a special role is occupied by derivatives of WS-PDI (Figure 3.9), a tetra-phenoxy substituted derivative carrying four sulfonic acid moieties, which was synthesized and widely investigated in the group of Prof. Müllen [51, 67–69]. With its superior photostability, good water solubility and the possibility to introduce anchors at the N-imide positions, these bay-functionalized water-soluble PDIs are able to be bioconjugated and outperform most of the commercially available chromophores in the bioimaging fields. Unfortunately, absorptivities and emissions in water are much lower compared to those of PDIs in organic solvents. In 2009 a new method for the functionalization
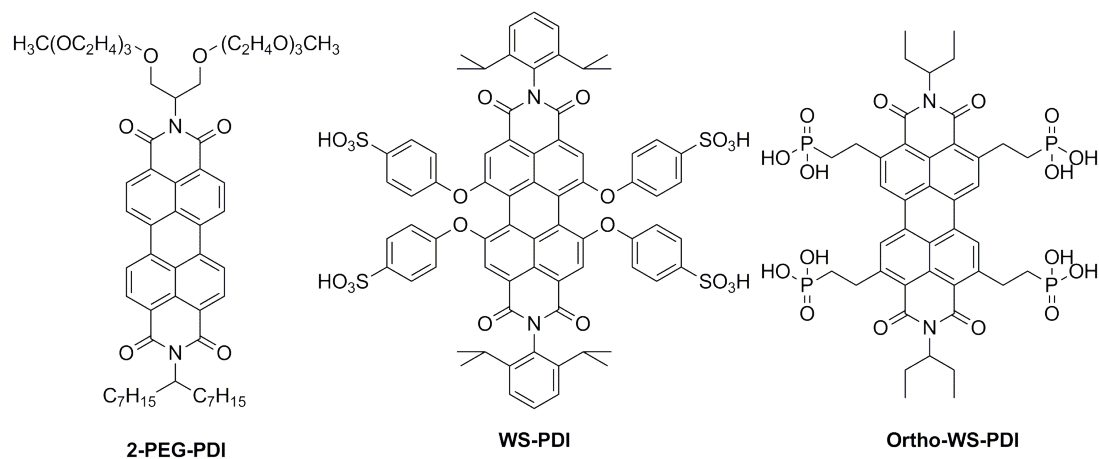
Figure 3.9: Chemical structures of WS-PDI, 2-PEG-PDI and Ortho-WS-PDI.

of the 2,5,8,11-positions (*ortho*-positions) of perylenediimides was discovered [70]. Following the Murai alkylation protocol via a one-step metal catalyzed reaction, the opportunity to selectively alkylate the perylene core was demonstrated, resulting in a tremendous influence on the solubility,
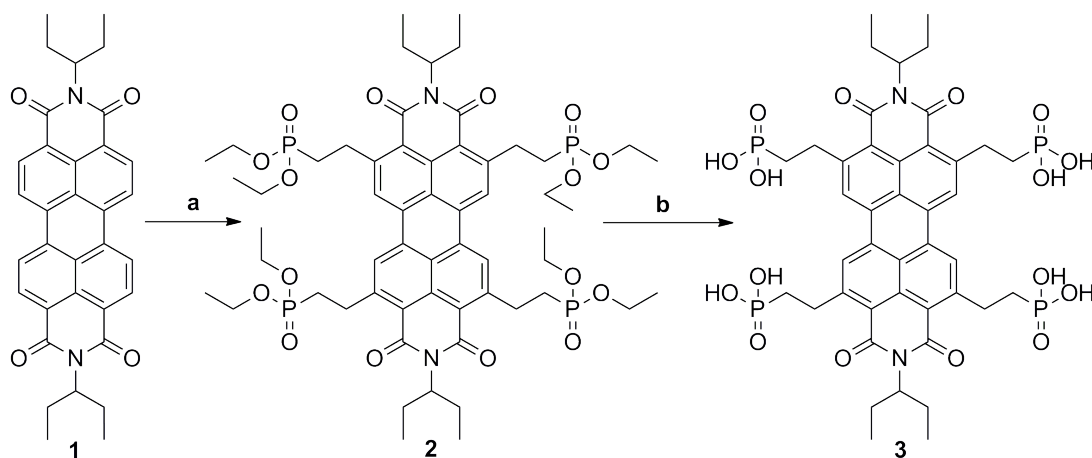
Figure 3.10: Synthetic route for the synthesis of compound **3**: (a) diethyl vinylphosphonate, $(RuH_2(CO)(PPh_3)_3)$, mesitylene, $180°C$ for 12 h; (b1) TMBS, CH_2Cl_2, r.t., 48 h; (b2) MeOH, r.t., 48 h.

intermolecular packing and solid-state fluorescence compared to the parent unsubstituted PDIs [71, 72]. Unluckily the number of alkenes that can be used in these reactions still remains limited due to the ruthenium complex reactivity and no water-soluble molecules could be obtained following this functionalization method [73–77]. In order to develop a competitive method to achieve a new water-soluble PDI derivative, a commercially available olefin should be used, able to react with PDIs in high yields and readily convertible into a water-solubilizing group. This is the case for diethyl vinylphosphonate. The absence of allylic hydrogens avoids undesired parasitic isomerisation reactions, which are usually lowering the yields of the alkylation procedure [78]. Additionally, phosphonates can be hydrolyzed to obtain phosphonic acids [79]. Such functional groups do not only find application in the field of surface functionalization and fuel cells, but are also capable of carrying two negative charges at biologically relevant pH values, with the possibility to synthesize water-soluble labels with enhanced resistance to aggregation and fluorescence quenching [80–83].

3.3.1 Synthetic Route of Ortho-WS-PDI

The synthetic route of a new ortho-functionalized WS-PDI is shown in Figure 3.10 and is performed in the group of Prof. K. Müllen. Diethyl vinylphosphonate and PDI **1** are refluxed in mesitylene in presence of the Murai catalyst $(RuH_2(CO)(PPh_3)_3)$ to give compound **2**. The desired product is obtained in almost quantitative yields, and it is soluble in nearly all organic solvents. Successive treatment of **2** with trimethylsilylbromide affords the desired water-soluble derivative **3**.

3.3.2 Absorption and Emission Spectra

Fluorescence and absorption spectra of compound **3** in water are presented in Figure 3.11 and show a slight bathochromic shift compared to the parent unsubstituted derivative **1** in dichloromethane. The molar absorption coefficient of 54.000 $M^{-1}cm^{-1}$ and quantum yield of fluorescence as high
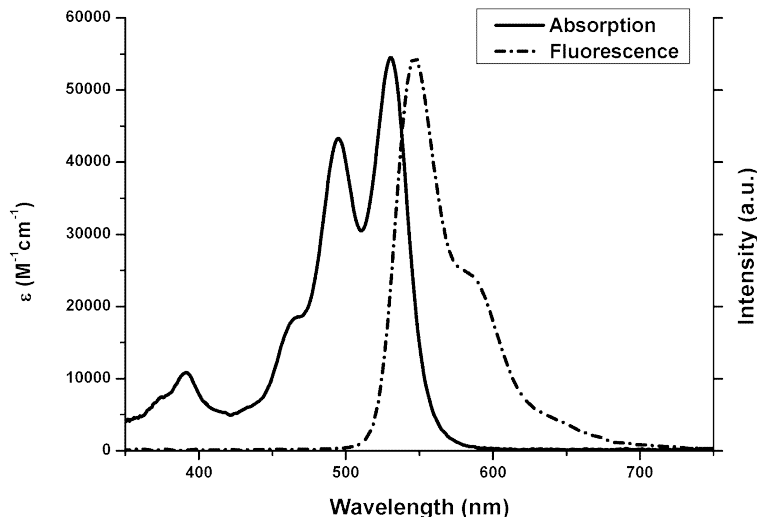
Figure 3.11: Absorption and fluorescence spectra of PDI **3** in water ($\lambda_{ex} = 531nm$).

as 0.77 render this dye an ideal candidate for investigation in single-molecule spectroscopy and biolabeling experiments.

3.3.3 Single-Molecule Studies

To study the photostability of the new ortho-functionalized perylenediimide derivative **3**, we performed single-molecule measurements on a modified scanning confocal microscope in the same way as shown in section 3.2.2 but using a different polymer, named (polyvinyl alcohol, PVA) to immobilize the molecules, so that on average only one molecule was in the confocal spot of the laser beam. We recorded fluorescence intensity trajectories of at least 30 single molecules for each dye and obtained the number of total emitted photons (TEP) from the single-molecule trajectories and the survival time (ST). These two parameters are representative for the fluorescence capability and the photostability of a fluorophore.

Using the formalism developed by Molski [56], we fitted the probability distribution of photons with a mono- or multiexponential distribution. The corresponding averaged TEP and ST for the dyes embedded in PVA together compared to literature data [56] are summarized in Table 3.3. It should be mentioned that the photobleaching mechanisms and the multiexponential decays are not fully understood on a molecular level so far [34]. However, mulitexponential decays typically are observed when more than one mechanism is present. The calculated average TEP for PDI **3** in PVA is $(8.3 \pm 0.5) \times 10^4$, and the average ST gives 2.7 ± 0.8 s. These results were compared with 2-PEG-PDI studied under the same experimental conditions and WS-PDI (data taken from Reference [34]). The comparison of TEP and ST of the three PDI derivatives show that **3** has an approximately 100 times lower TEP but a similar ST compared to 2-PEG-PDI. For single-molecule experiments the

Table 3.3: Averaged TEP and ST parameters of different dyes in spin-coated PVA.

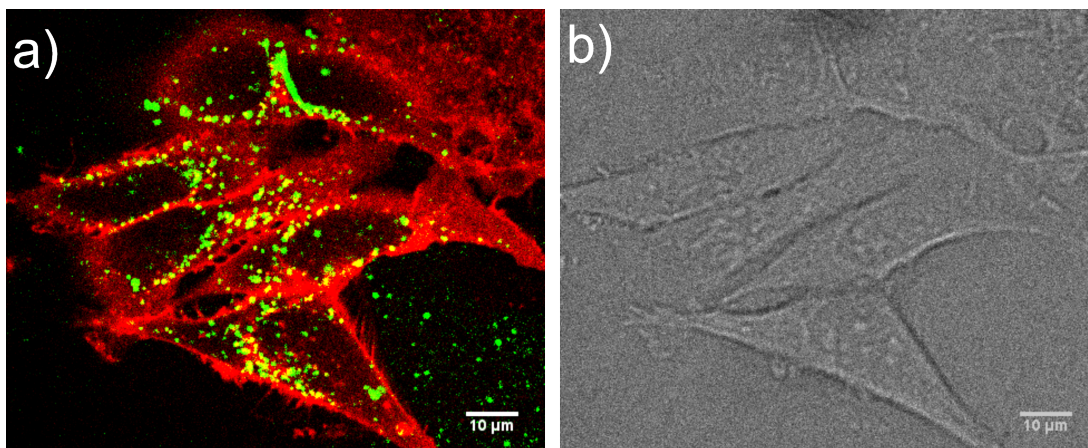| Fluorophore	TEP ($\times 10^6$) in PVA	ST [s] in PVA
WS-PDI [65]	$(7.8 \pm 0.4) \times 10^6$	14.7 ± 0.3
2-PEG-PDI	$(4.3 \pm 0.8) \times 10^6$	3.8 ± 0.2
PDI **3**	$(8.3 \pm 0.5) \times 10^4$	2.7 ± 0.8

Figure 3.12: (a) Confocal fluorescence image of HeLa cells excited with 488 nm and 639 nm laser light. The cell membrane is labeled with Deep Red (red). Uptake of PDI **3** (green) by the HeLa cells is clearly visible as well as an increased dye concentration around the perinuclear region. Also see the movie P3 on the Supplementary CD. (b) Transmission image of the HeLa cells after laser excitation.

TEP value is more important since it is the number of emitted photons that matters, whereas ST includes breaks due to blinking. The blinking activity is higher for charged dyes than for uncharged dyes. This explains the fact that **3** has a similar ST to 2-PEG-TDI, although its TEP value is much lower. Regarding the number of totally emitted photons and the survival time, PDI **3** cannot compete with the other two perylenes 2-PEG-PDI and WS-PDI but is still better than some of the commercially available fluorophores.

3.3.4 Interaction of Ortho-WS-PDI with HeLa Cells

Because of the good water-solubility of compound **3**, we investigated the ability for labeling HeLa cells with **3**. After 4 h of incubation with a dye concentration of 2 µM, PDI **3** was taken up by the cells and is present in the cytosol, presumably in endosomes (Figure 3.12a, green). An increased fluorescence intensity around the perinuclear region (Figure 3.12a, green) can be observed as well as the lack of green fluorescence in the cell membrane. For imaging of the cell membrane, the cells were labeled with Deep Red (Figure 3.12a, red). See also movie P3 on the Supplementary CD. The corresponding transmission image is depicted in Figure 3.12b. The cells seem to be healthy according to their morphology.

3.3.5 Conclusion

A new efficient functionalization method for the achievement of water-soluble perylenediimide derivatives was developed. For the first time the possibility to use phosphonate derivatives in a Murai-type alkylation reaction was demonstrated. The fluorescence capability and the photostability of compound **3** were investigated by TEP and ST experiments. Additionally, their absorption coefficient and quantum yield of fluorescence are much higher than of most commonly used PDI derivatives for bioapplications. Compound **3** was impregnated into HeLa cells for labeling successfully. The investigation towards alternative applications for example, chemosensors of the derivatives of compound **3** are currently ongoing.

In conclusion, highly fluorescent, water-soluble rylene dyes were investigated regarding their photophysical properties. In section 3.2 ultrahigh quantum yields of *peri*-functionalized rylene derivatives could be detected. However, the absence of sites available for bioconjugation limited their use in biological applications. Only 4-PEG-TDI out of the three new rylene dyes, functionalized with four glycol chains, labeled the membrane of HeLa cells. In section 3.3 a new functionalization method of the *ortho*-position of rylene derivatives was successfully used to achieve water-soluble, non-aggregating, and highly fluorescent perylenediimide derivatives. Ortho-WS-PDI showed a higher fluorescence adsorption coefficient and quantum yield than most of commonly used PDI derivatives for bioapplications and interacted with the perinuclear region of HeLa cells.

3.3.6 Experimental Part

The synthesis of Ortho-WS-PDI (PDI **3**), NMR spectra and UV/Vis measurements were performed in the group of Prof. K. Müllen (Mainz).

^1H and ^{13}C NMR spectra were recorded on a Bruker Avance 500 spectrometer and a Bruker Avance 300 spectrometer. Chemical shifts were denoted in δ units (ppm), and were referenced to residual solvent. Mass spectra were recorded with a Finnigan MAT and VG Instruments ZAB 2-SE-FPD. UV/Vis spectra were recorded at room temperature on a Perkin-Elmer Lambda 900 spectrometer with dichloromethane and toluene as solvent. Fluorescence emission spectra were recorded on a J&M Tidas spectrometer. Elemental analyses were performed on an Elementar Vario EL.

Synthesis of the Dyes: N,N'-Bis(1-ethylpropyl)-2,5,8,11-tetrakis[2-(diethoxyphosphoryl)ethyl] perylene-3,4:9,10-tetracarboxylic acid diimide (**2**): PDI **1** (100 mg, 0.19 mmol) and diethyl vinylphosphonate (619 mg, 3.77 mmol) were dissolved in 4 mL anhydrous mesitylene. Argon was bubbled through the solution for 30 min. $(RuH_2(CO)(PPh_3)_3)$ (9 mg, 0.01 mmol) was added to the mixture and the reaction was heated at $180°C$ for 12 h. After cooling the system to room temperature, the solvent was removed. The reaction mixture was dissolved in 10 mL of methanol and poured into 100 mL water. The precipitate was filtered and the desired compound was obtained as a red solid with 95% yield (213 mg, 0.18 mmol). ^1H NMR (500 MHz, CD$_2$Cl$_2$) δ: 8.63 (s, 4 H), 5.08

(m, 2 H), 4.24–4.08 (m, 16 H), 3.73 (dd, J=15.8, 9.3 Hz, 8 H), 2.35–2.15 (m, 12 H), 1.94 (m, 4 H), 1.34 (t, J=6.9 Hz, 24 H), 0.92 (t, J=7.2 Hz, 12 H). ^{13}C NMR (126 MHz, CD$_2$Cl$_2$) δ: 164.73 (s), 149.33 (s), 133.69 (s), 132.26 (s), 128.31 (s), 125.32 (s), 121.10 (s), 62.32 (s), 58.03 (s), 30.86 (s), 27.11 (s), 25.63 (s), 16.89 (s), 11.75 (s). FD/MS (8 kV): $m/z = 1183.6$ (100%) $[M^+]$. UV-Vis (in dichloromethane): λ_{max} (ϵ[M$^{-1}cm^{-1}$]): 524 nm (5.70×10^4), 488 nm (3.81×10^4), 458 nm (1.50×10^4). Fluorescence (in dichloromethane, $\lambda_{ex} = 524nm$): 532 nm. Φ_f: 0.88. Elem. Anal.: theoretical: C: 58.68%; H: 6.96%; N: 2.36%; experimental: C: 58.45%; H: 6.90%; N: 2.24%.

N,N'-Bis (1-ethylpropyl)-2,5,8,11-tetrakis-(dihydroxyphosphoryl) perylene-3,4:9,10-tetracarboxylic acid diimide (**3**): Compound **2** (150 mg, 0.13 mmol) and bromotrimethylsilane (309 mg, 0.266 mL, 2.02 mmol) were mixed together in 25 mL anhydrous dichloromethane and stirred in a sealed vessel for 2 days at room temperature. After evaporating the solvent, the solid was dissolved in 50 mL methanol and stirred at room temperature for 2 days. Afterwards the precipitate in the reaction was filtered and washed with 50 mL methanol and subsequent 50 mL dichloromethane. The desired product was obtained as an orange solid with 84% yield (102 mg, 0.11 mmol). ^1H NMR (250 MHz, DMF) δ: 8.70 (s, broad signal overlapping with protons of phosphoric acid), 4.89 (m, 2 H), 3.67 (s, 8 H), 2.47–1.76 (m, 16 H), 0.89 (t, $J = 7.0Hz$, 12 H). $^{13}CNMR$ (75 MHz, DMF) δ: 164.85 (s), 150.09 (s), 133.49 (s), 132.95 (s), 129.30 (s), 124.82 (s), 120.40 (s), 58.09 (s), 27.93 (s), 25.78 (s), 12.37 (s). UV-Vis (in water): λ_{max} (ϵ[M$^{-1}cm^{-1}$]): 531 nm (5.45×10^4), 495 nm (2.45×10^4), 458 nm (1.57×10^4). Fluorescence (in water, $\lambda_{ex} = 531nm$): 548 nm. Φ_f: 0.76. HRMS-ESI m/z ($[M^+H]^+$): theoretical=963.2208, found=963.2189.

Confocal Microscopy: To investigate the photostability on a single-molecule level, the dyes were fixed in a polymer matrix (polyvinyl alcohol, PVA). Thin polymer films (thickness $100-200\,$nm) were prepared by spin-coating fluorophores in polymer solutions at a concentration of $10^{-10}molL^{-1}$ (1 min at 3000 rpm, 2 wt%/wt PVA in water). In addition to the photostability of the new PDI dye (Ortho-WS-PDI), the photostability of 2-PEG-PDI was also investigated as a reference. All dyes were excited with an Nd-YAG laser (532 nm). The excitation power at the entrance of the objective was set to $20\,\mu$W. For the separation of the fluorescence emission of the dyes from the excitation laser beam we used a combination of emission filters (LP 532 and LP 540, AHF Analysentechnik). The experimental setup and the data analysis was described previously [65].

Live-Cell Measurements: HeLa cells (HeLa ACC57, DSMZ, Braunschweig, Germany) were grown in Dulbecco's modified Eagle's medium (DMEM) supplemented with 10% fetal calf serum at $37^\circ C$ in 5% CO$_2$ humidified atmosphere. Cell culture, fetal calf serum, and PBS buffer were purchased from Invitrogen GmbH (Karlsruhe, Germany). Dye-uptake experiments were conducted in HeLa cells at $37^\circ C$. Solutions of PDI **3** ($c \approx 2\,\mu$M) were added to the cells adherent on the surface of a cover glass. After an incubation time of about 4 h, the cells were washed five times with PBS buffer to remove the excess of dye. The cell membrane was stained with Deep Red (Invitrogen, Karlsruhe). The fluorescence signal from the labeled HeLa cells was monitored by confocal microscopy with a spinning disc microscope (Zeiss). Alternating excitation with $200\,\mu$W of 488 nm light (Coherent) and $25\,\mu$W

of 639 nm light (Coherent) were used to excite PDI **3** and Deep Red, respectively. Fluorescence was collected and separated from backscattered laser light with a dichroic mirror (405/488/568/647 Semrock). Subsequently, the fluorescence signal of PDI **3** and Deep Red were split up by a beam splitter (Semrock), separating fluorescence with a wavelength shorter and longer than 630 nm light. The fluorescence of PDI **3** and Deep Red was bandpass filtered (BP525/50, Semrock and BP690/50, Semrock), before being imaged onto two back-illuminated EMCCD cameras (Photometrics, Evolve). The experimental setup was described previously [12].

4 Highly Oriented Mesoporous Silica Channels for Single-Molecule Studies

This chapter, which is the core of this thesis, focuses on the investigations of the dynamics of single fluorescent dye molecules in highly oriented mesoporous silica channels. In the first section 4.1 important knowledge about mesoporous silica materials, such as the synthesis, formation mechanism and functionalization of sol-gel-derived porous silica materials, is briefly introduced, especially focusing on the evaporation-induced self-assembly (EISA) process for the formation of thin mesoporous silica films. Furthermore, we present a selected fundamental study that opened up new ways of understanding the interactions of hosts and guests by combining information from transmission electron microscopy (TEM) with the diffusion dynamics obtained from single-molecule microscopy studies. The knowledge that SMM can characterize the structural properties of the mesoporous structure in a non-invasive and direct way is applied in section 4.2 to optimize the synthesis conditions that lead to Pluronic F127-templated, large-pore silica thin films with highly oriented mesopores. The alignment is achieved by confinement in poly-(dimethylsiloxane) (PDMS) microgrooves without the necessity of additional forces. Furthermore, the influence of various experimental conditions including the way the grooves are filled, surface modification at the solid/liquid interfaces, and the height-to-width ratio of the microgrooves on mesopore alignment is described. By incorporating fluorescent dye molecules into the mesochannels, possible pathways within these pores including its most relevant defects are explored and mapped out. Additionally, high-accuracy single-molecule tracking experiments allow for the direct observation of jumps of single molecules between individual channels in the silica host. Finally, template removal and calcination of the aligned films is investigated leading to an increase of the number of defects. In an extension of this study, the controlled movement of charged single molecules under the influence of an electric field is described in section 4.3. Thereby, we present a host-guest model which explains the different pathways of charged and uncharged molecules. Furthermore, the influence of the electric field strength on charged molecules is investigated. In section 4.4 a strategy to load biomolecules, such as DNA, into the highly aligned mesopores is given. These studies, once more, demonstrate how important SMM is to reveal the real structure of the mesoporous silica materials and to gain dynamic information about the diffusion of guest molecules inside these networks.

4.1 Introduction: Mesoporous Silica Materials

This section is based on a review article by Bastian Rühle*, Melari Davies*, Prof. Dr. Thomas Bein, and Prof. Dr. Christoph Bräuchle, published in *Z. Naturforsch.*, 68b:1-22, 2013.
*These authors contributed equally to this work.

Porous silica materials are used in a wide variety of applications, including molecular sieves and filters [84, 85], catalysts [86], ion exchangers [87], nanosensors [88] or drug-delivery-systems [89, 90]. They are appreciated for their large pore volume, large surface area, and high chemical and structural flexibility and tunability. These properties allow us to tailor the morphology and interaction chemistry of the porous host systems according to the demands of the desired applications. However, in order to be able to efficiently design and synthesize new materials with the envisioned properties, a thorough understanding of the microscopic nature and structure of the host systems and their interactions with guest molecules is of great importance. There are many techniques that can help to gain an overview of the average, bulk properties of these porous systems, such as NMR [91], electron microscopy [92], X-ray diffraction, and neutron scattering measurements [93]. However, there are often heterogeneities at a nanoscopic or microscopic level that cannot be assessed with bulk methods, but still play an important role for host–guest interactions and can help us to improve our understanding of the porous host systems. While these heterogeneities can be random, there are also cases in which they reflect intrinsic characteristics of the materials, such as phase separation or domain boundaries. In order to be able to extract such information, single-molecule spectroscopy or microscopy measurements are highly desirable.

4.1.1 Synthesis Strategies and Formation Mechanism

Micro- and mesoporous silica materials are usually synthesized by a bottom-up approach, in which small organic molecules or surfactants act as a template for the porous structure of the silica framework. Early and prominent examples of this process include the use of alkylammonium ions to control the pore size and periodicity of zeolites, as demonstrated by researchers at the Mobil Oil Corporation in the 1960s [94]. The templating process results in porous, crystalline solids with a well-defined 1-, 2-, or 3-dimensional network of periodically arranged micropores. Later, this approach was further extended to longer-chain alkylammonium ions [95], which yielded a periodic array of mesopores that were approximately 4 nm in diameter or larger, and gave rise to the development of the MCM (Mobil Crystalline Material) family of mesoporous silica materials. The amphiphilic nature (i.e. the presence of hydrophilic and hydrophobic parts within one molecule) of the surfactant that acts as the structure-directing agent (SDA) allows for a spontaneous assembly of the latter into micelles, resembling a liquid crystalline phase that gives rise to the periodic porous structure. Meanwhile, a variety of other surfactants have been employed to extend the pore-size and structural diversity even further [96, 97], for example non-ionic triblock-copolymers for the synthesis of the Santa Barbara Amorphous (SBA) type materials [98].

The synthesis strategies mentioned above were originally designed for the synthesis of porous par-

ticles that are used in a wide variety of different fields. However, in certain applications such as membranes, low dielectric constant interlayers and sensors, thin films rather than particles are desired. In some of the first approaches that yielded stable, supported mesoporous silica films a substrate was introduced into a silica/surfactant/solvent system in which the initial surfactant concentration was high enough that a micellar phase could be formed (i.e. higher than the critical micelle concentration, cmc) [99–101]. These approaches allowed for the nucleation of hexagonal silica-surfactant mesophases on the substrate with pores oriented parallel to the substrate surface, and further growth and coalescence over a longer period of time resulted in continuous films. However, these films are often macroscopically inhomogeneous and feature granular textures on micrometer length scales. Another approach that yields very homogeneous films even on macroscopic length scales is the evaporation-induced self-assembly (EISA) approach, introduced by Brinker *et al.* in 1999 [102]. This synthesis strategy employs a homogeneous solution of soluble, inorganic building blocks such as alkoxysilanes (typically tetraethylorthosilicate (TEOS)) and surfactant molecules at concentrations lower than the cmc in a volatile solvent mixture, often comprised of ethanol and water. When coating this solution onto a substrate, preferential evaporation of the volatile solvent leads to an increase in concentration of the surfactant and the non-volatile silica precursor in water. This increase in surfactant concentration in turn leads to a spontaneous self-assembly of silica-surfactant micelles, which further organize into liquid-crystalline mesophases. By altering the molar ratios and chemical nature of the solvent mixture, the silica source, and the surfactant, differently arranged porous mesophases such as 2D-hexagonal, 3D-hexagonal, cubic, and lamellar structures can be obtained [103, 104]. In order for the self-assembly process to occur, the silica condensation has to be suppressed or slowed down during the film deposition step by adjusting the pH to a value close to the isoelectric point of colloidal silica (pH $\approx$ 2) [102]. This allows for the cooperative silica-surfactant self-assembly and results in as-deposited films exhibiting liquid-crystalline (i.e. semi-solid) behavior. Only after subsequent aging, thermal treatment, or exposure to acid or base catalysis the silica network solidifies in its final pore geometry.

The liquid-crystalline nature of freshly formed films was confirmed by the fact that tensile stress developed during the mesophase thin film deposition is much lower than that of a similar silica sol prepared without surfactants [102, 105]. Moreover, under certain conditions freshly deposited films could be transformed to a different mesophase (e.g. from lamellar to cubic) [103]. Further proof of a structurally flexible material after deposition and deeper insight into the mechanism of mesophase formation and film organization during the EISA process was gained by different groups through *in situ* grazing incidence small-angle X-ray scattering (GISAXS) experiments [105–107]. Grosso *et al.* [106] investigated the influence of various experimental parameters on the film formation and organization of films prepared by dip-coating from a silica sol with cetyltrimethylammonium bromide (CTAB) as the SDA. They found that – under otherwise identical conditions – the CTAB-to-TEOS ratio plays the main role in determining the structure of the resulting films. By adjusting this ratio to 0.08, 0.10, or 0.12, 2D-hexagonal, 3D-hexagonal, or cubic phases could be obtained. They also found that the degree of condensation of the silica species present in the solution (and hence, the water content and the aging time of the sol prior to deposition) can have a strong effect on mesophase
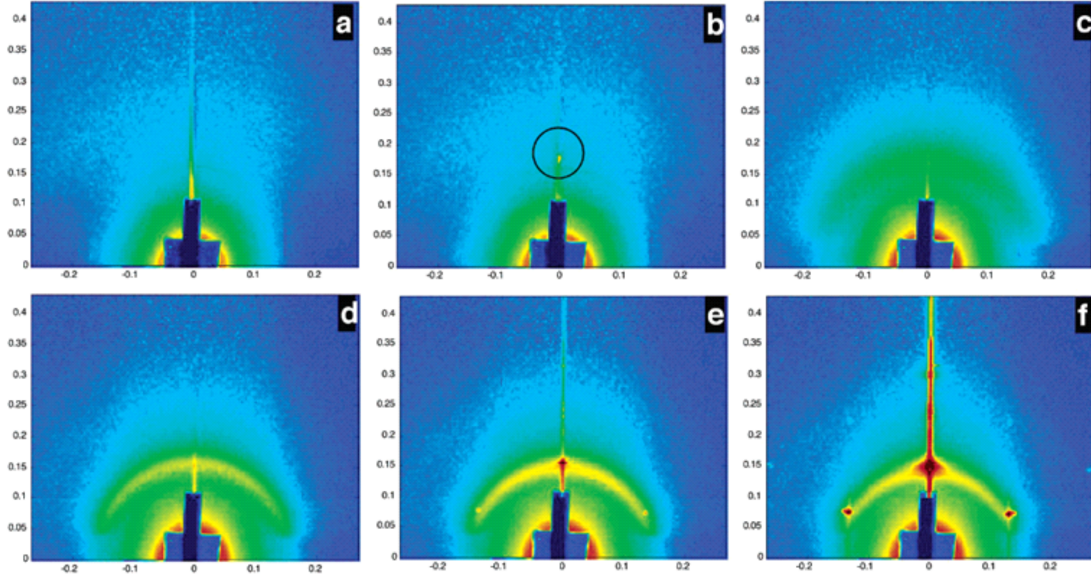
Figure 4.1: GISAXS patterns obtained at different points in time during the formation of a CTAB-templated, 2D-hexagonal thin silica film. The patterns correspond to the following phases: (a) the isotropic phase, (b) the lamellar mesophase, (c,d) the correlated micellar, and (e,f) the hexagonal mesophase. Figure adapted from Reference [105].

organization, where the highest degree of organization seems to correlate with a rather high condensation rate. Combining *in situ* XRD measurements with interferometry suggested a formation mechanism that includes the formation of micelles at the film/air interface, a morphological change from elongated to spherical micelles in the case of 3D-hexagonal and 3D-cubic structures, and the existence of a 3D-hexagonal intermediate phase prior to the formation of a 3D-cubic structure. In the case of the other structures (i.e. 2D-hexagonal and 3D-hexagonal), the authors also observed a transient peak in their XRD patterns. However, unlike in the case of the 3D-cubic structure, they did not attribute this transient peak to a real intermediate structure.

A similar system (namely a silica sol with CTAB as the SDA yielding a 2D-hexagonal mesophase) was also investigated by Doshi *et al.* [105], who carried out time-resolved *in situ* GISAXS studies combined with gravimetric analysis to study the self-assembly of a slowly evaporating film maintained in a horizontal geometry under controlled environmental conditions. This experiment allowed the authors to derive structural and compositional information simultaneously under steady-state conditions. They proposed a mechanism for the formation of the 2D-hexagonal mesophase that included four distinct successive stages during the EISA process, namely an isotropic, a lamellar, a correlated micellar, and finally a 2D-hexagonal geometry, each identified by their respective 2D GISAXS pattern (see Figure 4.1).

At the beginning, there are no reflections visible, indicating the lack of any periodic arrangement. Hence, this pattern was assigned to the isotropic phase. In the subsequent phase, a single Bragg reflection can be seen which indicates – in combination with the absence of out-of-plane reflections and combined with the spot orientation and d-spacing – a smectic ordering parallel to the substrate

surface. The appearance of such a lamellar phase is unexpected from the bulk phase diagram and the authors attributed it to an interfacial effect. Interestingly, this intermittent lamellar phase could only be observed in the presence of a silica precursor and did not appear under similar conditions when no TEOS was added to the precursor solution. At later stages, the lamellar diffraction spot disappears and a broad, diffuse arc appears concomitantly at larger q-values. This pattern can be explained by the presence of spherical or cylindrical micelles showing a low degree of spatial correlation and hence, was assigned to the correlated micellar phase. Over time, the scattering intensified and the width of the arc and its radius decreased. This was attributed to an enhancement of spatial correlation of micelles resulting from their increasing number density and conceivably from their positioning by regular undulations of the lamellar mesophase. Finally, three well-defined Bragg spots defining adjacent 60° central angles with respect to the origin are observed, which can be assigned to a 2D-hexagonal mesophase (*p6mm*) with tube axes oriented parallel to the substrate. Moreover, the authors also observed a disorder-to-order transformation during the EISA process using X-ray reflectivity data and electron microscopy. This transition seems to start at the solid-liquid and at the liquid-air interfaces, and then to propagate to the middle of the film. Similar observations were also made by other groups and for other surfactants, e.g. non-ionic triblock-copolymers [103, 106, 108]. Besides the cooperative mechanism discussed above, in which surfactant molecules and inorganic species combine first to form hybrid intermediate species which then further self-assemble into the final structures, a liquid crystal templating (LCT) mechanism has been discussed for some systems, which suggests that first a stable surfactant mesophase develops, around which the inorganic building blocks are assembled [97, 109, 110]. Both mechanisms are summarized in Figure 4.2. The exact nature of the mechanism that occurs during thin film synthesis most probably depends on the chemical parameters and processing conditions, and often a combination of both mechanisms might operate.

Studies on the mechanism during film growth were also recently published by Jung *et al.* who reported on the *in situ* visualization of domain growth in the self-assembly of silica nanochannels using fluorescence microscopy and atomic force microscopy (AFM) [112]. They observed well-ordered silica nanochannels with domain sizes of up to $\approx 0.3\,\text{mm}$ and showed that transient lamellar structures precedes the formation of hexagonal layers. Furthermore, they discussed that the layer growth follows two distinct pathways (for details see Reference [112]).
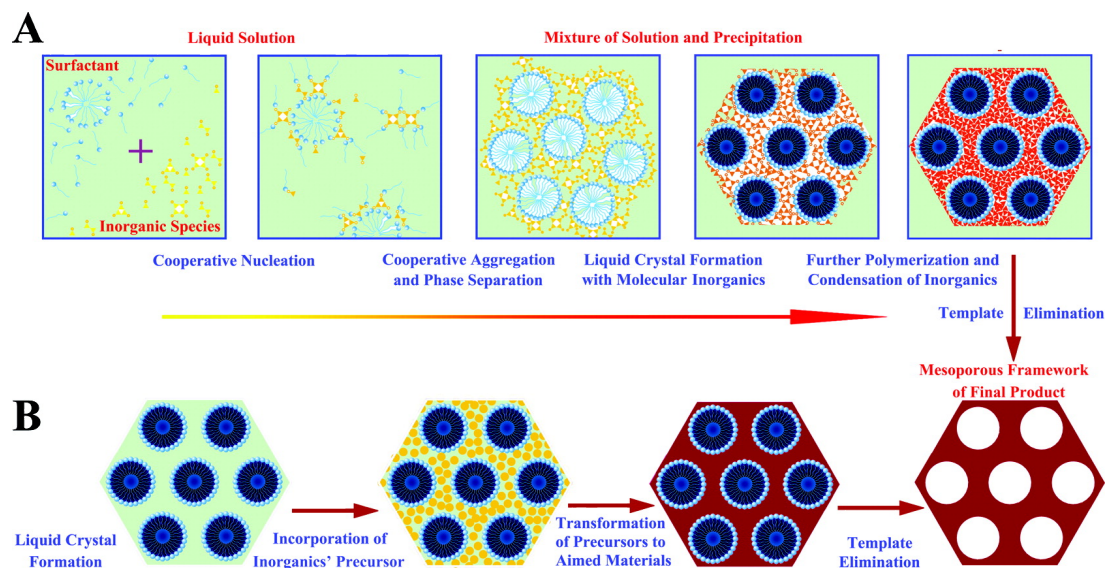
Figure 4.2: Two synthetic strategies for the formation of mesoporous materials: (A) cooperative self-assembly. (B) "true" liquid-crystal templating process. Figure adapted from Reference [111].

4.1.2 Thin Film Deposition and Functionalization Techniques

There are several techniques available for the preparation of thin films, of which a selection is depicted schematically in Figure 4.3 [113]. Out of these, the EISA process described above is compatible with the chemical solution deposition methods, i.e. spin-coating, dip-coating, spray-coating, and meniscus-coating. These are widely employed, because they are cheap and do not require expensive and sophisticated equipment, but rather rely on techniques that are already commonly used in industrial processes. Moreover, they offer a good degree of control over the experimental conditions before and during the self-assembly process.

However, these methods usually do not result in a macroscopic in-plane alignment of the mesopores, most probably due to the lack of a preferential direction during the self-assembly process. Since there are many applications that could greatly benefit from mesopore alignment on a macroscopic scale, such as nanofluidics and nanoreactors [114], oriented growth of nanowires [115], and optoelectronic devices [116], a lot of effort was put into developing methods that can help achieving this goal. These methods include the use of microtrenches [117, 118], external electric [119, 120] and magnetic [121] fields, substrate surface modification [101, 122, 123], and shear flow control [124, 125]. However, these approaches often require specialized equipment or impose constraints on the applicable substrates or surfactants. That is why we recently investigated another technique, namely guided growth in PDMS microchannels [126], which is described in more detail in section 4.2 of this thesis.

Wu *et al.* [117] and Daiguji *et al.* [118] demonstrated that microtrenches that introduce a spatial confinement during the EISA process can influence the mesopore alignment. The trenches were produced by top-down lithographic methods either by directly using the pattern generated from the resist [117], or by transferring the pattern into the substrate *via* reactive ion etching [118]. In both
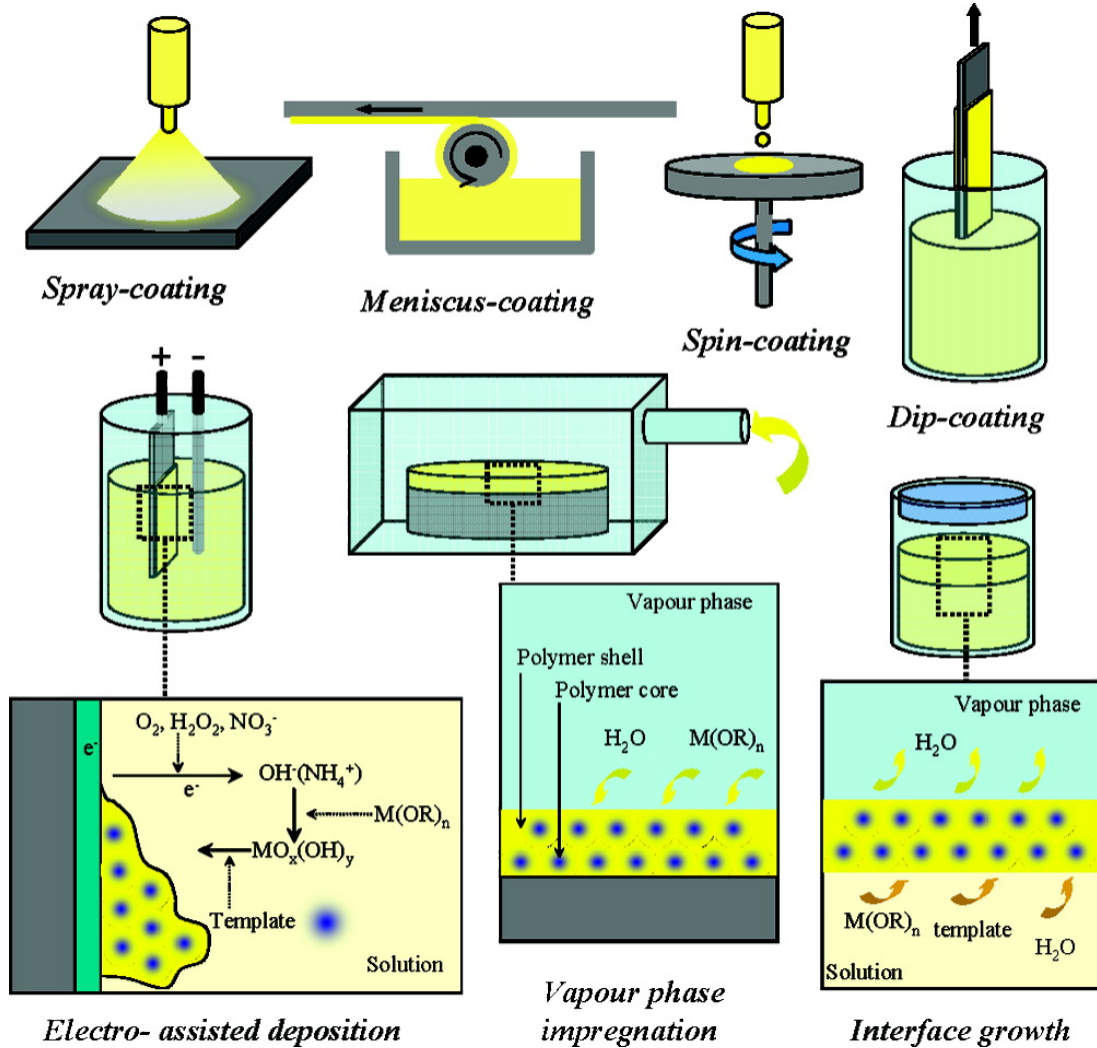
Figure 4.3: Various processing methods used to prepare mesostructured thin films. Figure adapted from Reference [113].

cases, the spatial confinement led to a preferential alignment of mesopores inside the trenches. Wu *et al.* showed in their studies that the alignment depends critically on the aspect ratio of the microtrenches, while Daiguji *et al.* also found an influence of the composition of the precursor solution, the relative humidity during coating and aging, and the chemical properties of the trench sidewalls on mesopore alignment. However, both methods require a clean room and a photolithography or even an electron beam lithography setup, rendering these approaches costly and time-consuming. Trau et al investigated the use of electric fields to induce mesopore alignment. [120] The authors used strong electric fields in combination with a microfluidic system to achieve mesopore alignment. They attributed the alignment effect to both the confined geometry and the presence of the electric field. However, the necessity of strong electric fields at the order of $1500\,\mathrm{V\,cm^{-1}}$ might limit the

applicability of the technique. Furthermore, it also narrows down the choice of the substrate to non-conducting materials and the choice of the template to charged or ionic surfactants, typically resulting in mesoporous silica thin films with small pore sizes. Tolbert *et al.* demonstrated that magnetic fields instead of electric fields could also be used to trigger mesopore alignment [121]. They oriented a silicate-surfactant liquid crystal phase in an 11.7 T magnetic field by heating the samples above their anisotropic-to-isotropic phase transition temperatures, followed by slow cooling (5 °C per hour in 3 °C to 5 °C steps) in the magnetic field and subsequent polymerization of the silica by acidic or acidic-thermal treatment. While this approach also allows for a perpendicular alignment of the mesochannels with respect to the substrate plane, it requires very specialized equipment. Another approach was pursued by Yang *et al.* and Miyata *et al.*, who deposited thin silica films on mica [101] or single-crystal silicon wafers [122] and found that the crystallographic orientation of the substrate surface can influence the mesopore alignment to a certain degree. Miyata *et al.* also suggested another way to introduce mesopore alignment by substrate surface modification, namely by creating a thin polyimide layer on the substrate and subjecting it to a rubbing treatment that can help to align the polymeric chains [123]. This alignment is passed on to the micellar structure of the surfactant molecules and can lead to a macroscopic alignment of the mesopores. The exact formation mechanism that leads to the alignment seems to depend on the matching of the chain length of the hydrophobic part of the surfactant to the chemical structure of the polyimide underlayer [127, 128]. Zhao *et al.* [124] and Naik *et al.* [125] demonstrated that the shear flow exerted on films during dip coating can also influence mesopore alignment to some degree, but the correlation length of the obtained mesostructure might be low in these cases.

Besides macroscopic ordering and mesopore alignment, chemical functionalization of the pore walls of the porous materials is of great importance for many applications, since these determine the host–guest interactions of the system [129–131]. There is a large variety of synthesis strategies that lead to functionalized porous materials [113], of which the co-condensation approach and the chemical grafting approach will be briefly discussed here. In the co-condensation approach, organically modified building blocks (such as functionalized aryl or alkyltriethoxysilanes) are mixed with the inorganic building blocks and the templates in a one-pot reaction [132, 133]. During the self-assembly process, the functionalized silica species will hydrolyze and condense together with the other inorganic silica precursors, resulting in a random incorporation into the silica framework. Another commonly used approach is the post-synthetic grafting of organically modified silica species onto the porous materials. In this approach, the unfunctionalized porous material is first obtained with a standard synthesis protocol, and subsequently subjected to silica species that bear functional groups and that exhibit reactivity towards the free hydroxyl groups present at the surface of the silica pore walls. While the co-condensation approach is simpler and has the advantage of a more homogeneous distribution of the functional groups within the material and its channels, the presence of functionalized silica species during the synthesis can interfere with the delicate formation mechanism of the porous structure and may result in a less well-defined (or, at high loadings, a completely amorphous) material with reduced hydrothermal stability [134].

4.1.3 Characterization of Host–Guest Interactions

Knowing the interactions between the mesoporous host and the guest molecules is essential for many applications. To investigate these interactions, single-molecule microscopy (SMM) is a powerful technique. While measurements of ensemble diffusion of molecules in porous hosts provide information about the overall behavior of the guest in the host, tracking of individual molecules provides insights into the heterogeneity and the mechanistic details of molecular diffusion as well as the structure of the host. With SMM experiments, Zürner *et al.* and Kirstein *et al.* showed how single dye molecules can be used as nanoscale probes to map out the structure of mesoporous silica channel systems prepared as thin films *via* the cooperative self-assembly of surfactant molecules with polymerizable silicate species [12, 135]. The dye molecules act as beacons while they diffuse through the different structural phases of the host: the structure of the trajectories, the diffusivities and the orientation of single molecules are distinctive for molecules traveling in the lamellar and the hexagonal mesophases [136]. These experiments reveal unprecedented details of the host structure, its domains and the accessibility as well as the connectivity of the channel system. In these studies, mostly strongly fluorescent and photostable molecules are used, e.g. terrylenediimide (TDI) derivatives, which can be easily incorporated into mesopores and then individually observed travelling in the host.

To learn more about host–guest interactions, e.g. how a single fluorescent dye molecule travels through linear or strongly curved regions of a mesoporous channel system, a combination of electron microscopic mapping and optical single-molecule tracking experiments were performed by Zürner *et al.* [135]. In this study, an extremely thin mesoporous silica film with a 2D-hexagonal pore arrangement and a pore to pore distance of about 7 nm was synthesized on a silicon nitride membrane (Si_3N_4 membrane). In order to correlate fluorescence and structural features, a fluorescent terrylenediimide (TDI) derivative and 280 nm polystyrene beads were added to the synthesis solution of the mesoporous silica. The polystyrene beads were used as markers and allowed the authors to overlay the transmission electron microscopy (TEM) images with the SMM images. Fast Fourier transform (FFT) directors obtained from a FFT analysis of regions in the TEM images (black bars in Figure 4.4a) indicate parallel aligned channels with strongly curved areas and domain boundaries. By overlaying the SM trajectory over the TEM images it can be clearly seen that the molecule diffuses along the pores. This was the first direct proof that the molecular diffusion pathway through the pore system correlates with the pore orientation of the two-dimensional hexagonal structure (Figure 4.4). Changes of the molecular diffusional movement (and even stopping at less ordered regions) in the channel structure, repulsion by domain boundaries with different channel orientations, or lateral motions between "leaky" channels allow a molecule to explore different parallel channels within an otherwise well-ordered periodic structure. This striking heterogeneity of diffusion behavior only becomes apparent through single-molecule experiments, whereas TEM provides static information only. Moreover, TEM images correspond to an average over the thickness of the film, and while giving a good indication about the general local architecture, they cannot show single defects such as closed channels or open neighboring channels, which can be detected by SMM.
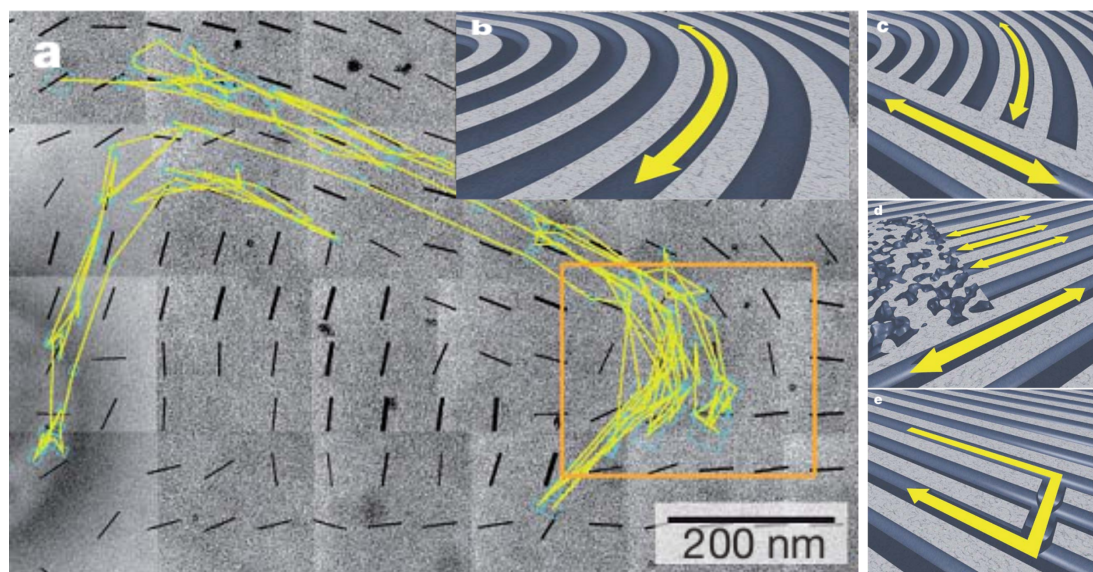
Figure 4.4: (a) Overlay of a single-molecule trajectory (yellow) and multiple TEM images of the silica film (grey) stitched together to provide a macroscopic overview of the sample. The pathway of the molecule is influenced by the domain architecture of hexagonally ordered mesoporous silica pores. Domain boundaries and the local orientation of the pores (black bars) are indicated by the fast Fourier transform of the TEM images. (b-e) Schematic representations of structural elements and molecular movements found in hexagonal mesoporous silica films. Figures adapted from Reference [135].

In the following study, we applied the knowledge that SMM can characterize the structural properties of the mesoporous structure in a non-invasive and direct way and optimized the synthesis conditions that lead to porous silica thin films with highly oriented mesopores.

4.2 Highly Oriented Mesoporous Silica Channels Synthesized in Microgrooves

This chapter is based on the article "Highly Oriented Mesoporous Silica Channels Synthesized in Microgrooves and Visualized with Single-Molecule Diffusion" by Bastian Rühle*, Melari Davies*, Timo Lebold, Prof. Dr. Christoph Bräuchle, and Prof. Dr. Thomas Bein, published in *ACS Nano*, 6(3):1948-1960, 2012.
*These authors contributed equally to this work.
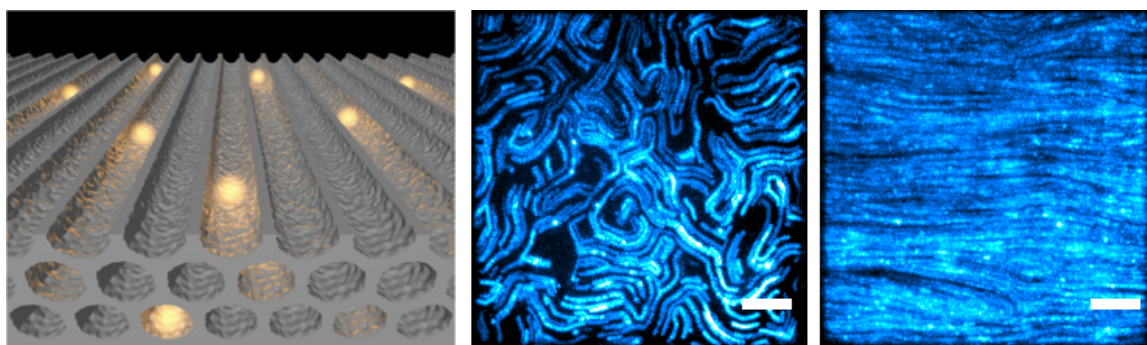
Two-dimensional hexagonal (*p6mm*) mesoporous silica materials have attracted much attention as a host for versatile applications including nanofluidics and nanoreactors [114], oriented growth of nanowires [115], and optoelectronic devices [116]. For these applications, control over pore alignment can be crucial. However, the evaporation-induced self-assembly (EISA) approach [95], which is one of the most common ways to prepare these structures, usually results in small domains with randomly oriented mesoporous channels. This can be attributed to the lack of a preferential direction on the substrate, and a variety of ways that have been reported aimed at introducing a preferential direction of the mesopores on a macroscopic scale, including microtrenches [117], external electric [119, 120] and magnetic fields [121], substrate surface modification [122], and shear flow control [124]. However, these approaches often require specialized equipment or impose constraints on the applicable substrates or surfactants. In the case of employing microtrenches, a clean room and a photolithography or even an electron-beam lithography setup is needed, rendering these approaches costly and time-consuming. The use of external fields requires charged templates such as CTAB, hence, limiting this approach to mesoporous silica with small pores. The other approaches require crystalline substrates with a certain crystallographic orientation or result in channel lengths typically < 1 μm. In this contribution, we describe a general approach for the design of oriented mesoporous silica films with large pores and large channel length (typically around 10 μm) that serve as model systems for the investigation of single-molecule diffusion. This approach is not limited by the need for specific substrates (e.g. nonconductive substrates or substrates with crystalline order), specific templates (e.g. ionic surfactants), or the application of strong electric or magnetic fields that may be difficult to implement. Moreover, to the best of our knowledge, this is the first report of an

in-depth investigation of the structural features (such as correlation length and domain sizes) and dynamical properties (such as guest diffusion) of large-pore silica materials with macroscopically aligned mesochannels.

Our approach was inspired by a technique initially introduced by Whitesides *et al.* as micromolding in capillaries (MIMIC) [119, 120], where an EISA precursor solution is filled into microgrooves defined by a poly(dimethylsiloxane) (PDMS) stamp. This technique is, in principle, compatible with any flat substrate and any surfactant, and no specialized equipment is needed once the masters for the PDMS stamps are obtained. Moreover, the PDMS stamps can be reused, rendering this approach very simple, fast, and cost-effective. We extended the MIMIC approach and investigated mesopore alignment inside PDMS microgrooves using the well-known, uncharged Pluronic F127 tri-block copolymer as a template. We found that the reaction conditions and the surface modification at the solid-liquid interfaces inside the microgrooves can drastically influence the direction of the mesopore alignment. We also introduce single-molecule fluorescence microscopy as a very efficient and powerful tool to gain direct insights into the mesochannel structure, correlation length, and pore directionality in the mesoporous silica films. This method provides unique nanoscale structural information about the pore system and about the interactions of guest molecules with the porous host that cannot be obtained with any other analytical technique (see also the following section 4.2.1 for a more detailed description of this concept) [12, 135–137].

Before the detailed description of the synthetic strategies and how different parameters can affect mesopore alignment, we present some general remarks about the 2D hexagonal (*p6mm*) silica structure itself and the way single-molecule fluorescence microscopy is used as a fast and efficient tool to investigate mesopore alignment and correlation length.

4.2.1 Characterization Techniques

It is known from the literature that an EISA precursor solution of the composition described below (Section 4.2.8) can give a 2D hexagonal phase of mesoporous silica with cylindrical (or elliptical) mesopores lying preferentially in a plane parallel to the substrate [125]. These structures are commonly characterized using X-ray diffraction (XRD) or (cross-sectional) electron microscopy techniques. However, a simple 1D XRD pattern can only give information about the phase (hexagonal or cubic) of a mesoporous silica thin film but says little about its in-plane ordering or the domain sizes. More elaborate X-ray diffraction techniques can also give information about the pore directionality of the mesopores, but these techniques also do not provide much information about the domain size and correlation length of the cylindrical mesopores, and they give only averaged data for a certain area without spatial resolution. On the other hand, electron microscopy top view images of the structure can give information about the phase, the alignment and – to some extent – the correlation lengths of the individual mesopores. However, this only works for the topmost layer in scanning electron microscopy (SEM) (or thin layers in transmission electron microscopy (TEM)), but as will be shown in this work, the alignment of the mesopores can differ drastically between top and bottom layers. In contrast, cross sections can provide information about the orientation at
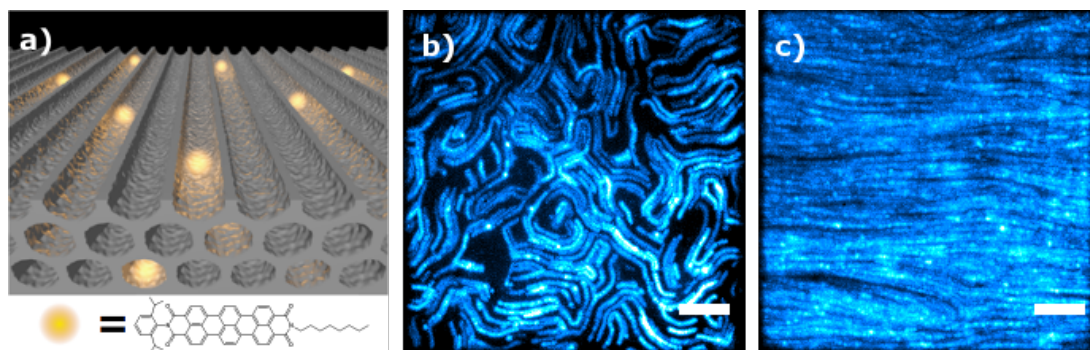
Figure 4.5: Representation of schematic structure and different domain patterns in the mesoporous thin films. Schematic representation of fluorescent dye molecules diffusing inside 2D hexagonally arranged mesopores of a porous silica host (the template is omitted for clarity) (a, top) and the chemical structure of N-(2,6-diisopropylphenyl)-N'-octylterrylene-3,4,11,12-tetracarboxdiimide (As-TDI) (a, bottom). Maximum projection of the individual frames of a movie recorded with a fluorescence microscope at a frame rate of 2.5 fps taken from sample 1, revealing the ordering of the mesoporous structure (false-colored in blue; scale bars are 5 μm; see also movies M1 and M2 on the Supplementary CD) (b,c). The cylindrical mesopores lie in a plane parallel to the substrate, but they do not show macroscopic in-plane alignment (b). The mesopores lie in a plane parallel to the substrate and show a preferential alignment (left-right) on a macroscopic length scale (c).

different heights, but they do not directly provide information about domain sizes of the mesopore channels and they usually require destruction of the sample.

Single-molecule fluorescence microscopy can complement XRD and electron microscopy data [135] and directly provide spatially resolved information about alignment and correlation lengths of mesoporous channels in a fast, direct, and nondestructive way. Moreover, several additional parameters such as the diffusion coefficient of the fluorescent dyes inside the mesopores or even information about defects in the mesoporous structure can be obtained, as will be shown later.

4.2.2 Experimental Conditions

In order to gain information about pore directionality and correlation length, we mixed a fluorescent dye (N-(2,6-diisopropylphenyl)-N'-octylterrylene-3,4,11,12-tetracarboxdiimide (As-TDI)) at a very low concentration (typically $10^{-10} - 10^{-11}$ M) into the EISA precursor solution. During self-assembly of the mesoporous silica structure, the hydrophobic dye is incorporated into the hydrophobic core of the micelles inside the cylindrical mesopores. After solidification of the silica network, the dye remains mobile inside the mesopores, presumably due to the presence of the template acting as a lubricant phase. However, the diffusional movement of the dye molecules is now confined by the silica side walls, so each of the "trapped" dye molecules moves inside a mesoporous channel network, exploring and mapping out the possible pathways. The positions of the dye molecules at different points in time, hence, create a "map" of the mesoporous structure inside the silica host (Figure 4.5). This map can be obtained by recording a movie at the desired position of the sample with a fluorescence microscope (in this work, typically 200-1000 images at a frame rate of 2.5 frames
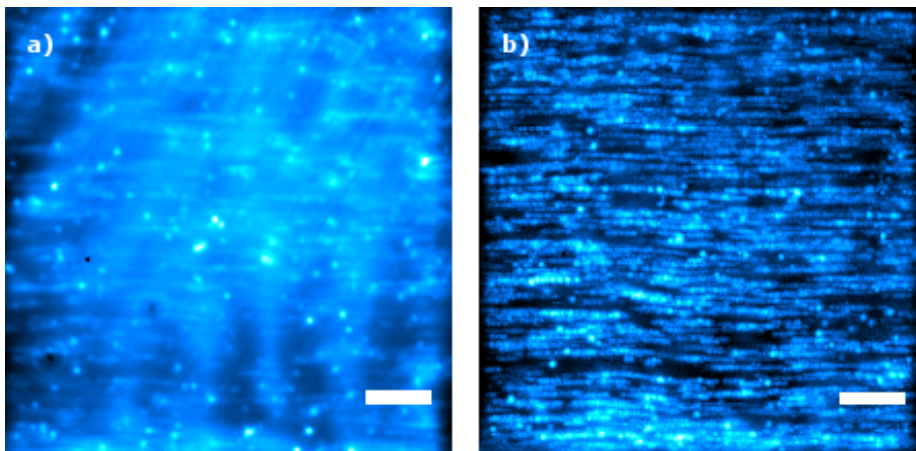
Figure 4.6: Two different ways of obtaining the overlay: by averaging over the individual frames (a) and by using a maximum projection (b). Both images are reconstructed from the same movie taken from sample 2, false-colored in blue, and contrast and brightness were optimized. Both scale bars are 5 μm. The corresponding movie M3 can be found on the Supplementary CD.

per second (fps) were used) and subsequently overlaying the individual frames of the movie in an appropriate way (see next paragraph). This overlay shows directly that the dye molecules do not perform a random walk movement as it would be expected for dye molecules that are merely adsorbed on a surface or, to some extent, dye molecules inside a cubic (*Im3m*) structure, but they rather show a confined movement along certain pathways. Moreover, pore directionality and correlation length can also be directly obtained by analyzing the overlays. The fact that the dye molecules do not diffuse in and out of focus during the recording period of the movies shows that they are inside the 2D hexagonal mesoporous network with the pores aligned preferentially in a plane parallel to the substrate.

The most direct way of creating these overlays would be a summation of (or averaging over) the individual frames of the movie. While this technique works in principle, it has some drawbacks. Most importantly, it overemphasizes stationary fluorescent objects (e.g. constant background, contaminations, immobile dye molecules, defects, etc.) compared to (fast) moving objects because a moving object only contributes intensity to a certain pixel of the overlay when it passes exactly this point in one of the frames of the movie (which might only be the case for a small fraction of the total frames), while a stationary object contributes the same intensity in each frame. For this reason, we used a "maximum projection" in this work, where each pixel in the overlay assumes the maximum value of the corresponding pixels in the individual frames that was reached during the recording time. Hence, the final overlay consists only of the brightest pixels of the movie. This technique treats moving and stationary fluorescent objects more equal and usually provides information-rich images. It is, however, more prone to overemphasizing noise than the averaging method described above since a bright spot in the background that occurs in only one of the frames of the movie is likely to end up in the final overlay. However, with bright fluorophores and a high signal-to-noise ratio, this is usually not a problem (Figure 4.6).
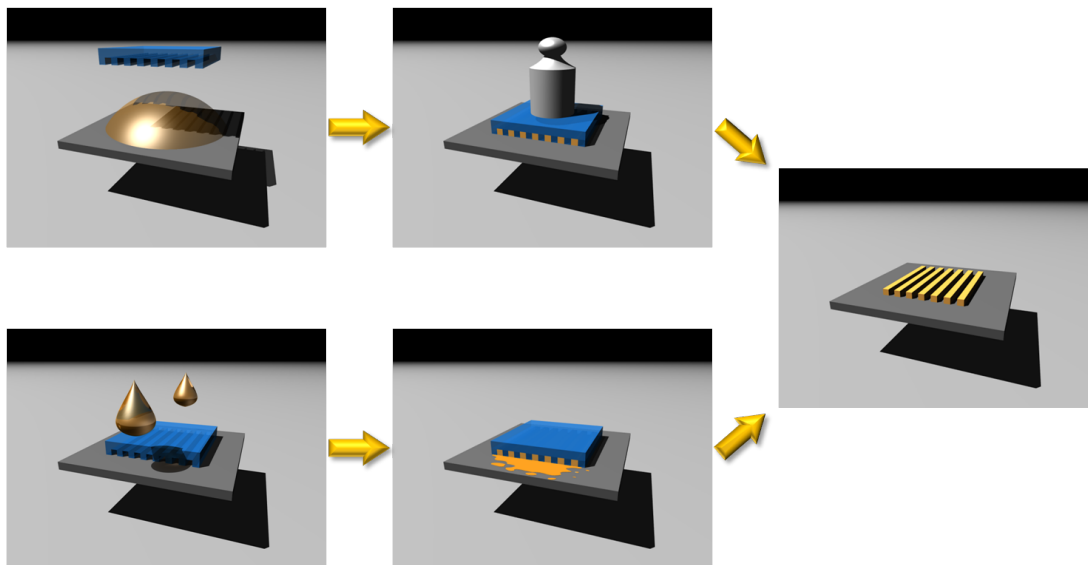
Figure 4.7: Schematic representation of the two approaches used to trigger mesopore alignment by confinement in PDMS microgrooves.

In order to trigger mesopore alignment during the EISA process, the condensation of the precursor solution was performed in confined spaces defined by a PDMS stamp with a stripe pattern. Two different approaches were pursued that are depicted schematically in Figure 4.7. In the first approach ("stamping approach"), a droplet of the precursor solution was deposited on the substrate, the stamp was placed on the latter, and pressure was applied on the stamp in order to achieve dewetting of the surface and to transfer the pattern of the stamp. In the other case ("capillary flow approach"), the stamp was placed on the substrate first, and then a droplet of the precursor solution was applied to both ends of the stamp. The solution gets sucked into the microgrooves defined by the stamp and the substrate by capillary flow. After solidification of the solution, the stamps can be carefully peeled off to obtain the final structure.

In the course of this work, we varied different parameters to investigate their influence on mesopore alignment. In addition to the two approaches described above, we also varied the height-to-width ratio of the microgrooves, the surface modification of the stamp and the substrate, and the synthetic conditions during solidification of the silica framework.

When stamps with microgrooves of a height-to-width ratio of approximately 1:2 (ca. 1.5 µm high and 3.0 µm wide) were used in the stamping approach without further modification of the stamp or the substrate, we found that the mesopores inside the structure tend to align perpendicular to the long axis of the channel (Figure 4.8). This finding is somewhat surprising since according to Aksay *et al.* the formation of end-caps in self-assembled micelle cylinders is unfavored due to their high free energy of formation [120].

As the original goal was to obtain long, well-aligned mesochannels (preferably longer than the microgroove width), we investigated the influence of different synthesis parameters in order to favor
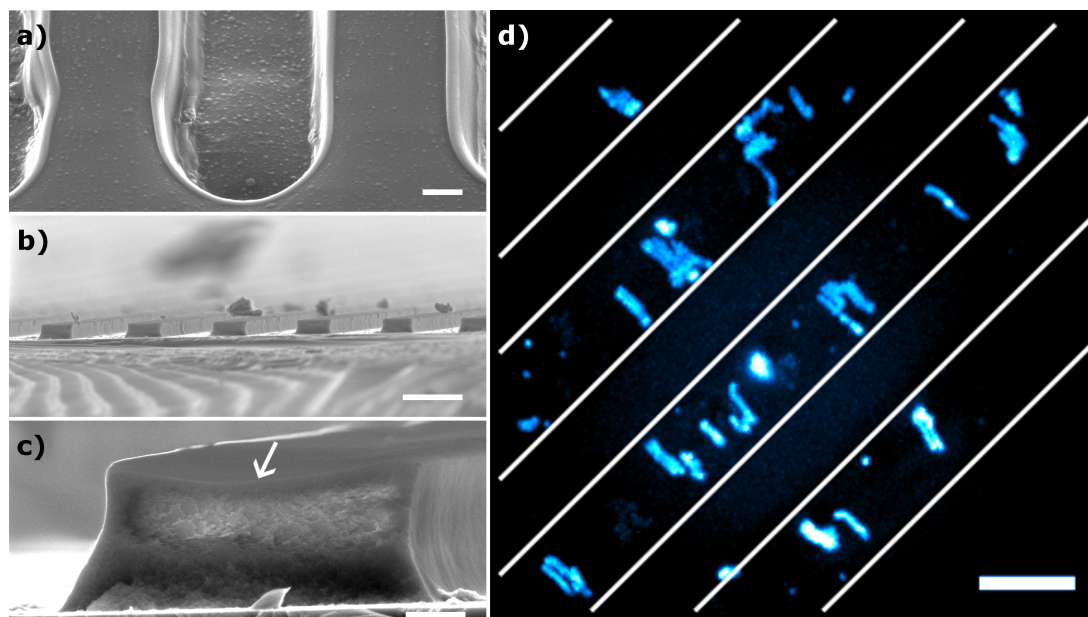
Figure 4.8: Microgrooves and silica mesopore patterns. Microgrooves in the PDMS stamp (scale bar is 1 µm) (a). Mesoporous silica pattern, produced by the "stamping approach" (scale bars are 5 µm and 500 nm, respectively) (b,c). In (c), the top surface of the silica bar is indicated by the arrow. Maximum projection through 500 individual frames of a movie recorded with a single-molecule fluorescence microscopy setup at 2.5 fps taken from sample 3, indicating the orientation of the mesochannels (false-colored in blue; white lines indicate the direction of the microgrooves; scale bar is 5 µm; see also movie M4 on the Supplementary CD) (d).

mesopore alignment along the long axis of the microgrooves. Endo *et al.* showed that in silicon trenches with hydrophobic side walls the mesochannels of SBA-15 films tend to align perpendicular to the long axis of the trenches [118], while in trenches with hydrophilic side walls a parallel alignment was favored. Additionally, it was known from dip-coating experiments conducted by Okubo *et al.* [125] that shear forces can also influence the alignment of the mesochannels favoring pore directionality parallel to the direction of flow (i.e. the dipping direction in their experiments).

With this in mind, we investigated the capillary flow approach, which can provide shear forces during filling of the microgrooves in the stamp, in combination with different modifications of the surface properties of stamp and substrate regarding their hydrophilicity and hydrophobicity. The surface properties of the stamp and the substrate can be varied independently. Modification of the stamp influences the solid/liquid interface at three side walls of the resulting microgrooves, while modification of the substrate influences one solid/liquid interface. Modification of the interfacial properties can indeed strongly influence the alignment of the mesoporous channels. Of the four possible combinations for surface functionalization of the stamp/substrate pair (i.e. hydrophilic/hydrophilic, hydrophilic/hydrophobic, hydrophobic/hydrophilic, and hydrophobic/hydrophobic), best results (meaning preferential alignment of mesochannels parallel to the microgrooves) were achieved by using substrates rendered hydrophobic with PFOTS and stamps rendered hydrophilic by exposure to oxygen plasma and subsequent incubation in an acidic aqueous
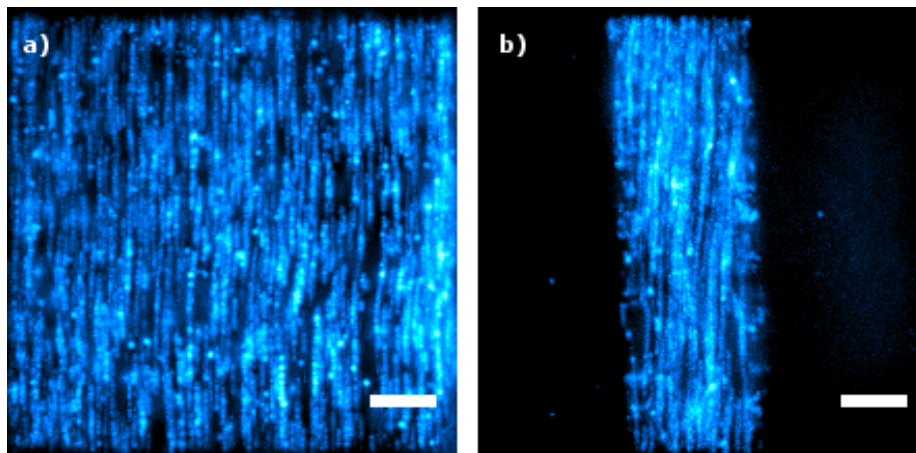
Figure 4.9: Maximum projection indicating the orientation of the mesochannels in a low height-to-width ratio channel (approximately 1:20; sample 2; rotated by 90° for clarity) (a) and a higher height-to-width ratio channel (approximately 1:6; sample 4) (b) (false-colored in blue; both scale bars are 5 µm; see also movies M3 and M5 on the Supplementary CD).

solution of TEOS. Using this combination, very well aligned mesopores could be obtained in narrow microgrooves (typically with a height of 1.5 µm and a width of $10-15$ µm, i.e. a height-to-width ratio smaller than 1:7 to 1:10) in $60-80$ % of the cases. In some cases, parallel alignment could also be observed in extremely low height-to-width ratio grooves with a height of approximately 1.5 µm and a width of ca. 30 µm, that is, a ratio of 1:20 (Figure 4.9).

The parallel alignment usually extends over several millimeters from the ends into the interior of the microgroove, and under favorable circumstances, the entire resulting silica bar of $1-2$ cm length showed alignment of the mesopores. The end regions differ from the middle region mainly in the following aspects. First, the capillary flow in these regions is stronger, indicated by the fact that the movement of the meniscus and hence, the filling of the microgrooves occurs quite fast in the beginning (right after the droplet of the precursor solution was added to the open end of the stamp) but then rapidly slows down. Second, the supply with fresh reactants from excess solution that has not filled the microgrooves is better in these regions. Third, the evaporation rate of the solvent in these regions is different from the middle region since evaporation can occur easier through the open ends of the PDMS stamps.

Interestingly, in some cases, the pore directionality changed abruptly within one channel depending on the height above the substrate (i.e. it changed within different focal planes of the microscope). While close to the substrate, an alignment parallel to the microgrooves could be observed, the orientation changed to a perpendicular alignment at higher positions (Figure 4.10).

We believe that this might be due to the fact that the silica patterns show a concave rather than a flat surface (see Figure 4.8c and Figure 4.11), and the alignment could follow this concave curvature. Similar observations were made by Endo *et al.* for dip-coated films in silicon microtrenches, and the authors attributed the effect to shear flow during solvent evaporation [118].

We also observed that mesopore alignment parallel to the microgrooves can be achieved in higher
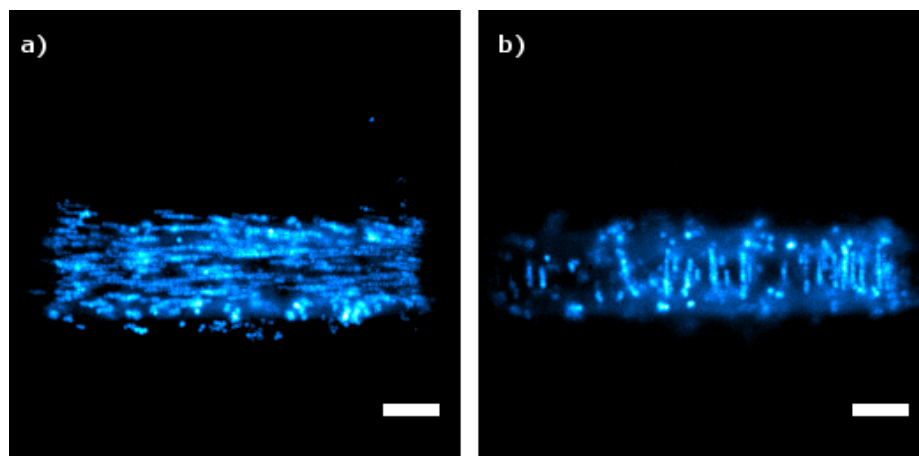
Figure 4.10: Maximum projection taken from sample 2, indicating the orientation of the mesochannels in a focal plane close to the substrate (a) and higher above the substrate (b) (false-colored in blue; both scale bars are 5 µm; see also movie M6 on the Supplementary CD).
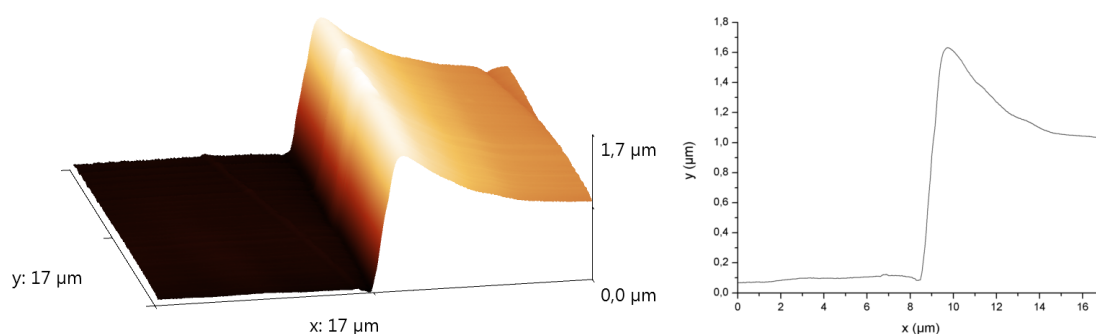

Figure 4.11: AFM Image and line profile from a silica bar showing its concave surface (sample 5); shown is one-half of the bar's cross section.

microgrooves ($4-8$ µm height) by employing the "capillary flow approach" in combination with a hydrophobic (i.e. untreated) PDMS stamp and a hydrophilic substrate. This is interesting for the possible removal of the stamp by controlling the adhesion with the silica bar. In these experiments, we obtained results comparable to the ones shown above regarding mesopore orientation and correlation length when the samples are first incubated in a saturated atmosphere of ethanol at about $22\,°C$ for 21 h and then additionally 24 h at ambient conditions (Figure 4.12). The saturated ethanol atmosphere slows down the evaporation rate of the solvent and hence, the solidification of the silica matrix. However, after these aging times, the structures were found to be sufficiently stable to withstand mechanical stress (such as the stamp removal or SEM preparation) and further treatment such as extraction, and hence, the solidification process was considered to be complete after these times. To determine the structure of the mesoporous silica in the microgrooves, small-angle X-ray scattering (SAXS) experiments and cross-sectional high-resolution scanning electron microscopy (HR-SEM) were performed (Figure 4.13). Both provide evidence for hexagonally arranged mesopores lying in a
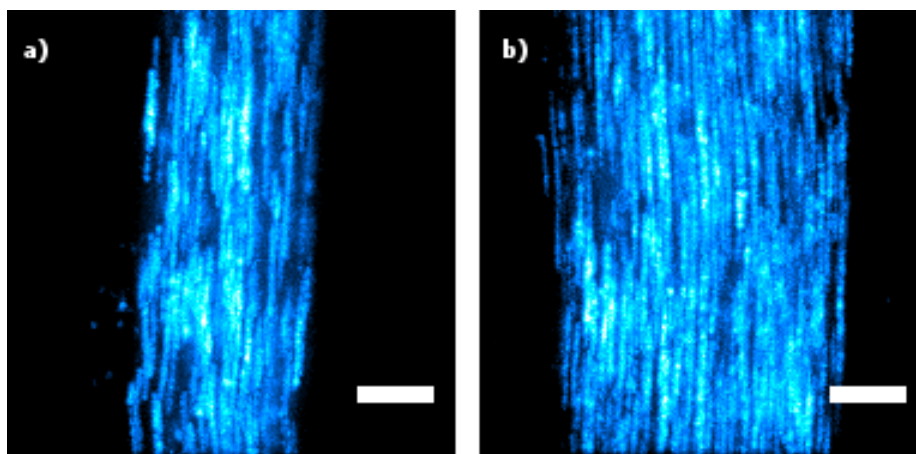
Figure 4.12: Maximum projection taken from sample 6, indicating the orientation of the mesochannels in silica bars of different widths prepared as described above (false-colored in blue; both scale bars are $5\,\mu m$; see also movies M7 and M8 on the Supplementary CD).

plane parallel to the substrate. The cross-sectional HR-SEM images (cleaved perpendicular to the microgroove direction) also indicate the well-ordered state of the mesopores along the long axis of a microgroove. The elliptical shape of the mesopores is typical because of the anisotropic shrinkage in mesoporous silica films during drying. Image analysis of the HR-SEM data gives a mean mesopore width of $6-8\,nm$ and a height of $5-7\,nm$ and a pore-to-pore distance of $12-16\,nm$ horizontally and $9-13\,nm$ diagonally, which is in line with the d spacing of the XRD (100) peak of ca. $7.5\,nm$.
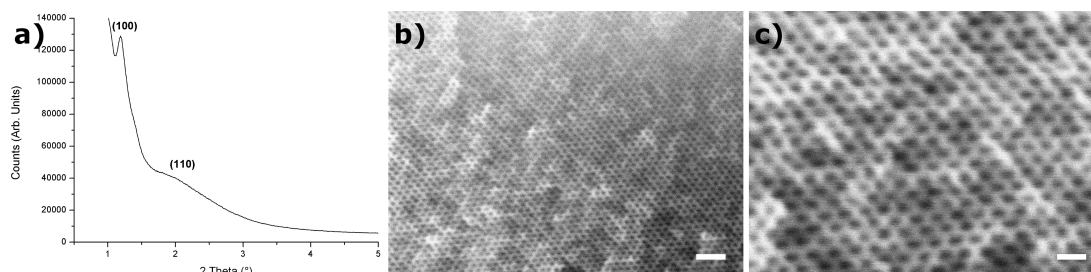
Figure 4.13: Structural analysis of the mesopore system of sample 7. XRD pattern (a) and cross-sectional HR-SEM images (cleaved perpendicular to the long axis of a silicon bar) of mesoporous silica produced as described above (b,c). Scale bars are (b) $50\,nm$ and (c) $20\,nm$.

4.2.3 Detailed Analysis of Trajectories

Samples prepared in the way explained above (i.e. samples $6-9$, see Table 4.1) were also subjected to a more detailed analysis using single-molecule fluorescence microscopy. We obtained high spatial resolution for the pathways of single molecules inside the mesopores, and thus, could analyze the individual channel structures in much more detail. Furthermore, we could gain dynamic information about the diffusion of the molecules in such structures. The main driving force for molecular
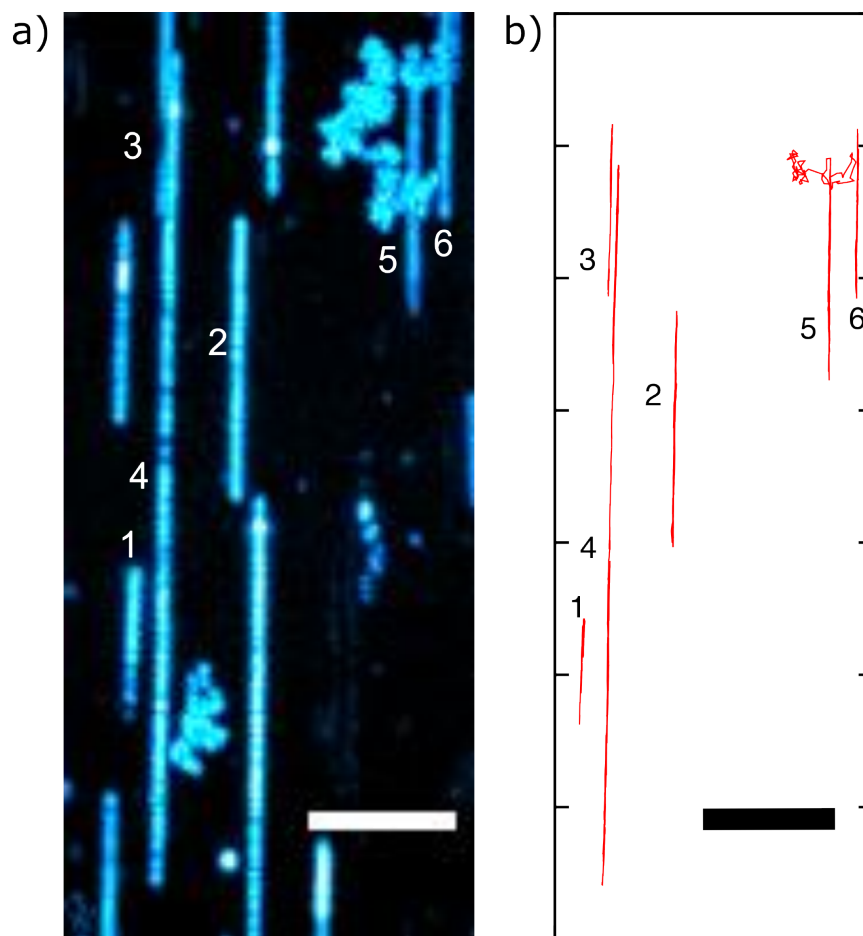
Figure 4.14: Maximum projection and trajectories of single molecules taken from sample 8. Maximum projection of the individual frames of a movie recorded with a fluorescence microscope at a frame rate of 2.5 fps, revealing the pathways of single molecules in the mesoporous structure (a). The mesopores lie in a plane parallel to the substrate and show a preferential alignment on a macroscopic length scale (scale bar is 5 μm; see also movie M9 on the Supplementary CD). Trajectories of all tracked single molecules in (a) in the mesoporous silica structure (b). Scale bar is 5 μm.

movement in these channel systems is Brownian motion, while biased motion due to concentration or structural gradients cannot be fully excluded.

In order to follow the pathway of single molecules with much higher accuracy, the dye concentrations were reduced even further than in the experiments performed before. A direct consequence of such low dye concentrations is the much better separation of the pathways of the single molecules from each other, as shown in Figure 4.14a.

Furthermore, such low concentrations increase the signal-to-noise ratio because of less background. Figure 4.14a shows the high contrast for the traces of 10 single molecules that can be obtained under such experimental conditions. The traces of 6 of these molecules were analyzed in greater detail and show a striking parallel alignment, thus, indicating the high order of the silica channels at a

large scale. Furthermore, the traces show different lengths whereby the trajectory of molecule no. 4 with 27 µm is one of the longest observed in our experiments. However, besides these well-ordered traces, some molecules diffuse in a random manner. These molecules are presumably at the surface of the sample where no guidance by the channel structure exists. Such behavior has been observed in previous studies [12] and is of no further interest here (movie M9 on the Supplementary CD shows the movement of the molecules in Figure 4.14a in time lapse (10x)).

The pathway of a single-molecule in Figure 4.14a was obtained by single-particle tracking, that is, the position of the molecule was determined in each of the 1000 frames of the movie. In each frame, the position can be analyzed by simulating the point spread function of the fluorescent spot with a 2D Gaussian. The positioning accuracy depends on the signal-to-noise ratio and is typically in the range of 6 – 8 nm in our experiments (see also Figure 4.15b). The resulting trajectories are shown in Figure 4.14b for the corresponding pathways of the molecules in Figure 4.14a. These trajectories permit a detailed analysis of the movement of the molecules in the channels and give further information about the structure of these channels. As an example, we concentrated on the trajectory no. 1 in Figure 4.14. This trajectory is enlarged in Figure 4.15.a and extends about 4 µm in the channel direction, which is chosen as the x-direction. In y-direction, however, it varies its width, being broad in the top region and thinning out toward the bottom region. This suggests that the molecule may not only travel up and down in a single channel but, in addition, may switch between neighboring channels through defects in the channel walls.

In order to analyze this in more detail, we determined the distribution of the positioning accuracy for this trajectory, which is depicted in Figure 4.15b. The histogram shows that the most likely positioning accuracy is 6 – 8 nm. This value is clearly smaller than the horizontal pore-to-pore distance (12 – 16 nm; see also Figure 4.13) and hence, allows us to localize the dye molecule and distinguish its position from the position in a neighboring channel.

To analyze a possible switching of molecule no. 1 between adjacent channels, the y-axis was enlarged into the nanometer range while keeping the x-axis in the µm range. The plot of the trajectory in this axis system is shown in Figure 4.15c. It clearly indicates four different distinguishable regions in the y direction marked with four different colors. From this x-y plot of the trajectory, the two separate graphs x(t) and y(t) can be obtained, shown in Figure 4.15d,e. They provide the movement of the molecule as a function of time separated in x and y direction [137]. From the graph y(t) in Figure 4.15e, it is obvious that the molecule jumps in the y direction in four consecutive steps. These distributions can be fitted by four Gaussian curves with a maximum at 42.8 nm (black), 24.6 nm (red), 0.0 nm (blue), and 7.5 nm (green). The distances of these jumps can be correlated to jumps between adjacent channels. The corresponding channel structure in the z-y plane is shown in Figure 4.15f. With this figure, the jumps of the molecule from region 1 (black) to region 4 (green) can be clearly interpreted as switches between adjacent channels. So the molecule starts in channel 1 and then jumps after 31.6 s through an adjacent channel to channel 2 where it then moves for further 93.9 s. Then it jumps again through an adjacent channel into channel 3 and stays there for an additional 39.2 s to finally jump into channel 4. For this pathway in y the jump widths correlate quite well with a horizontal mesochannel spacing of approximately 13 nm, which is in line with HR-
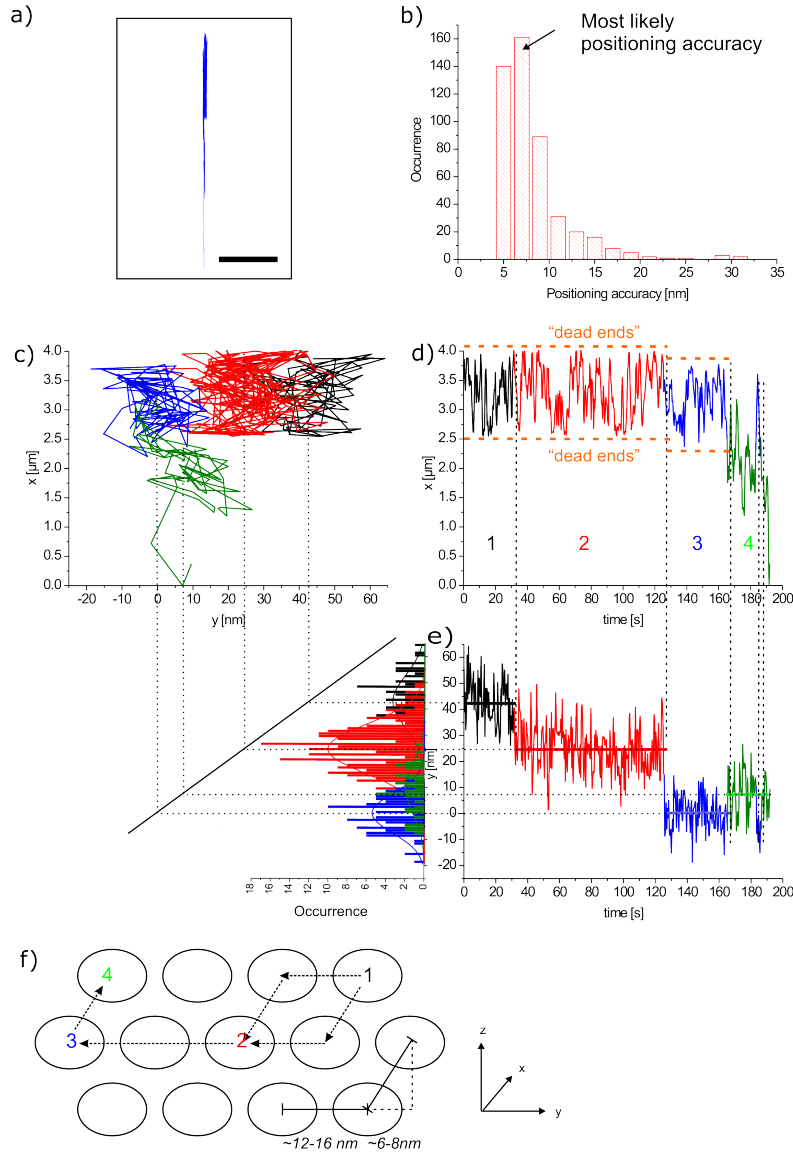
Figure 4.15: Detailed analysis of a trajectory in space and time. Trajectory of molecule no. 1 of the sample depicted in Figure 4.14 (sample 8) with its x-axis parallel to the pore direction, scale bar is 5 μm (a). Histogram of the positioning accuracy for this trajectory; the most likely positioning accuracy is 6 – 8 nm (b). Trajectory of molecule no. 1 with the y-axis in the nanometer range and the x-axis in the um range for better clarity (c). Projection of x and y coordinates as a function of time for the single As-TDI molecule no. 1 shows diffusion of the molecule in at least four distinct neighboring pores (marked with black, red, blue, and green), while the molecule moves back and forth in each pore. Histograms of the y lateral coordinate (bottom left) for the four different time intervals with their Gaussian fits (black, 42.8 ± 1.0 nm; red, 24.6 ± 0.7 nm; blue, 0.0 ± 0.7 nm; green, 7.5 ± 0.2 nm) (d,e). A possible pathway of the single molecule, switching between neighboring channels (f).

SEM images shown in Figure 4.13. However, we cannot distinguish the ± direction of the jumps in z. Therefore, the jumps in the -z direction could also occur in +z or vice versa. From Figure 4.15f,

it is obvious that the jumps from 1 to 2 and 2 to 3 have to occur in larger defects since they include at least two adjacent channels.

Additional information can be obtained from the graph x(t) in Figure 4.15d. This plot shows that the molecule diffuses up and down within a range of approximately 1.5 μm in the first 165 s. The most striking pattern of this part of the trajectory is that the molecule frequently hits the same point at the upper and lower part in the x direction, indicating that there exist two blockades. Thus, the molecule is limited in its pathway along the channel direction by two dead ends. Interestingly, these dead ends seem to be nearly at the same position in x for the first two channels and may change somewhat for the third channel. When the molecule finally switches into channel 4 after 165 s, it finds a pathway that extends further in the x direction for more than 2.5 μm. So the molecule reaches the full extension of the trajectory in the x direction not in one channel but by switching into neighboring channels. A similar picture is obtained by the analysis of the other trajectories shown in Figure 4.14 (data not shown).

In summary, a molecule in such a mesoporous system mainly moves up and down along a single channel that may be blocked by imperfections. However, the molecule eventually finds a defect in the side wall which allows it to switch into a neighboring channel. There it can find its way further along the channel. The impact of imperfections that may block the pathway of molecules may be balanced by the defects in the side walls, allowing the molecule to circumvent dead ends. Thus, the molecule seems to move in a maze with channels oriented along one direction including some small openings to the side and blockades within the channels. This shows the real structure of the mesoporous system including its most relevant defects.

4.2.4 Statistical Analysis

In addition to the structural details discussed above, our experiments reveal the dynamic properties of single molecules in such guest–host systems [136]. For this purpose, a statistical analysis based on the mean-square displacements (MSDs) as a function of time was performed for about 70 single-molecule trajectories for As-TDI. The resulting MSDs are plotted versus time Δt in Figure 4.16a. The MSD graphs are approximately linear for at least the first 10 points (2 orders of magnitude in time) as expected for normal diffusion (Brownian motion). Therefore, it is possible to extract a diffusion coefficient using the relationship between MSD and time for a random walk in one dimension, as the molecules diffuse inside the highly oriented, parallel channels:

$$MSD = \left\langle r^2(t) \right\rangle = 2Dt \,, \tag{4.2.1}$$

where D is the diffusion coefficient. Most of the MSD plots are not perfectly linear for higher values of "Δt" but are slightly curved in the upper regime. This is a further indication of the presence of a confined diffusion, which is consistent with the presence of "dead ends" in the structure as discussed above.

The distribution of the diffusion coefficients for the 70 trajectories is shown in Figure 4.16b. It resembles a Gaussian curve with a mean diffusion coefficient of $1.21 \times 10^5 \, \mathrm{nm^2 \, s^{-1}}$, where the linear
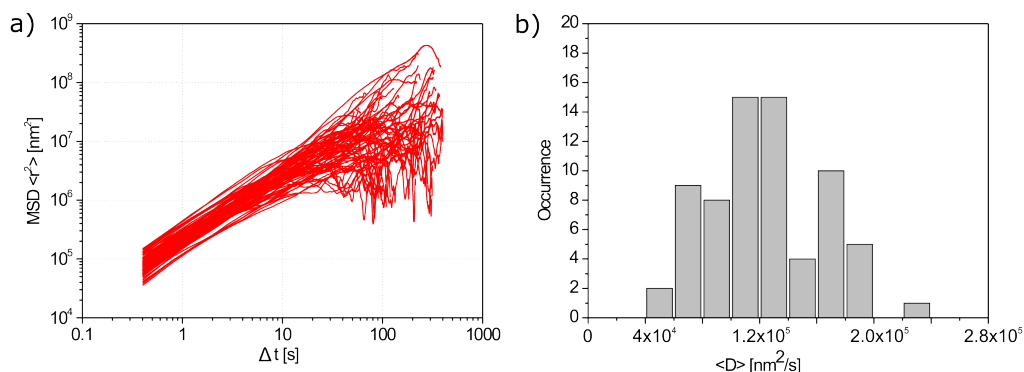
Figure 4.16: Statistical analysis of 70 molecular trajectories. Mean square displacements (MSD) versus time of 70 single-molecule trajectories (As-TDI) (a). Histogram of the mean diffusion coefficient $\langle D \rangle = 1.21 \times 10^5 \, \mathrm{nm^2 \, s^{-1}}$ extracted from the linear part of the individual MSD plots for 70 As-TDI molecules (b).

parts of the MSDs were fitted with a minor deviation of $\pm 2 \times 10^3 \, \mathrm{nm^2 \, s^{-1}}$. The diffusion coefficient of our samples is about 6 times higher for As-TDI than in other comparable known systems, such as Brij-56 [136]. This can be mainly explained by the larger diameter of the pores used in this work (obtained with Pluronic F127 (Ø 6 – 8 nm) compared to Brij-56 (Ø 4 – 5 nm)). In addition, the different interactions between TDI/Brij-56 and TDI/F127 may influence the diffusion coefficient. Furthermore, the width of the distribution shows the heterogeneity of the mesoporous material; that is, it describes the large variation of the interactions between the molecules and their surroundings inside the channels.

4.2.5 Length of the Accessible Pores

The length of the accessible pores can be related to the resulting trajectories as discussed above [12, 135]. Seventy molecules were observed, each for 1000 frames, which corresponds to an observation time of 400 s. In this time, the molecules can move up and down in the channels and switch between them. In order to characterize the possibility of a molecule to diffuse along the channel direction in such a time, a statistical plot of the lengths of the trajectories is given in Figure 4.17. The broad distribution of the histogram in Figure 4.17 shows again the large heterogeneity of the system and was fitted with a log-normal function. The geometric mean and the multiplicative standard deviation of this log-normal distribution are 9.0 $^\times/$ 1.6 µm [138].

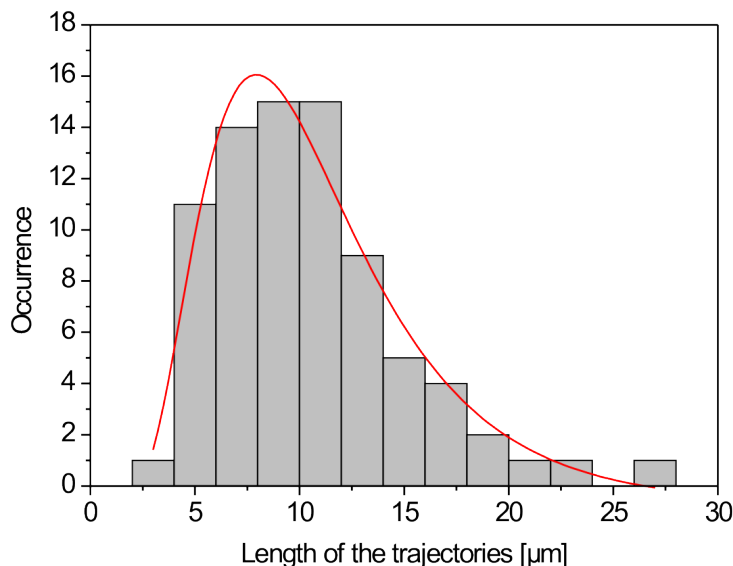**Figure 4.17:** Histogram showing the length of the trajectories of 70 molecules within 400 s. The geometric mean and the multiplicative standard deviation of the fitted log-normal distribution (red line) are $9.0 \; {}^{\times}\!/ \; 1.6 \, \mu m$ [138].

4.2.6 Extracted Mesopores

The results discussed so far demonstrate how the quality of the mesoporous structure can be assessed directly from as-synthesized samples (i.e. the dye molecules are diffusing inside the template-filled mesopores, and the PDMS stamp is not (necessarily) removed from the structures). For many applications, however, freely accessible mesopores that are not filled with a template are desired. The most common way to remove the template inside the pores is to calcine the material, typically at $400 - 500 \, °C$. However, if the quality of the template-free structures is to be investigated by single-molecule fluorescence microscopy similar to the procedure shown above, calcination of the silica material is not an option since it usually results in a high background fluorescence that makes it impossible to identify single fluorophores. We found that this can be avoided by first extracting the template by refluxing in ethanol for 90 min before calcination. The resulting template-free mesoporous silica films can then again be loaded with various guest molecules. In order to examine the nature of the structure after this treatment, we loaded a fluorophore into the channels by submerging the films in an ethanolic solution of the dye at a concentration of approximately $10^{-10} - 10^{-11} \, \mathrm{M}$ for a few hours under mild agitation, followed by rinsing in ethanol. During the incubation in the ethanolic dye solution, the fluorophores can enter the mesoporous network through open mesopores or defects in the structure. However, without a lubricant phase (like the template), the single dye molecules inside the mesoporous channels appear immobile because of strong interactions with active silanol groups at the walls of the channels (at least at the time scales we typically use for
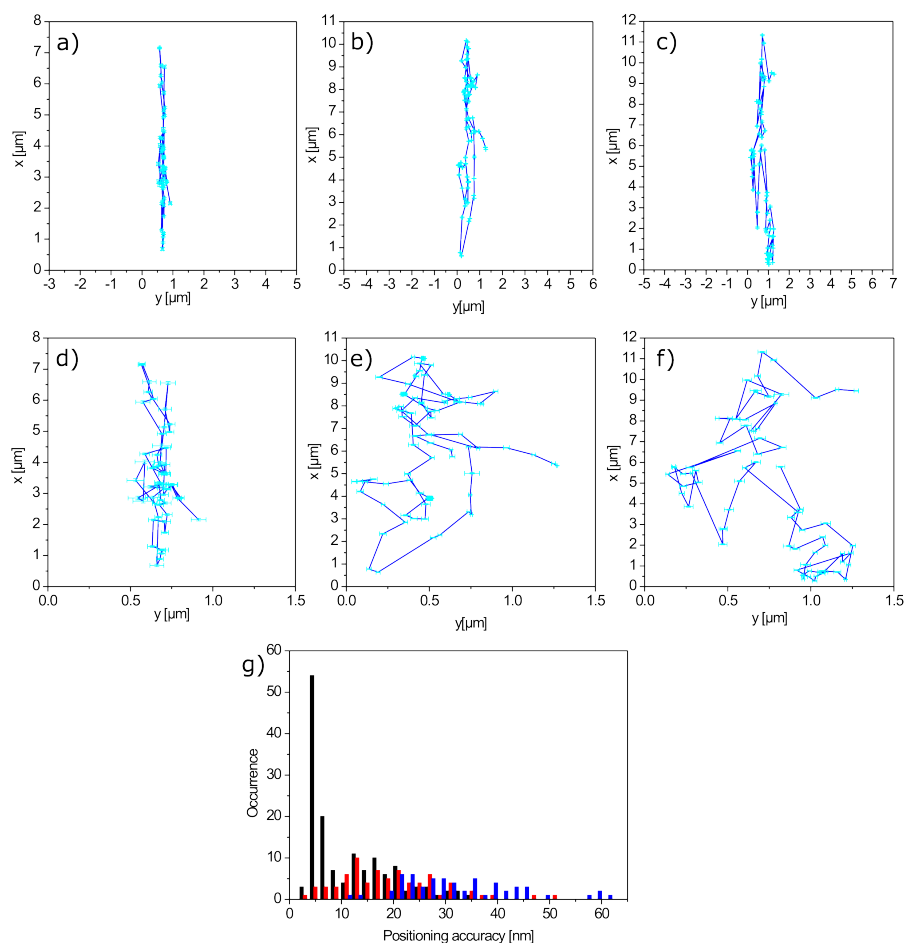
Figure 4.18: Trajectories of single fluorescent dye molecules reloaded into extracted mesoporous silica thin films and exposed to ethanol vapor. Trajectories in sample 9 (a,d) and sample 10 (b,c,e,f) are shown with an axis aspect ratio of 1 in (a-c) and a magnification of the y-axes for the same trajectories in (d-f). All axes are in μm. See also movie M10 (a,d) and M11 (b,c,e,f) on the Supplementary CD. The positioning accuracy in these samples (blue (a,d), black (b,e), and red (c,f)) is plotted in the histogram below (g).

observation, i.e. a few minutes). In order to enable dye movement inside the pores, an atmosphere of an organic solvent such as ethanol or chloroform (good solvents for As-TDI) is required, which results in the formation of a lubricant-like phase inside the pores. In the presence of such a solvent atmosphere, dye molecules inside the pores usually move much faster and also tend to photobleach more rapidly than in unextracted samples. However, it is still possible to follow the movement of single dye molecules and thus, obtain the corresponding trajectories indicating the pathways in the mesoporous silica network, as explained above (Figure 4.18). These trajectories indicate that there still is a preferential direction of diffusion; however, by comparing the trajectories to those shown in Figure 4.14, it is obvious that there are more defects in the silica network after this treatment.

4.2.7 Conclusion

In this study, we have demonstrated that well-defined macroscopic alignment of Pluronic F127-templated, large-pore mesochannels in mesoporous silica can be achieved by confinement in PDMS microgrooves. The influence of various experimental conditions including the way the channels are filled, the surface modification at the solid/liquid interfaces, and the aspect ratio of the microgrooves were investigated. Furthermore, we found that the alignment of the mesochannels can change abruptly from parallel to perpendicular depending on the height within the microgrooves.

We also show how single-molecule fluorescence microscopy can be used to directly assess the mesopore structure of the as-synthesized silica thin films, how a maximum projection can give a global overview on the pore structure, how it can give deeper insights into the real microscopic structure of the mesoporous silica framework, and how it can help us to gain dynamic information about the diffusion of guest molecules inside these materials. The spatial accuracy in these experiments is high enough to observe movements of the dye molecules between individual channels in the mesoporous silica. This high resolution allows us to observe details of long-distance movement of the molecules: in order to travel the very large distances in these highly ordered structures, the molecules circumvent defects by moving to neighboring channels. Finally, we illustrate how solvent-extracted samples can be investigated by this technique and how the defect concentration increases as a result of template removal.

4.2.8 Experimental Part

If not stated otherwise, all chemicals were used as received. Absolute ethanol, tetraethylorthosilicate (TEOS), and Pluronic F127 were purchased from Sigma-Aldrich Co. HCl (1 M) was purchased from AppliChem GmbH. Standard glass coverslips (#1, 22 x 22 mm) were purchased from Gerhard Menzel, Glasbearbeitungswerk GmbH & Co. KG. Hellmanex cleaning solution was purchased from Hellma GmbH & Co. KG. PDMS and PDMS curing agent were purchased from Dow Corning Co. 1H,1H,2H,2H-Perfluorooctyltriethoxysilane (PFOTS) was purchased from abcr GmbH & Co. KG. Aqueous ammonium hydroxide solution (25 %) was purchased from VWR International GmbH.

Exposure to oxygen plasma was carried out with a Femto Plasma System from Diener Electronic typically operated at a power of 50 W and an oxygen flow of $4-5$ sccm. Atomic force microscopy (AFM) images were recorded with a Nanoink NScriptor DPN System in close contact mode. One-dimensional X-ray diffraction (XRD) patterns were obtained with a Bruker D8 Discover X-ray diffractometer using Cu K_{α} radiation. Scanning electron microscopy (SEM) and high-resolution scanning electron microscopy (HR-SEM) images were obtained with a JEOL JSM6500F scanning electron microscope equipped with a field-emission gun, typically operated at an acceleration voltage of 4 kV and 10 kV and a working distance of 10 mm and 7 mm for SEM and HR-SEM, respectively. Single-molecule fluorescence images of the as-synthesized samples with the PDMS stamp still in place were recorded with a wide-field setup, using an Eclipse TE200 (Nikon) epi-fluorescence microscope with a high numerical aperture (NA) oil-immersion objective (Nikon Plan Apo, 100x, NA = 1.40). The fluorescent dye N-(2,6-diisopropylphenyl)-N'-octylterrylene-3,4,11,12-tetracarboxdiimide

(called As-TDI in this work; for the chemical structure, see Figure 4.14 and ref. [139]) with a high photostability and excellent quantum yield were incorporated into the material in single-molecule concentrations ($10^{-10} - 10^{-11}\,\mathrm{mol\,L^{-1}}$). The dye was kindly provided by the research group of Prof. Klaus Müllen (Max-Planck-Institute for Polymer Research, Mainz, Germany).

The molecules were excited at $633\,\mathrm{nm}$ with a He-Ne gas laser (Coherent, $75\,\mathrm{mW}$ maximum at $632.8\,\mathrm{nm}$) with an intensity of $0.3\,\mathrm{kW\,cm^{-2}}$. Their fluorescence was detected with a back-illuminated electron multiplying charge-coupled device (EM-CCD) camera in frame transfer mode (Andor iXon DV897). Incident laser light was blocked by a dichroic mirror ($640\,\mathrm{nm}$ cutoff, AHF) and a band-pass filter (730/140 AHF). One pixel on the camera chip corresponds to $154\,\mathrm{nm}$ on the sample. The individual molecule patterns were fitted by a Gaussian function

$$f(x, y, A, w) = A \cdot e^{-\left(\frac{x - x_0}{w}\right)} \cdot e^{-\left(\frac{y - y_0}{w}\right)},$$

where A and w are the amplitude and the width of the Gaussian curve, respectively. The method was described in detail in previous studies [12, 140, 141]. The resulting positions can be combined frame by frame to form molecular trajectories as described in the text.

The EISA precursor solution was prepared following a procedure from Okubo *et al.* [125] with slight modifications. First, $700\,\mathrm{\mu L}$ of Millipore water and $100\,\mathrm{\mu L}$ of HCl ($1\,\mathrm{M}$) were mixed with $4.4\,\mathrm{g}$ of ethanol (abs.) and $1.0\,\mathrm{g}$ of tetraethylorthosilicate (TEOS) and stirred at $65\,^\circ\mathrm{C}$ for $1\,\mathrm{h}$ in a sealed polypropylene beaker. At the same time, $475\,\mathrm{mg}$ of Pluronic F127 was mixed with $4.4\,\mathrm{g}$ of ethanol and stirred at room temperature for $1\,\mathrm{h}$. Then, the surfactant solution was added to the silica solution, and the resulting clear liquid of molar composition $1.00 : 7.37 \times 10^{-3} : 39.8 : 2.19 \times 10^{-2} : 9.27$ (TEOS/F127/ethanol/HCl/water) was stirred for another $2-4\,\mathrm{h}$ at room temperature. PDMS stamps were fabricated by replica molding from photolithographically patterned masters using standard techniques. The final thickness of the stamps was typically about $1.0-1.5\,\mathrm{mm}$. The substrates were cleaned by submerging them in a water/Hellmanex solution at $60\,^\circ\mathrm{C}$ for $1\,\mathrm{h}$, followed by ultrasonic agitation for $3\,\mathrm{min}$ and rinsing with DI water. For further surface modification, the cleaned substrates were treated by submersion in piranha solution for $1\,\mathrm{h}$ or by exposing them to oxygen plasma for $15\,\mathrm{min}$. When hydrophilic substrates were desired, the substrates were directly used after this treatment. For hydrophobic substrates, the activated glass coverslips were placed in a desiccator alongside a Petri dish with 1H,1H,2H,2H-perfluorooctyltriethoxysilane (PFOTS), the pressure was reduced until the boiling pressure of the silane was reached at ambient temperature (approximately $7 \times 10^{-2}\,\mathrm{mbar}$), and the substrates were incubated in the resulting silane atmosphere for $3-4\,\mathrm{h}$. When hydrophobic stamps were desired, the PDMS replica molds were used without further modifications because PDMS is intrinsically hydrophobic. To render the PDMS hydrophilic, it was exposed to oxygen plasma for $90\,\mathrm{s}$ and then submerged in an aqueous solution of TEOS ($3\,\mathrm{mM}$) and HCl ($96\,\mathrm{mM}$) for $2\,\mathrm{h}$. It is well-known that functionalized trialkoxy- and trichlorosilanes can be grafted to reactive surface hydroxyl groups from the liquid or the gas phase [142, 143].

In some cases, extraction of the template was achieved by refluxing the samples in ethanol (abs.) for $90\,\mathrm{min}$ after they had been subjected to an $\mathrm{NH_3}$ atmosphere obtained by incubating the samples in a closed container next to a Petri dish containing an ammonium hydroxide solution ($25\,\%$ in water) at

room temperature for $10-15\,\text{min}$ (to promote silica condensation). Subsequently, the samples were calcined in air by first heating at $60\,°\text{C}$ for $90\,\text{min}$ (ramp: $1\,°\text{C}\,\text{min}^{-1}$), then at $160\,°\text{C}$ for $90\,\text{min}$ (ramp: $1\,°\text{C}\,\text{min}^{-1}$), and finally at $400\,°\text{C}$ for $4\,\text{h}$ (ramp: $1\,°\text{C}\,\text{min}^{-1}$).

An overview of the different samples discussed in this work including precise treatment and synthesis conditions can be found in Table 4.1.

Table 4.1: Overview of the samples discussed in the text[1]

| Sample Code	Microgroove height [µm]	Surface Properties of PDMS Stamp	Surface Properties of Glass Substrate	Microgroove Filling Method	Ageing Conditions	Post Treatment
1	2	Hydrophilic	Hydrophobic	Capillary Flow	48 h at RT and amb. hum.	None
2	2	Hydrophilic	Hydrophobic	Capillary Flow	48 h at RT and amb. hum.	None
3	2	Hydrophobic	Neutral (untreated)	Stamping	48 h at RT and amb. hum.	None
4	2	Hydrophilic	Hydrophobic	Capillary Flow	48 h at RT and amb. hum.	None
5	2	Hydrophilic	Hydrophobic	Capillary Flow	48 h at RT and amb. hum.	Removal of PDMS Stamp
6	4-8	Hydrophobic	Hydrophilic	Capillary Flow	21 h at RT and sat. EtOH atm. and 24 h at RT and amb. hum.	None
7	4-8	Hydrophobic	Hydrophilic	Capillary Flow	21 h at RT and sat. EtOH atm. and 24 h at RT and amb. hum.	Removal of PDMS Stamp and standard SEM cross-section preparation
8	4-8	Hydrophobic	Hydrophilic	Capillary Flow	21 h at RT and sat. EtOH atm. and 24 h at RT and amb. hum.	None
9	4-8	Hydrophobic	Hydrophilic	Capillary Flow	21 h at RT and sat. EtOH atm. and 24 h at RT and amb. hum.	Removal of PDMS Stamp, incubation in NH_3-atm., Extraction in EtOH (reflux), calcination in air
10	4-8	Hydrophobic	Hydrophilic	Capillary Flow	21 h at RT and sat. EtOH atm. and 24 h at RT and amb. hum.	Removal of PDMS Stamp, incubation in NH_3-atm., Extraction in EtOH (reflux), calcination in air

[1]See the experimental part for further details on the entries of the table; rt = room temperature (typically $22-25\,°C$); amb. hum. = ambient humidity (typically $30-60\,\%$); atm. = atmosphere

4.3 Electrophoresis of Single Dye Molecules in Highly Oriented Mesoporous Silica Channels

In the previous section 4.2 we have demonstrated how single-molecule fluorescence microscopy can be used to assess the structure of highly oriented mesoporous silica channels synthesized in poly-(dimethylsiloxane) (PDMS) microgrooves. In an extended single molecule study, these highly oriented mesopores are used, to perform electrophoresis experiments.

Parts of this chapter are based on a manuscript of an article by Melari Davies*, Bastian Rühle*, Dr. Chen Li, Prof. Dr. Klaus Müllen, Prof. Dr. Thomas Bein, and Prof. Dr. Christoph Bräuchle, which is currently in preparation.
*These authors contributed equally to this work.
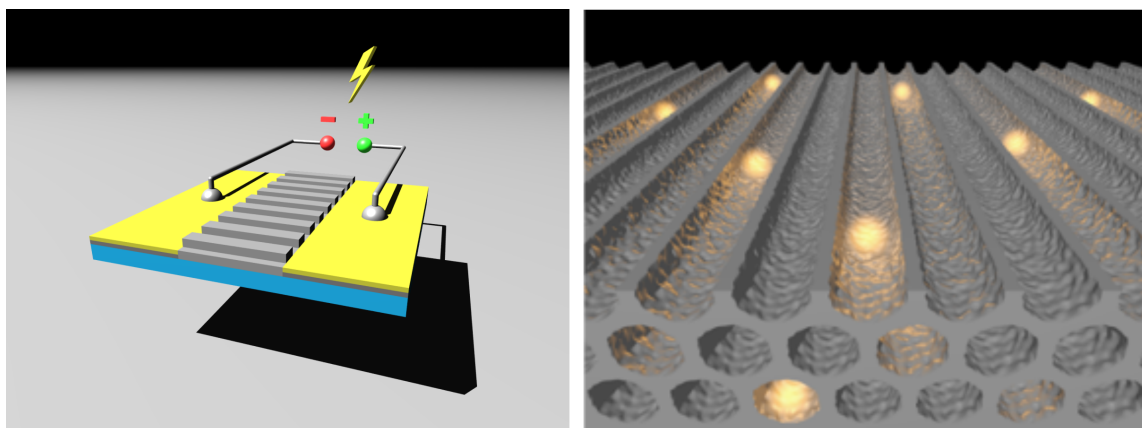
Electrophoresis and electrochemical sensing are important tools in biochemistry and biology and are commonly used for separation and detection of biomolecules. The separation and detection result from the different mobility of these molecules depending on their size, charge and conformation as well as their interaction with the host material. Extending these concepts to mesoporous silica host systems could be very beneficial due to the enormous structural and functional versatility. Although there are several examples in which modified mesoporous silica is used for separation and as an electrode coating material for electrochemical sensing [144–147], little is known about the detailed behavior and interactions of the guest species inside the mesoporous silica host channels on a single-molecule basis.

We investigated mesoporous silica thin films with a highly ordered mesoporous structure in order to gain deeper insights into the triggered movement under the influence of an electric field, pure diffusional behavior and the interactions of charged guests inside the porous silica host. It is, to the best of our knowledge, the first time that a direct observation of the movement of charged guest species in mesoporous silica hosts is described and analyzed. This analysis was carried out using single-molecule microscopy, which allows for a detailed investigation of the diffusional pathways and

the triggered movement of uncharged and charged dye molecules under the influence of an electric field and gives deeper insights into the interaction of the guest molecules with their porous host and with the electric field. Moreover, a separation of differently charged molecules inside the host structure could be directly observed on a single-molecule basis.

We have recently demonstrated that defined macroscopic alignment of large-pore mesochannels (diameter about 9 nm) in mesoporous silica can be achieved by confinement in poly(dimethylsiloxane) microgrooves. The detailed synthesis and analysis of these systems has been described in section 4.2 and is therefore described only briefly in section 4.3.9. In the present work we demonstrate the feasibility of electrophoresis experiments in such highly oriented silica channels. For our investigations, differently charged fluorescent dye molecules were incorporated into mesoporous silica channels in single-molecule concentrations ($10^{-10} - 10^{-11}$ M) and directly influenced by an externally applied electric field. We also carried out investigations with uncharged dyes to ensure the integrity of the mesoporous structure under the experimental conditions, i.e. the presence of strong electric fields. All dyes, we have used for the respective experiments are summarized in Figure 4.19.

By determining the position of the molecules in each frame of a movie recorded with a wide-field fluorescence microscope and overlaying the individual frames of the movie, the pathway of the molecules can be depicted. Specifically, each pixel in the overlay assumes the maximum value of the corresponding pixels in the individual frames that was reached during the recording time. The final overlay consists only of the brightest pixels of the movie. We call this procedure a "maximum projection" (see also section 4.2 and Rühle *et al.* [126]). This method gives a global overview of the pore alignment. In addition, single-molecule tracking allowed for a more detailed structural and dynamic analysis of the guest molecule movement.
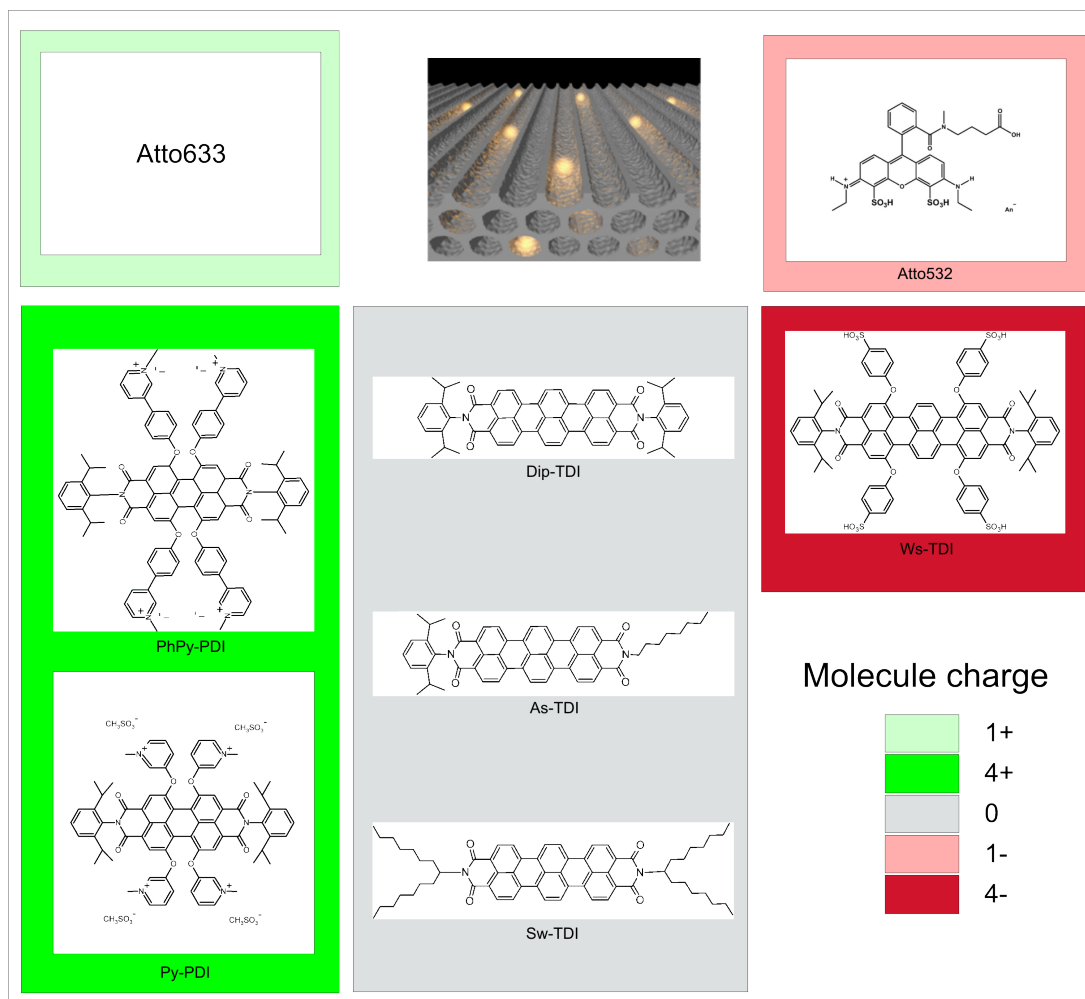
Figure 4.19: Overview of the dye molecules incorporated into the mesoporous silica channels. Atto633 and Atto532 are commonly available dyes with one charge (Atto633 is positively charged and Atto532 is negatively charged). PhPy-PDI and Py-PDI are both four-times positively charged with a perylenediimide (PDI) chromophore. The neutral dyes, Dip-TDI, As-TDI, SW-TDI and also the four-times negatively charged Ws-TDI molecules have a terrylenediimid (TDI) core.

4.3.1 Diffusional Behavior of Dip-TDI, As-TDI and Sw-TDI

In order to verify the mesopore alignment of the porous host material, we used uncharged guest molecules (Dip-TDI, As-TDI and Sw-TDI, chemical structures see Figure 4.19) in a preliminary experiment. The movies recorded with our wide-field microscope (see movie M12, movie M13 and movie M14 on the Supplementary CD) clearly display a structured movement of these TDI molecules parallel to the pore direction of the silica channels. The maximum projections of the individual frames of the movies directly depict the pathways of the molecules and thus, the macroscopic alignment of the mesoporous channels (Figure 4.20a,b,c). Single-molecule trajectories reveal the structure of the channels in even more detail, exhibiting defects and dead ends present in the porous

system (Figure 4.20d,e,f). By analyzing the trajectories of the molecules in space and time one can even observe the switching of guest molecules from one channel to another channel through defects in the silica walls, as also discussed in section 4.2.
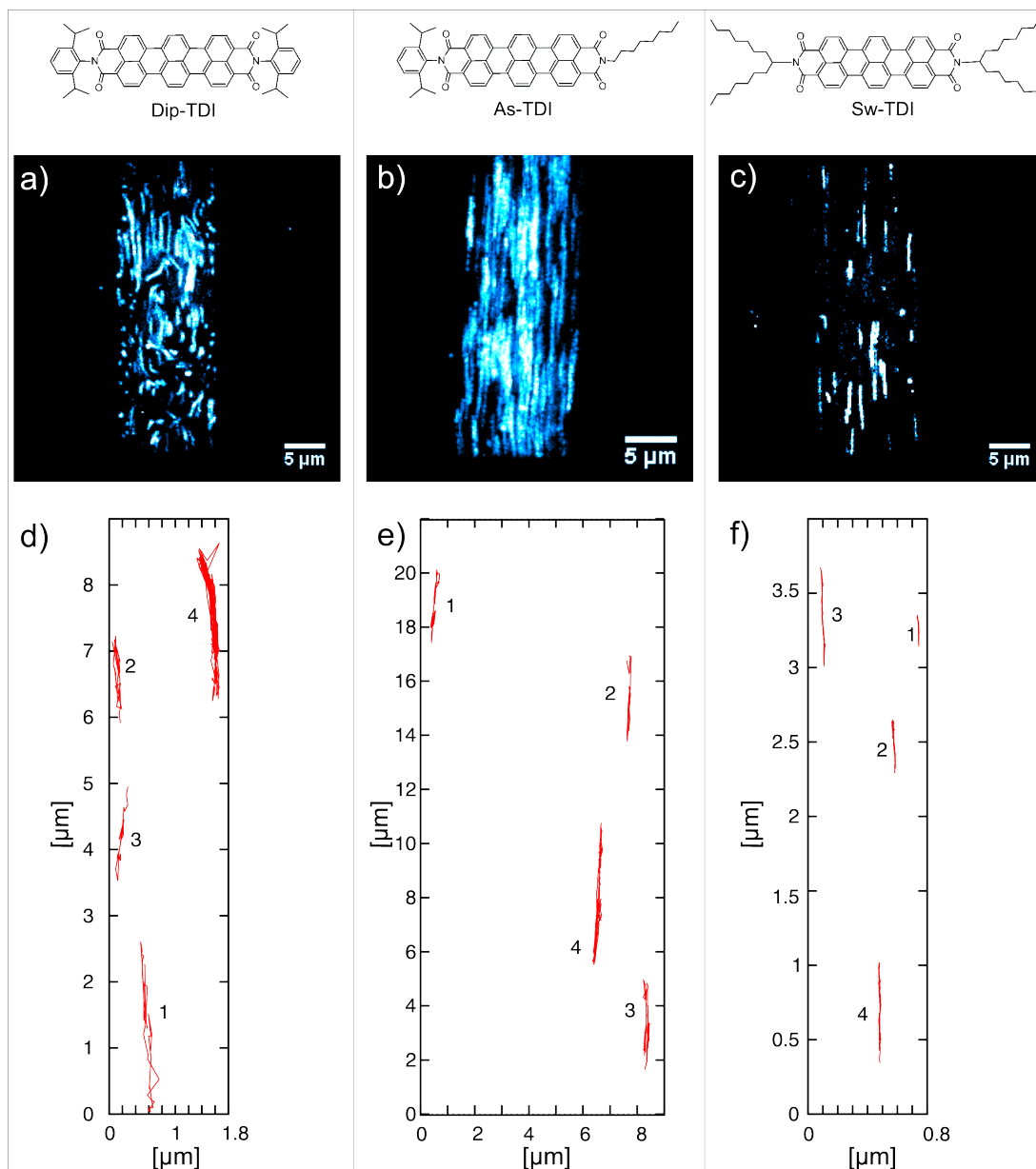
Figure 4.20: Maximum projection of several consecutive wide-field images indicating the alignment of the mesoporous silica channels. (a) Dip-TDI (N,N'-bis(2,6-diisopropylphenyl)terrylene-3,4,11,12-tetracarboxdi-imide), (b) As-TDI (N-(2,6-diisopropylphenyl)-N'-octylterrylene-3,4,11,12-tetracarboxdiimide) and (c) Sw-TDI (N,N'-(pentadecan-8-yl)terrylene-3,4,11,12-tetracarboxdiimide) molecules were incorporated as fluorescent guest dyes into the mesopores during the synthesis in order to gain information about pore directionality. Exemplary single-molecule trajectories of (d) DIP-TDI, (e) As-TDI and (f) Sw-TDI reveal the structure and alignment of the mesopores.
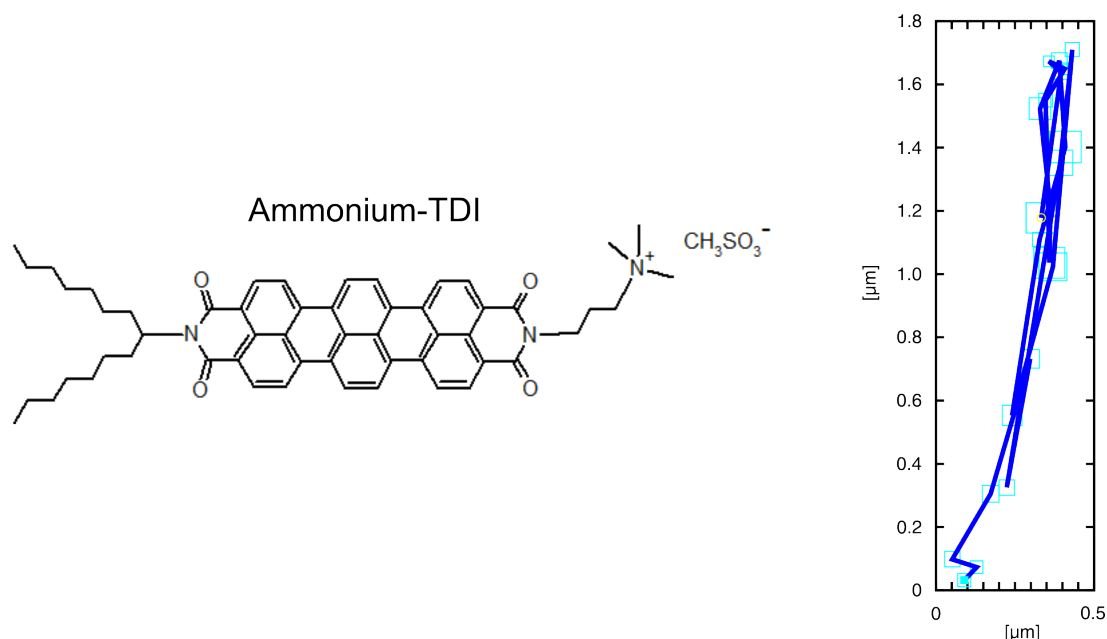
Figure 4.21: Chemical structure of Ammonium-TDI and an exemplary single-molecule trajectory of the dye in oriented silica mesopores.

4.3.2 Diffusional Behavior of Ammonium-TDI

For electrophoresis experiments in highly oriented mesopores a new positively charged terrylene derivative was synthesized in the group of Prof. Klaus Müllen. The chemical structure of this dye, depicted in Figure 4.21, is comparable to the terrylene derivatives used in section 4.3.1, especially to the structure of Sw-TDI. The molecules were incorporated into the highly oriented mesopores and observed with a wide-field microscope. The single-molecule trajectories display structured movement of the molecules. Exemplary, one trajectory is presented in Figure 4.21. However, the diffusional behavior of the molecules was not affected by applying an electric field. This raises the question if the dye molecules remained charged after incorporation into the porous host. Possibly shielding effects, caused from counter ions in the solution which can form a cloud around the charged molecules, partially shielding the charged dyes from the electric field (E). So, these dye molecules were not used for further electrophoresis experiments.

4.3.3 Diffusional Behavior of PhPy-PDI *versus* As-TDI

By incorporating other charged dye molecules, e.g. PhPy-PDI with four positive charges (all used dyes are listed in Figure 4.19) into the same samples we observed an effect of the electric field. However, the diffusional pathways were more random as expected. To be sure that the structure of the sample is highly oriented, we mixed uncharged As-TDI molecules with charged PhPy-PDI molecules (Figure 4.22a) and incorporated them into the same sample. PhPy-PDI was excited with a 532 nm diode Laser in order to be able to spectrally separate its fluorescence signal from the

signal of As-TDI molecules which were excited with a He-Ne-Laser (633 nm), and we detected both fluorescence signals simultaneously in different channels. Channel 1 depicts the fluorescence signal of PhPy-PDI molecules and Channel 2 displays the signal of As-TDI molecules. The uncharged molecules (As-TDI) indicate structured movement up and down (see movie M15 on the Supplementary CD and also maximum projection in Figure 4.22b) while the charged molecules (PhPy-PDI) moved more randomly (see movie M16 on the Supplementary CD and also maximum projection in Figure 4.22a). By switching on the electric field $(1200\,\mathrm{V\,cm^{-1}})$ we could observe a directed movement of the charged PhPy-PDI molecules before photobleaching (movie M17 on the Supplementary CD). As expected, the diffusional movement of the uncharged As-TDI molecules was not affected by the electric field. They continued moving in a structured way exactly as they did without the electric field. We consider this a strong indication that the highly ordered sample structure is maintained under the influence of a (strong) electric field and that the rather unstructured movement of the charged dyes is due to other effects than the destruction of the ordered mesoporous structure (see also discussion below).

Figure 4.22: Maximum projection of the individual frames of a movie recorded with a fluorescence microscope at a frame rate of 2.5 frames per second (fps), revealing the pathways of (a) PhPy-PDI and (b) As-TDI molecules in the same sample. PhPy-PDI molecules were excited with 532 nm and As-TDI molecules were excited with 633 nm. So, the fluorescence signals of both dyes could be spectrally separated in Channel 1 (left) and Channel 2 (right).

4.3.4 Diffusional Behavior of Atto633 *versus* As-TDI

In a further experiment, we introduced charged Atto633 molecules and uncharged As-TDI molecules into the same sample. Both dyes were excited with a 633 nm He-Ne Laser and detected in the same channel. We discovered two different species. Both could be clearly distinguished due to their physical properties. The species that moved randomly was bleaching faster and since it is known that Atto dyes are not as photostable as TDI dyes [33], we assigned these signals to Atto633 molecules. The molecules which moved in a structured way had a good photostability and could therefore be identified as As-TDI molecules (see movie M18 on the Supplementary CD). Figure 4.23a depicts the maximum projection of all frames of the movie M18 (Supplementary CD) recorded with our fluorescence microscope, revealing the pathways of both species of single molecules in the mesoporous

structure. A maximum projection of the last 100 frames of the same movie M18 expose the pathway of only one species (As-TDI) moving in a structured way (Figure 4.23b), while all unstructured Atto633 molecules have already been photo-bleached.

In order to compare the patterns of movement of both dyes, exemplary trajectories of each dye are plotted in Figure 4.23c. As-TDI molecules (red trajectories in Figure 4.23c) move up and down in y-direction (which is the direction of the mesoporous silica channels) in a structured way, while Atto633 molecules (green trajectories in Figure 4.23c) move rather randomly, having a greater propagation in x-direction and lacking the preferential movement in y-direction.
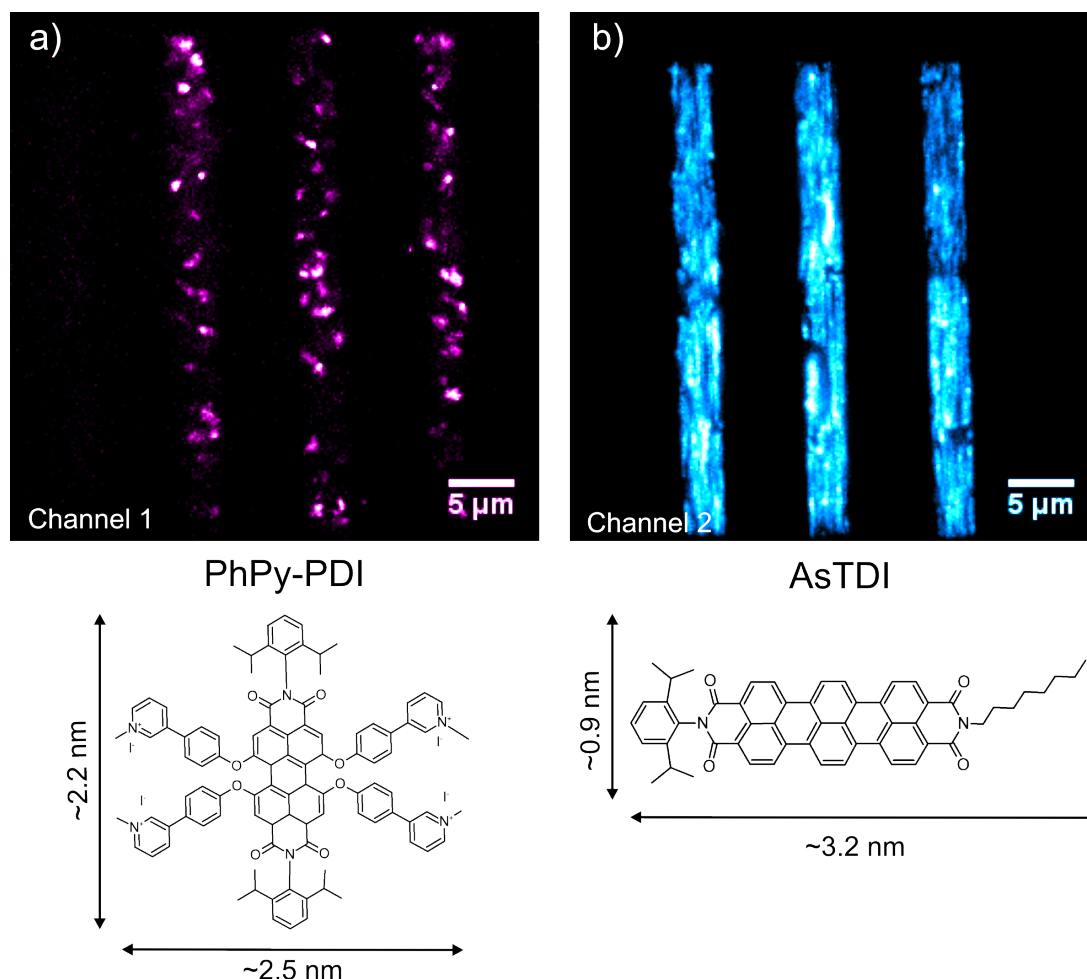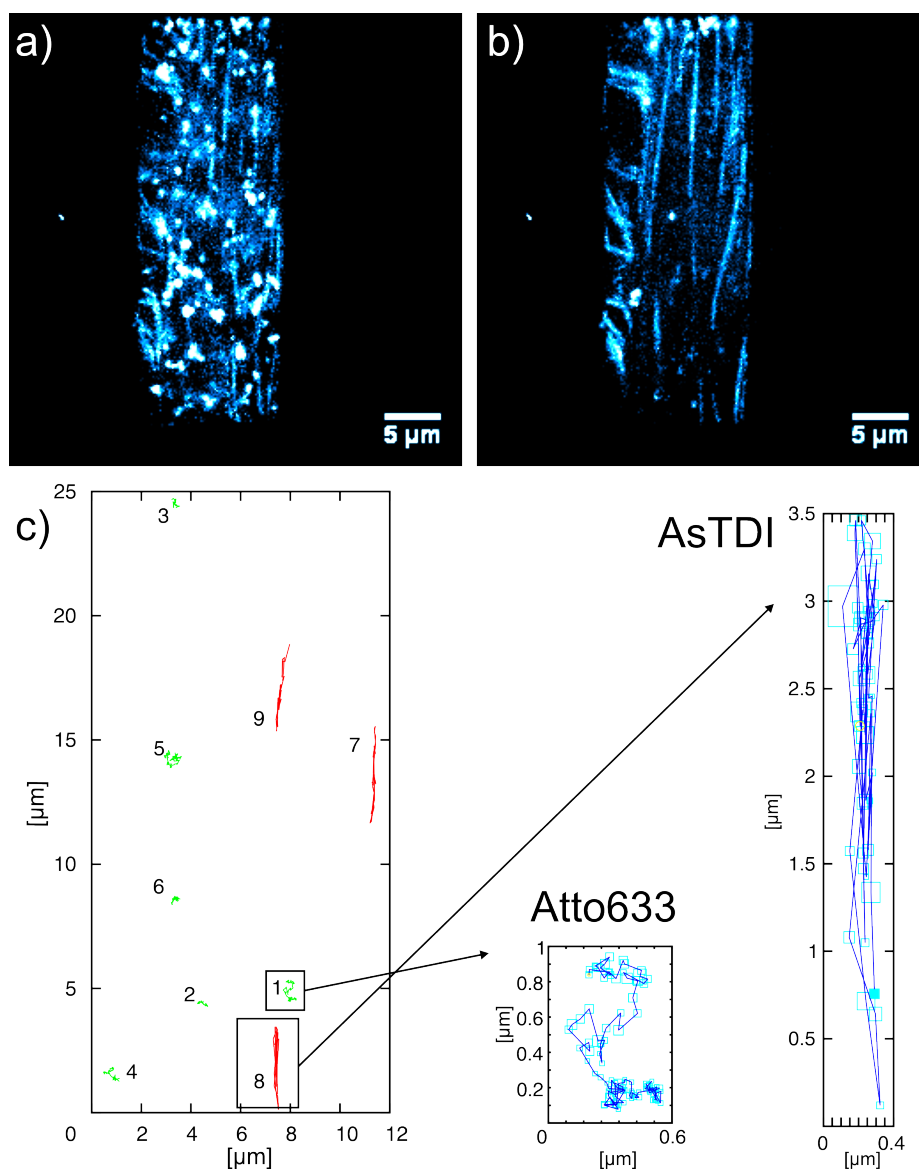
Figure 4.23: Maximum projection and trajectories of As-TDI and Atto633. (a) Maximum projection of the individual frames of a movie recorded with a fluorescence microscope at a frame rate of 2.5 fps, indicating the pathways of two different species of single molecules (Atto633 and As-TDI) in the mesoporous structure. (b) Maximum projection after photobleaching revealing only one species (As-TDI), which shows structured movement. (c) Direct comparison of exemplary trajectories of As-TDI (red) and Atto633 (green). As-TDI molecules show structured, aligned pathways while Atto633 molecules feature an unstructured, random movement.
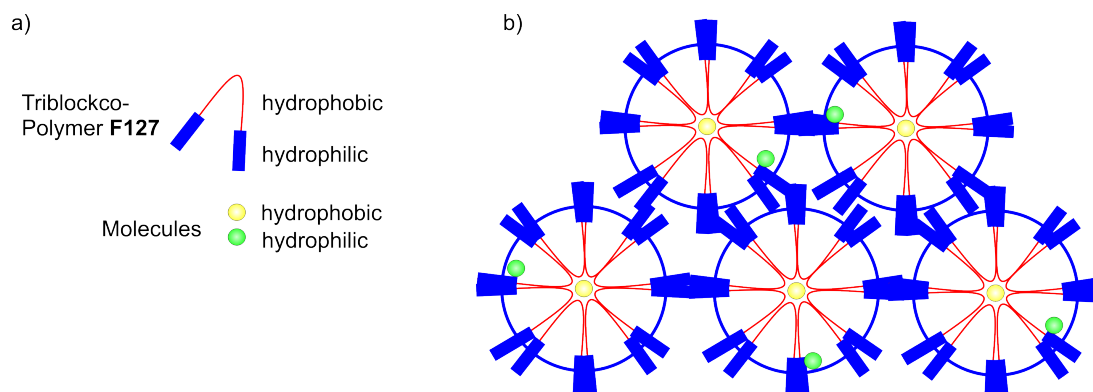
Figure 4.24: Model of the guest–host system.

4.3.5 Model of the Host–Guest System

In order to address the question why charged dye molecules presented a different pattern of movement than uncharged dyes, we tested various charged dyes (PhPy-PDI, Atto633, Atto532, Ws-TDI, Py-PDI) to rule out that the random movement inside the porous host was due to the chemical nature of the respective dye. However, all of the charged dyes that were investigated showed the same behavior in the material. We believe that this phenomenon can be explained by the following model of the host–guest system (see Figure 4.24). For the synthesis of the mesoporous silica channels we used the triblock-copolymer Pluronic F127 in an evaporation-induced self-assembly (EISA) approach. This template creates mesopores by forming cylindrical micelles in the polar solvent mixture with a diameter of about 9 nm, with the micelles featuring a hydrophobic interior and a hydrophilic exterior. The hydrophilic ends of the template protrude into the silica walls and can cause intrawall porosity [148–150]. The existence of such intrawall pores has already been described in the literature for Pluronic-templated mesoporous silica and has been studied by sorption measurements and electron microscopy of nanomolded platinum replicas [151–156]. In unextracted (i.e. template-filled) mesoporous silica films, we assume that these outer parts of the micellar template structure are preferred by hydrophilic, charged molecules whereas hydrophobic, uncharged molecules prefer the hydrophobic core of the micelles from where they cannot access the defects in the pore wall. This could be a possible explanation why uncharged molecules move in a structured way inside the channels, while charged molecules moving in close proximity to the pore wall can access defects and switch to other channels.

As a further proof of this model and in order to assure that the charged molecules are moving inside the pores of the mesoporous silica structure despite their rather random movement patterns, we prepared a sample containing only Atto633 in a single dye molecule concentration and applied an electric field diagonally to the aligned pores (movie M19 on the Supplementary CD). We could observe that the molecules which were located in the mesopores showed a directed movement along the mesoporous silica channels whereas molecules next to, but outside of the structure followed the electric field lines. The maximum projection of the individual frames of movie M19 is depicted

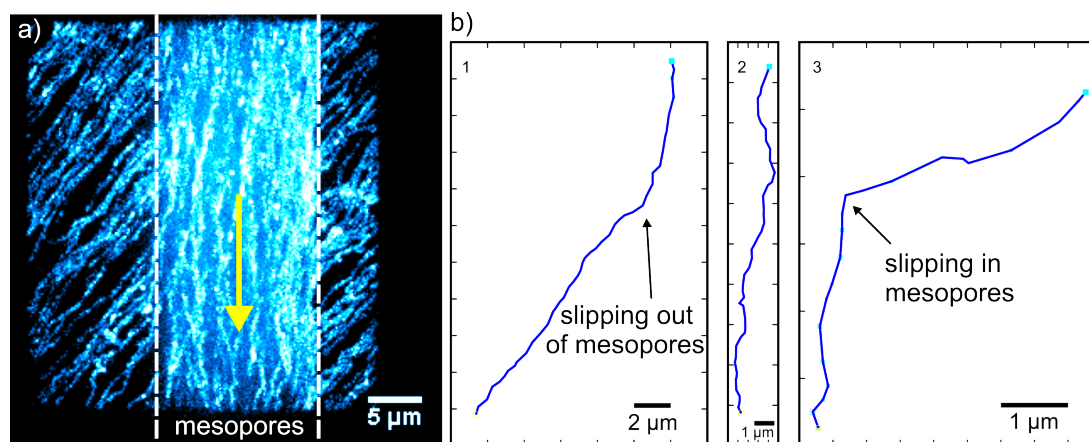**Figure 4.25:** Electrophoresis of Atto633 molecules in a diagonal electric field. (a) Maximum projection of the individual frames of a movie recorded with a fluorescence microscope revealing the pathway of Atto633 molecules influenced by a diagonal electric field. Molecules inside the mesoporous structure are guided by the aligned mesopore channels, whereas molecules next to the microgroove follow the electric field lines. The yellow arrow indicates the direction of movement of the molecules inside the mesopores. (b) Exemplary trajectories of Atto633.

in Figure 4.25a. We also observed molecules next to the silica structure changing their direction abruptly when slipping into the mesoporous structure (see exemplary trajectory 3 in Figure 4.25b) and also slipping out of it (see exemplary trajectory 1 in Figure 4.25b). This is possible because of numerous defects in the silica walls as explained above. Moreover, the experiment demonstrates that the molecules are guided by the mesoporous silica channels (see exemplary trajectory 2 in Figure 4.25b) aligned in y-direction. The trajectories of the charged dye molecules are again not as straight as in the case of uncharged dye molecules, as explained above in the guest–host model (Figure 4.24).

4.3.6 Average Velocity

We then investigated the influence of the electric field strength on the average velocity of single Atto633 dye molecules. For this purpose the electric field was applied along the channel direction. At the beginning, the electric field was adjusted to $1800\,\mathrm{V\,cm^{-1}}$ and then reduced stepwise to $100\,\mathrm{V\,cm^{-1}}$. The velocity of the molecules decreases with decreasing electric field strength and could therefore be directly influenced by the electric field acting as an external stimulus. Figure 4.26 present the maximum projection of the individual frames of movie M20 (see Supplementary CD) revealing the pathway of Atto633 molecules pulled along the silica channels. By averaging the positions (pixels converted to distance) *versus* time of at least five individual molecules for each electric field strength, the dependence of the average velocity on the electric field strength could be calculated (Figure 4.26b). The error bars depict the standard deviations of the averages. A linear trend can be seen for the increase of the average velocities with the electric field strength. From the slope we can calculate the mobility ($b = 5 \times 10^{-8}\,\mathrm{cm^2\,V^{-1}\,s^{-1}}$) of the Atto633 molecules in the
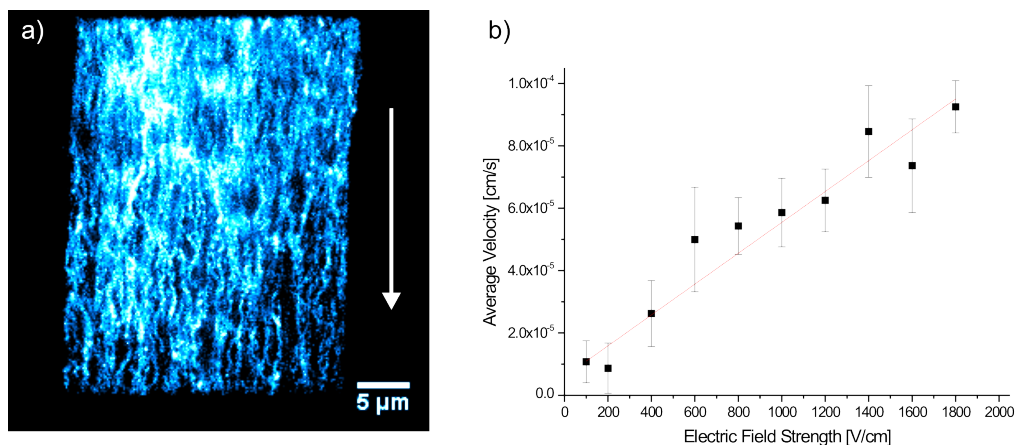
Figure 4.26: Maximum projection and average velocity. (a) Maximum projection of the individual frames of a movie recorded with a fluorescence microscope revealing the pathway of Atto633 molecules pulled along the silica channels by an electric field. The white arrow indicates the direction of movement of the molecules inside the mesopores. (b) Plot of the average velocity of Atto633 molecules versus electric field strength increasing from 100 to $1800\,\mathrm{V\,cm^{-1}}$. A linear fit ($y = a + bx$) with $a = 6 \times 10^{-6}\,\mathrm{cm\,s^{-1}}$ and $b = 5 \times 10^{-8}\,\mathrm{cm^2\,V^{-1}\,s^{-1}}$ is shown in red.

silica host.

4.3.7 Electrophoretic Separation of Ws-TDI and Py-PDI

To demonstrate the possibility of electrophoretic separation, we incorporated WS-TDI (negatively charged, molecular structure see Figure 4.27) and Py-PDI (positively charged, molecular structure see Figure 4.27) into the same sample. Again, we detect both fluorescence signals simultaneously in different channels. Channel 1 shows the fluorescence signal of Py-PDI molecules (see maximum projection in Figure 4.27a and movie M21 on the Supplementary CD) moving in the opposite direction as WS-TDI molecules in Channel 2 (see maximum projection in Figure 4.27b and movie M21 on the Supplementary CD). By switching the electric field on and off, the directed movement of the molecules could be controlled. Thus, we demonstrated the feasibility of separating differently charged molecules in a porous silica host.

$$\text{Py-PDI} \qquad\qquad \text{Ws-TDI}$$
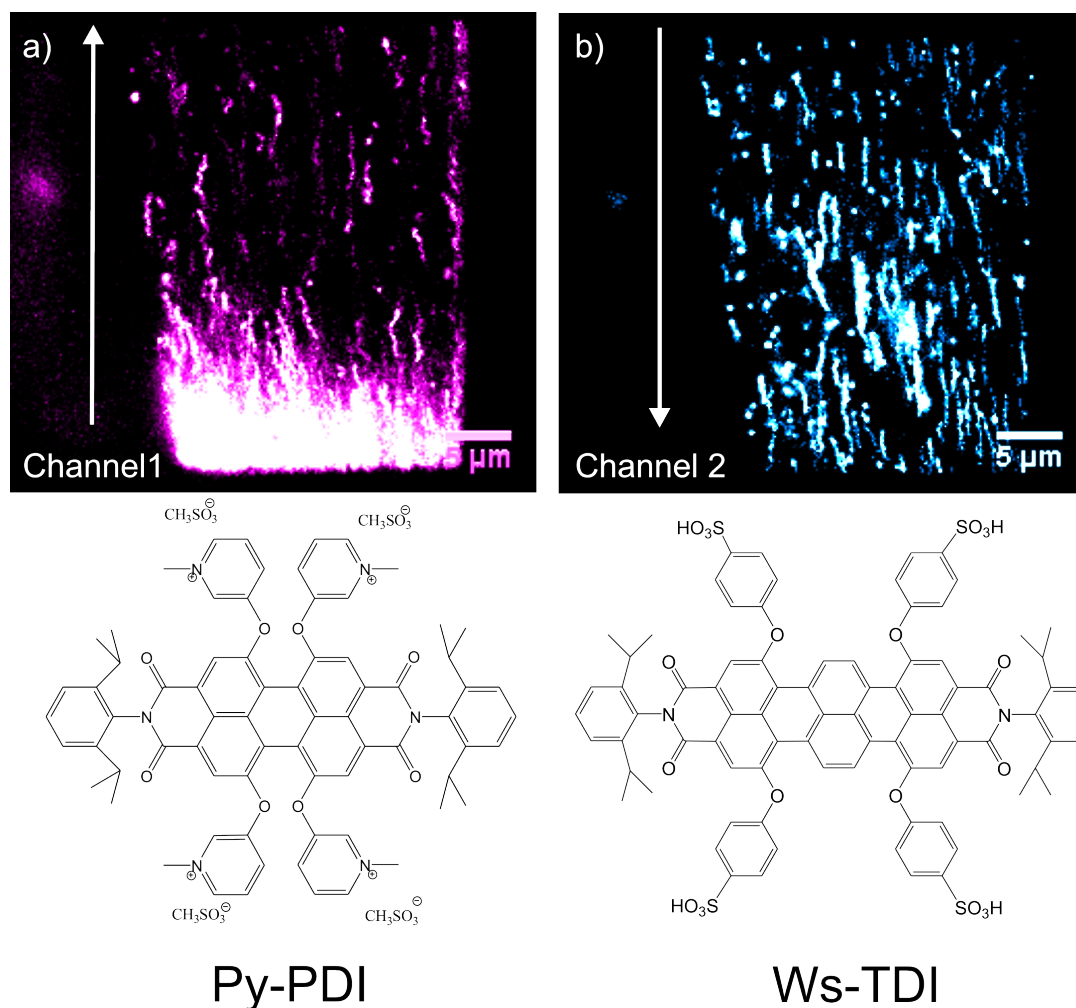
Figure 4.27: Separation of differently charged dyes. The maximum projections of the individual frames of a movie recorded with a fluorescence microscope at a frame rate of 2.5 fps reveals the pathways of (a) Py-PDI and (b) Ws-TDI molecules. The white arrows indicate the direction of movement of the molecules inside the mesopores under the influence of an electric field ($1000\,\text{V cm}^{-1}$).

4.3.8 Conclusion

In this study we have demonstrated the controlled movement of single molecules in highly oriented, template-filled mesoporous silica thin films under the influence of an electric field. Single-molecule trajectories directly reveal the mesoporous structure of the silica thin films with their defects and dead ends. By incorporating various uncharged dyes into the mesochannels we observed structured movement along the well-defined large-pore mesochannels in y-direction, while charged molecules took totally different, more random diffusional pathways and showed a greater propagation in x-direction. Based on these observations we presented a host–guest model which explains the different pathways of the molecules in such mesoporous materials.

Furthermore, the influence of the electric field strength on charged molecules was investigated. The

velocity of the charged molecules increased monotonically with increasing electric field strength, were the slope of the plot is the mobility of the guest molecule inside the host. By applying a diagonal electric field we could even observe molecules switching into the mesoporous structure, guided by the well aligned pores and also switching out of the mesoporous material through defects in the silica walls. Finally, we illustrate the controlled separation of differently charged molecules in the template-filled mesoporous silica thin films which can be directly observed with our single-molecule fluorescence wide-field microscope.

4.3.9 Experimental Part

Single-molecule fluorescence images were recorded with a wide-field setup, using an Eclipse TE200 (Nikon) epi-fluorescence microscope with a high numerical aperture (NA) oil-immersion objective (Nikon Plan Apo x100, NA = 1.40). The fluorescent uncharged dyes N-(2,6-diisopropylphenyl)-N'-octylterrylene-3,4:11,12-tetracarboxdiimide (called As-TDI in this work and ref. [139]), N,N'-bis(2,6-diisopropylphenyl)-terrylene-3,4:11,12-tetracarboxdiimide (called Dip-TDI in this work) and N,N'-bis(pentadecan-8-yl)-terrylene-3,4:11,12-tetracarboxdiimide (called Sw-TDI in this work) (for their chemical structures see Figure 4.20) with a high photostability and excellent quantum yield and the charged fluorescent dyes N-(trimethylammoniumpropyl)-N'-octylterrylene-3,4:11,12-tetracarboxdiimide (called Ammonium-TDI in this work), N,N'-bis(2,6-diisopropylphenyl)-1,6,7,12-tetra-(1-methyl-3-(4-phenoxy)-pyridinium)-perylene-3,4:9,10-tetracarboxdiimide tetraiodide (called PhPy-PDI in this work; chemical structure in Figure 4.19 and synthesized as described in ref. [157]), N,N'-bis(2,6-diisopropylphenyl)-1,6,7,12-tetra-(1-methylpyridinium-3-oxy)-perylene-3,4:9,10-tetracarboxdiimide tetramethanesulfonate (called Py-PDI in this work and synthesized as described in ref. [66]) and N,N'-bis(2,6-diisopropylphenyl)-1,6,9,14-tetra-(4-sulfonylphenoxy)-terrylene-3,4:11,12-tetracarboxdiimide (called Ws-TDI in this work and synthesized as described in ref. [49]) (chemical structures in Figure 4.19) were incorporated into the material in single-molecule concentrations ($10^{-10} - 10^{-11}$ M). The molecules were either excited at 633 nm with a He-Ne gas laser (Coherent, 75 mW maximum at 632.8 nm) with an intensity of 0.3 kW cm^{-2} or at 532 nm with a diode pumped solid-state laser (Cobolt Samba TM Laser) with an intensity of 0.05 kW cm^{-2}. Their fluorescence was detected with a back-illuminated electron multiplying charge-coupled device (EM-CCD) camera in frame transfer mode (Andor iXon DV897, 512x512 pixels). Incident laser light was blocked by a dichroic mirror (dual line beam splitter 532/633, AHF Analysentechnik) and by band-pass filters (675/250 and 560/40 for Channel 1 and 730/140 for Channel 2, AHF Analysentechnik). One pixel on the camera chip corresponds to 154 nm on the sample. The movement of the single molecules was detected in dependence of an electric field. In this study, electric field strengths up to 1800 V/cm were used. Single-molecule tracking was done by fitting the fluorescence spot by a 2D-Gaussian function:

$$f(x, y, A, w) = A e^{-\left(\frac{x-x_0}{w}\right)^2} e^{-\left(\frac{y-y_0}{w}\right)^2} ,$$

where A and w are the amplitude and the width of the Gaussian curve, to the point-spread function of the signals recorded with a back-illuminated EM-CCD camera. The method was described in

detail in previous studies [12, 140, 141]. The resulting positions can be combined frame by frame to form molecular trajectories.

The mesoporous silica thin films were prepared as described in our previous work [126]. Briefly, 700 µL of Milli-Q water and 100 µL of aqueous HCl (1 M) were diluted in 4.40 mL of absolute ethanol. Then, 1.00 mL of tetraethylorthosilicate (TEOS) were added and the solution was stirred (≈ 400 rpm) at 65 °C for 1 h. Simultaneously, a mixture of 475 mg of Pluronic F127 in 4.40 mL of Ethanol was stirred at room temperature for 1 h. Then, this solution was poured slowly into the ethanolic TEOS solution, and the resulting clear solution was stirred at room temperature for 2 h. Afterwards, the solution was used to infiltrate the voids of a PDMS-stamp that was brought into close contact with a plasma-treated standard glass cover slip and aged at room temperature for 21 h in a saturated ethanolic atmosphere and for $24 - 48$ h under ambient conditions.

Electrodes for applying the electric field were either obtained by depositing a thin silver film (typically 100 nm) with a gap of the desired width (typically $1 - 5$ mm) on the glass coverslips by a sputter-coating process using a shadow mask, or they were made by cutting the structure to the desired width after the ageing process (typically $1 - 5$ mm) with a razor blade and applying a conductive silver paste to both sides of the remaining structure forming two pads for connection to the high voltage generator.

4.4 Electrophoresis of DNA in Highly Oriented Mesoporous Silica Channels

The controlled movement of single dye molecules in highly oriented, template-filled mesoporous silica thin films under the influence of an electric field was successfully demonstrated in the previous section 4.3. As a further application of the aligned material, biomolecules such as DNA were incorporated on a single-molecule level into the pores and observed with a wide-field fluorescence microscope. The final aim of this project was, to separate different DNA molecules due to size differences.

4.4.1 Introduction

The development of nanostructure devices has opened the door to new DNA separation techniques. Loading bulky biomolecules into ordered nanostructures, such as the previously reported mesoporous silica structures [126], is very difficult but has great advantage compared to gels, in which the pores are disordered and the pore sizes are limited by the level of crosslinking. Besides the confined geometry, the tunable functionalization of the mesopores ensures a favorable interaction with DNA molecules in order to separate them due to their electrophoretic mobility μ. With this proportionality constant, the drift velocity v is proportional to the electric field E:

$$v = \mu E \qquad (4.4.1)$$

Furthermore, the diffusion coefficient D and the electrophoretic mobility μ are related through the Nernst-Einstein relation:

$$D = \frac{k_B T}{Q_{eff}} \mu \qquad (4.4.2)$$

with the Bolzmann's constant k_B and the temperature T. Q_{eff} defines an effective charge of the drifting molecule. This relation can be used to determine Q_{eff} from a known μ and D and to separate DNA strands of different lengths.

In the course of this thesis, several single-molecule experiments with different types of DNA strands (listed in Table 4.2), all labeled with Atto532 and Atto647N to show Förster Resonance Energy Transfer (FRET), were performed (Figure 4.28). Upon excitation of the ATTO532 dye, energy transfer will take place from the green ATTO532 (donor) to the red ATTO647N (acceptor) dye and fluorescence of the red dye can be monitored. Moreover, the intensity of the FRET signal depends strongly on the distance between both dyes, which must be in the range of $2-10$ nm. In the case of DNA denaturation no FRET signal is expected. The mesoporous silica thin films were prepared in cooperation with Bastian Rühle from the group of Prof. Thomas Bein as described in the Experimental section 4.4.5. After fixing the electrodes, the samples were loaded with DNA in a concentration suitable for single-molecule microscopy.
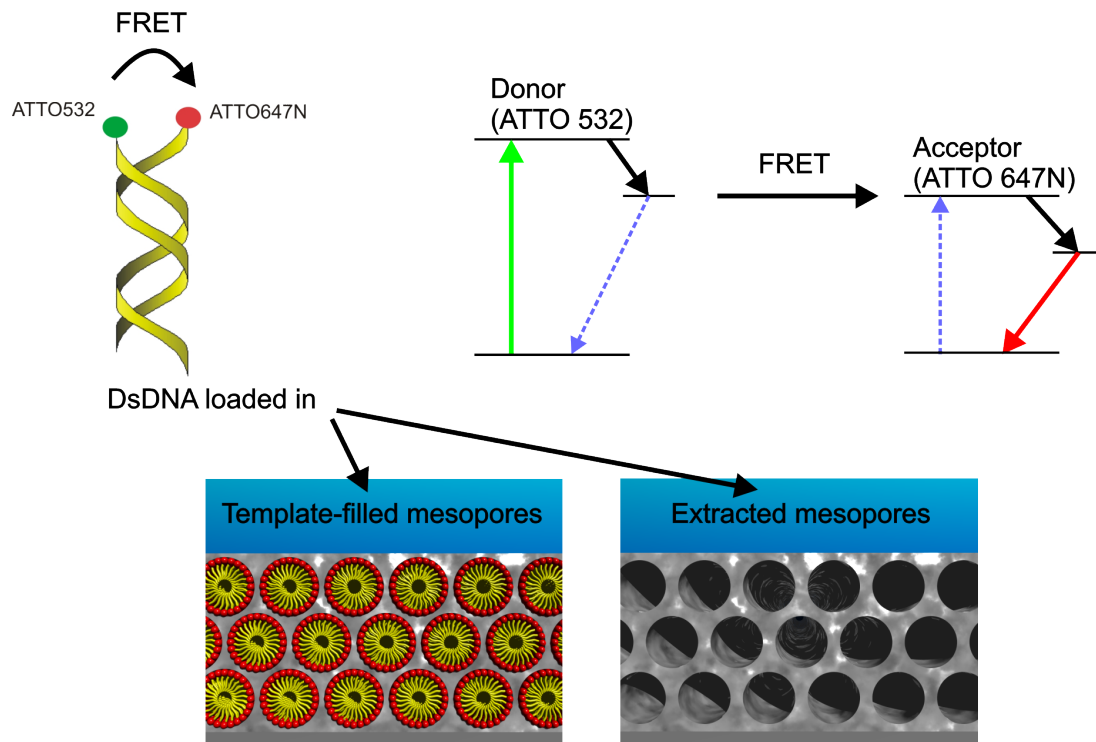
Figure 4.28: Fluorescence Resonance Engery transfer (FRET) experiments. DNA strands of different length are loaded in either template-filled or extracted highly oriented mesopores. Excitation of the donor (Atto532) with 532 nm light results not only in donor emission, but partially also in emission characteristic for the acceptor fluorophore (Atto647N), which is called FRET signal.

4.4.2 Strategy to Incorporate DNA into Template-Filled Mesopores

Figure 4.29 displays two maximum projections where 20 bp ssDNA labeled with Atto532 and Atto647N on a single strand was incorporated into template-filled mesopores. The samples were excited with 532 nm to induce FRET. After loading the DNA, many molecules could be detected in the green channel of Figure 4.29a, whereas in the red channel due to the bad signal-to-noise ratio and probably low FRET efficiency, less signal appeared. Additionally, one has to keep in mind the problem of crosstalk of both fluorophores. However, after photobleaching the acceptor molecules, some donor molecules appeared and could be detected in the green channel of Figure 4.29b. The maximum projection displays structured movement of two signals (highlighted with arrows), which can be probably assigned to DNA strands, or free Atto532 molecules. Due to the studies described in section 4.3, the latter case can be excluded, because Atto532 always showed unstructured movement in template-filled mesopores. Therefore, we assume the successful incorporation of the ssDNA, showing some structured movement of the ssDNA molecules in the green channel. To improve the signal-to-noise ratio and the FRET efficiency, different DNA strands and another loading strategy were pursued in the following section.
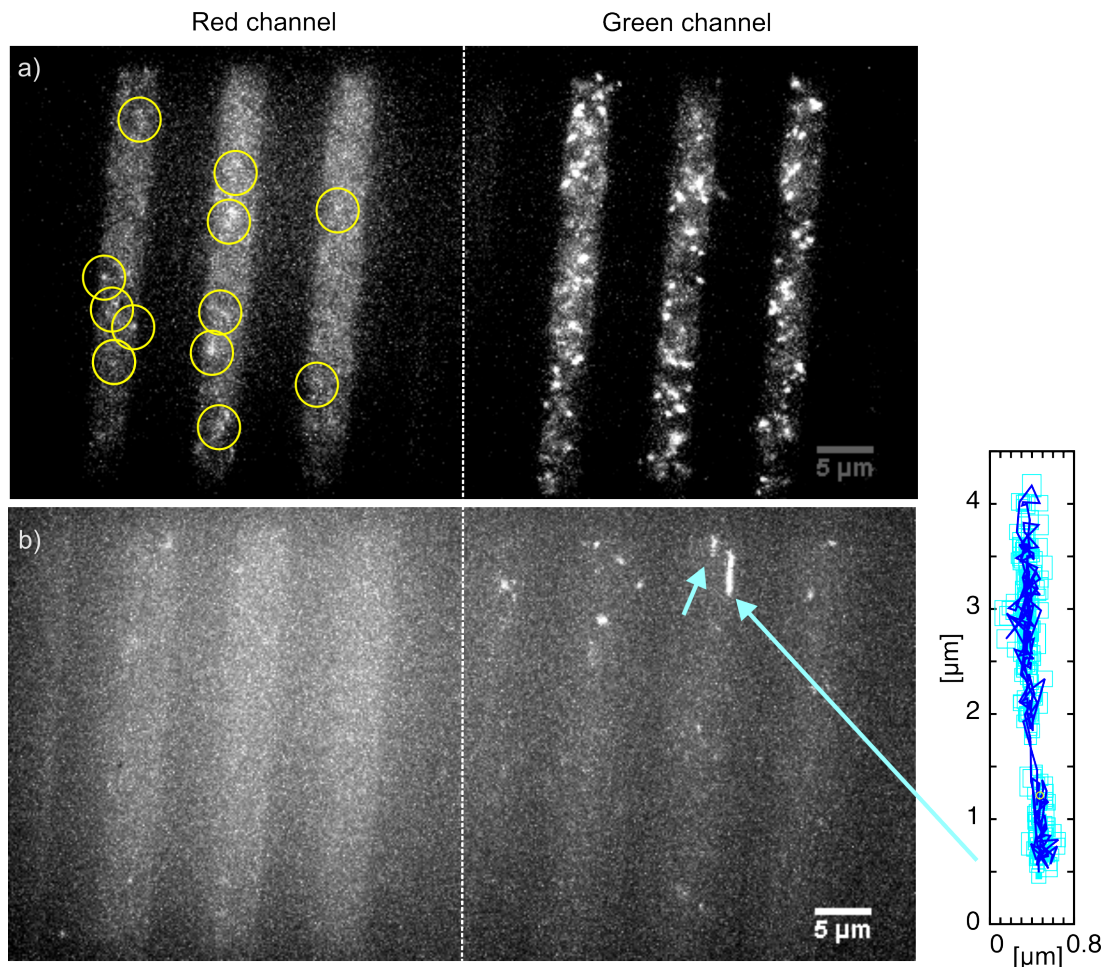
Figure 4.29: Single-molecule FRET experiments with 20bp ssDNA (DNA-sequence in table 4.2) labeled with Atto532 and Atto647N incorporated into template-filled mesopores. (a) The maximum projection of individual frames of a wide-field movie shows the FRET signals (circled yellow) in the red channel. Most of the DNA molecules remained immobile. (b) After photobleaching of the acceptor molecules, the maximum projection of the green channel clearly shows the structured pathways of two molecules (marked with blue arrows; The corresponding movie M22 can be found on the Supplementary CD) whereas the other molecules mainly stayed immobile.

4.4.3 Strategy to Incorporate DNA into Extracted Mesopores

Another strategy was to remove the template before the samples were loaded with labeled dsDNA. In our system the empty pores have a diameter of about 9 nm. Previous studies (section 4.2.3) showed the connections between adjacent channels and the defects in the silica walls. Therefore, biomolecules such as dsDNA should be able to enter the structure through such defects and diffuse into the pores upon immersion of the samples in a solution of biomolecules.

20bp dsDNA molecules labeled with Atto532 and Atto647N (see basepair sequence in Table 4.2) were loaded into extracted mesopores and excited with 532 nm light. The focus was varied during
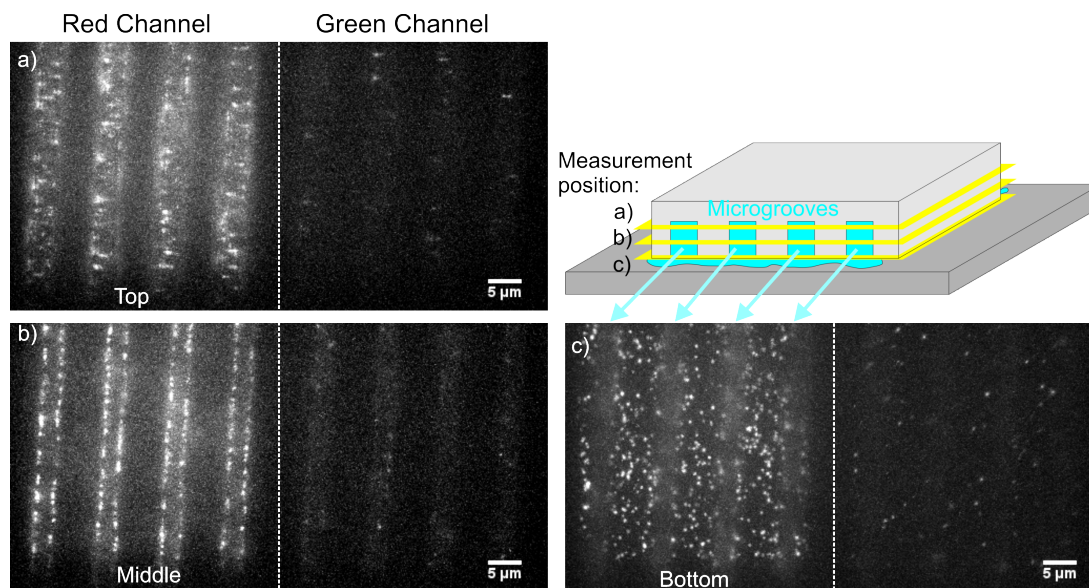
Figure 4.30: Single-molecule FRET experiment, where dsDNA strands, labeled with Atto532 and Atto647N, were loaded to extracted mesopores. The maximum projections of individual frames of a wide-field movie (movie M23 on the Supplementary CD) depict four microgrooves and show the FRET signals in the red channel of 20bp dsDNA moleculesat different measurement positions of the microgrooves. (a) shows molecules which are focused at the bottom of the sample near the coverslip, (b) depicts the middle of the microgrooves and (c) displays molecules at the top region of the microgrooves.

the measurement to observe the DNA molecules over the entire height of the microgrooves. Figure 4.30 displays three maximum projections of individual frames of a movie taken with a wide-field microscope at different measurement positions a,b and c. The emission of Atto647N molecules of intact dsDNA molecules caused by FRET is visible in the red channel. The molecules diffuse more random and most of them seem to adsorb on the surface of the microgrooves. This can be seen in the red channel of Figure 4.30b, where most of the molecules occur at the side of the microgrooves. In order to favor the diffusion within the channels, a particular functionality of the pores is highly desirable. Initial experiments with Cyano- (CN) and Amino- (NH_2) functionality similar to a previous publication [131] showed a too high background fluorescence to observe the FRET signal of single molecules. These impurities could be removed after several washing steps, but the structure of most of the channels was destroyed by this procedure. It is therefore important to find an ideal functionalization strategy which preserves the structure of the highly oriented channels and enhances the affinity between the host and the guest molecules.

4.4.4 Conclusion

Initial experiments performed with template-filled mesopores have demonstrated the successful incorporation of DNA, showing some structured movement which could be associated to 20bp ssDNA molecules. However, to support this, more experiments with labeled DNA strands, showing higher FRET efficiency, have to be done. The experiments with Atto532 and Atto647N labeled dsDNA

Table 4.2: Sequences of the investigated DNA strands.

DNA	Sequence
20 bp ssDNA	**ATTO532** GAC ATC ATC GCG GCT ATA GC **ATTO647N**
20 bp dsDNA	5' GGA CGC CAG GGG GAA GCG AC **ATTO647N** 3' 3' CCT GCG GTC CCC CTT CGC TG **ATTO532** 5'
30 bp dsDNA	5' GGA CGC CAG GGG GAA GCG ACG GAC GCC AGG **ATTO532** 3' 3' CCT GCG GTC CCC CTT CGC TGC CTG CGG TCC **ATTO647N** 5'
60 bp dsDNA	5' GGA CGC CAG GGG GAA GCG ACG GAC GCC AGG CTG ATT TGA AGC TTA TGA CTT ATT GGA CCT **ATTO532** 3' 3' CCT GCG GTC CCC CTT CGC CTC CTG CGG TCC GAC TAA ACT TCG AAT ACT GAA TAA CCT GGA **ATTO647N** 5'
90 bp dsDNA	5' GGA CGC CAG GGG GAA GCG ACG GAC GCC AGG CTG ATT TGA AGC TTA TGA CTT ATT GGA CCT ATC TCT GAC ATA TTA TAC TAG GCT GTG TTT **ATTO532** 3' 3' CCT GCG GTC CCC CTT CGC TGC CTG CGG TCC GAC TAA ACT TCG AAT ACT GAA TAA CCT GGA TAG AGA CTG TAT AAT ATG ATC CGA CAC AAA **ATTO647N** 5'

molecules which were incorporated into extracted pores showed good FRET signals, however the molecules adsorbed mainly at the surface of the microgrooves. Therefore, a functionalization strategy which enhances the affinity between the host and the guest molecules and preserves the structure of the highly oriented silica channels has to be developed.

4.4.5 Experimental Part

Single-molecule fluorescence images were recorded with a wide-field setup, using an Eclipse TE200 (Nikon) epi-fluorescence microscope with a high numerical aperture (NA) oil-immersion objective (Nikon Plan Apo x100, NA = 1.40). Table 4.2 depicts all used DNA strand sequences.

They were incorporated into the material in single-molecule concentrations ($10^{-10} - 10^{-11}$ M).

The biomolecules were excited at 532 nm with a diode pumped solid-state laser (Cobolt Samba TM Laser) with an intensity of 0.05 kW cm^{-2}. Their fluorescence was detected with a back-illuminated electron multiplying charge-coupled device (EM-CCD) camera in frame transfer mode (Andor iXon DV897, 512x512 pixels). Incident laser light was blocked by a dichroic mirror (dual line beam splitter 532/633, AHF Analysentechnik) and by band-pass filters (675/250 and 560/40 for Channel 1 and 730/140 for Channel 2, AHF Analysentechnik). More details about the setup is described in section 2.2.1.

The mesoporous silica thin films were prepared as described in our previous work [126] and in the section above. Electrodes for applying the electric field were made by cutting the structure to the desired width after the ageing process (typically $1 - 5$ mm) with a razor blade and applying a conductive silver paste to both sides of the remaining structure forming two pads for connection to the high voltage generator.

5 Optical and Structural Properties of Silver Nanowires

This chapter is based on the article "Synchronous Emission from Nanometric Silver Particles through Plasmonic Coupling on Silver Nanowires" by Melari Davies*, Angela Wochnik*, Florian Feil*, Dr. Christophe Jung, Prof. Dr. Christoph Bräuchle, Prof. Dr. Christina Scheu, and Prof. Dr. Jens Michaelis, published in *ACS Nano*, 6(7):6049-6057, 2012.
*These authors contributed equally to this work.
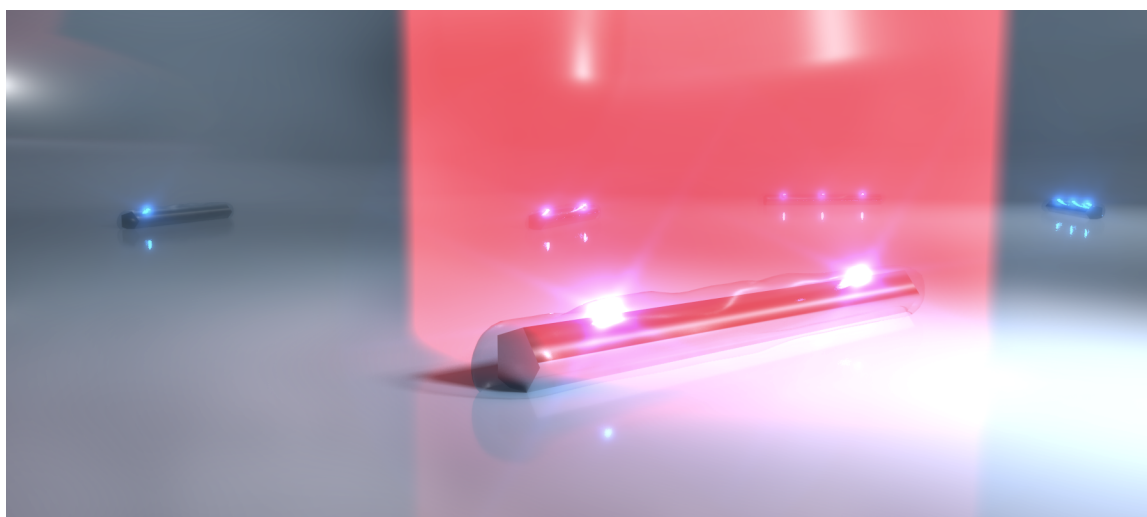
5.1 Introduction: Plasmonics in Metals

When light interacts with a metal surface (Figure 5.1), it excites electrons, which can form propagating excitation waves called surface plasmon polaritons or surface plasmon resonanz (SPR) [158]. Analogue to water waves, these electromagnetic waves can propagate in a direction parallel to the metal interface or be located strongly on the metall surface (then called localized SPRs (LSPRs)). Moreover, these oscillations are very sensitive to any change (e.g. a local particle, defect or a rough surface) on the boundary of the metal and the external medium. When the surface plasmon wave interacts for example with a particle, parts of the energy can be re-emitted as light. Due to this there has been a growing interest in the synthesis and control of nanostructures of (noble) metal assemblies.

Figure 5.1: Light excitation of a (a) Ag-particle and (b) Ag-Nanowire causes propagating excitation waves on the surface of Ag, called surface plasmons.
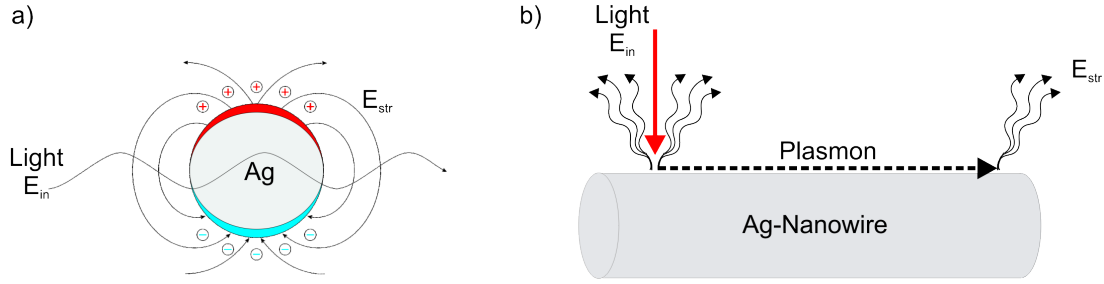
Their unique optical properties caused by the collective oscillation of free electrons, are a central subject of recent research [158–160]. In particular, silver is known for exhibiting plasmon resonances for particle sizes in the nanometer regime. Also the shape of the metal, such as the aspect ratio of silver nanowires, has a tremendous influence on the plasmonic properties [161]. Consequently, a thorough understanding of these properties is essential for the development of customized plasmonic systems for nanotechnology applications. Such potential utilizations include surface-enhanced Raman scattering (SERS) [162–165], plasmon wave-guiding [166–170], gas or biomolecular sensors [171, 172], and coupling to luminescent particles, such as dye molecules [173–175], quantum dots [176, 177], or metal nanoparticles [178]. Despite the extensive efforts put into the investigation of synthesis conditions of metal nanoparticles, such as silver nanowires (Ag-NWs) and their plasmonic properties for spectroscopic enhancement, only few studies on their luminescence after photoactivation exist as high detection sensitivity is required [179–181].

Uniform silver nanowires are usually synthesized by templating methods using either hard templates, such as porous alumina [182], or soft templates, including cetyltrimethylammonium bromide (CTAB) [183], polyvinylpyrrolidone (PVP) [184, 185], or trisodium citrate [186]. It is known that small defects in the nanowire as well as the presence of silver nanoparticles in the close vicinity of the nanowire can have tremendous influence on their emission properties. One important example is the photochemical formation of a silver nanocluster in such defects, which form local emitting entities. The formation of such entities has recently been described [187–190]. First, pure silver is oxidized, followed by the generation of small silver clusters within the silver oxide layer caused by irradiation with a laser beam. Important insight into the emission characteristics of metal nanoparticles can be obtained by single-molecule spectroscopy (SMS) experiments, where a single particle or molecule is observed continuously over a long time interval providing a direct view on the heterogeneity of molecular behavior [191–194]. With SMS subpopulations, rare events and the influence of structural heterogeneous environment on the different single particles can be revealed. However, detailed structural analysis of the nanowires and nanoclusters is hindered due to the limited spatial resolution.

In the following section silver nanowires are investigated using a combination of SMS and transmission electron microscopy (TEM) including analytical techniques. With this, a further field of

application of single-molecule microscopy is presented. Using wide-field illumination, we observed synchronous fluorescence emission from emitters located at distinct positions along single nanowires. By correlating fluorescence, high-resolution TEM (HRTEM), and energy-dispersive X-ray spectroscopy, we were able to attribute the cooperative behavior to spectroscopic features of the silver nanowires.

5.2 Synchronous Emission on Silver Nanowires

We investigated silver nanowires using correlative wide-field fluorescence and transmission electron microscopy (TEM). In the wide-field fluorescence images, synchronous emission from different distinct positions along the silver nanowires was observed. The sites of emission were separated spatially by up to several micrometers. Nanowires emitting in such cooperative manner were then also investigated with a transmission electron microscope. Therefore, general remarks about electron microscopy and especially TEM is presented in the following section before the detailed description of the TEM studies follow.

5.2.1 Transmission Electron Microscopy (TEM) Studies

Electron microscopy operates with the same basic principles as a light microscope but uses electrons instead of light. Electrons have wavelengths about 100.000 times shorter compared to visible light photons, and therefore the resolution of an electron microscope (theoretical resolution of about 0.1 Å) is much better than with a diffraction limited non-confocal light microscope (resolution about 300 nm). It is therefore a useful technique to reveal the nanostructure of materials. However, spherical and chromatic aberrations as well as astigmatism of the lens limit the resolution of conventional electron microscopes. With aberration correctors atomic resolution is possible in practice. With a transmission electron microscope (TEM) structures which are much smaller than the wavelength of visible light, like the pores of highly oriented silica material in Chapter 4 or silver nanowires presented in this chapter, can be investigated. The electrons are emitted from a tungsten filament or a LaB_6-crystal and accelerated by a high voltage. The electron beam is focused onto an ultra-thin specimen by electromagnetic fields and generates several signals, such as Auger electrons, secondary electrons, backscattered electrons and x-rays which are all summarized in Figure 5.2a.

In Figure 5.2b the schematic representation of the electron beam through a TEM is depicted. To decrease and control the diameter of the electron beam, it passes the condenser lens which focuses the beam onto the specimen. Subsequently, the objective lens is needed to form the first intermediate image in the back focal plane. The intermediate and projector lenses then enlarge the image which also can be the diffraction pattern (depending on the strength of the intermediate lens). Finally, the image or the diffraction pattern is projected on a fluorescent screen or a CCD camera. Different TEM-based techniques, such as bright-field (BF) imaging, high-resolution (HRTEM), and energy-dispersive X-ray (EDX) spectroscopy were used to investigate silver nanowires and are therefore briefly introduced here:

Bright-field (BF) images are produced if the objective aperture is centered around the optical axis
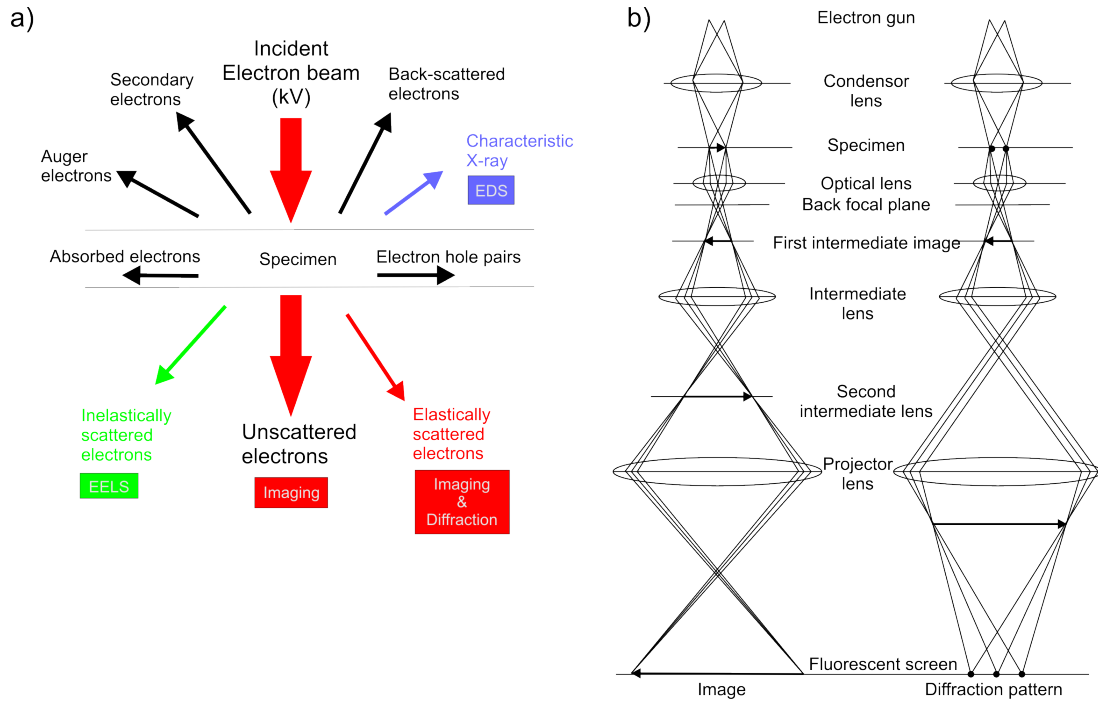
Figure 5.2: (a) Different kind of interaction between the incident electron beam and the specimen. (b) Schematic representation of the beam path through a transmission electron microscope. Figure adapted from Reference [195].

and which gives a bright background in the absence of the specimen.

High-resolution TEM (HRTEM) allows to illustrate the periodicity of the crystallographic structure of a specimen with atomic resolution and is therefore used to characterize nanostructures in crystalline materials such as silver nanowires.

With energy dispersive X-ray spectroscopy (EDX), elemental analysis and chemical characterization of the nanowires are demonstrated.

The bright-field image of an exemplary silver nanowire (Ag-NW) in Figure 5.3a shows an 11 µm long and 80 nm thick Ag-NW deposited on a holey carbon-coated copper grid. The single crystalline silver nanowires were synthesized by a seedless wet-chemical approach (see Section 5.2.5). As can be seen, the nanowire has a rather homogeneous thickness over the entire length.

Higher magnification images and diffraction studies revealed more detailed information of the Ag-NWs structure. Figure 5.3b shows a higher magnification bright-field image of a selected region of this Ag-NW (indicated by the red square in Figure 5.3a). A $10-20$ nm thick layer surrounding the Ag-NW can be observed, which is attributed to the sodium citrate used for the growth and stabilization of the Ag-NWs during their synthesis (see Section 5.2.5). Additionally, particles of about $5-10$ nm in size can be seen in this citrate layer. The electron diffraction pattern (Figure 5.3b inset) taken in the middle of the Ag-NW from Figure 5.3b displays spots corresponding to Ag reflections.
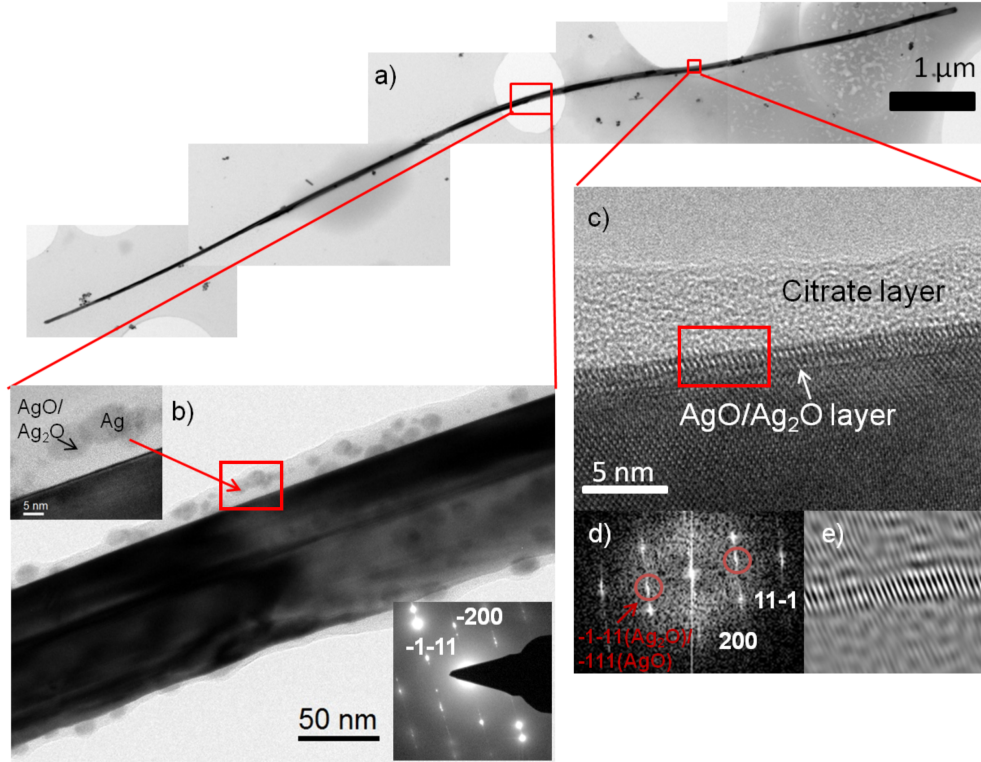
Figure 5.3: (a) Bright-field TEM image of an exemplary silver nanowire with dimensions of about $11\,\mu m$ length and $80\,nm$ thickness. The red squares indicate specific areas that were then imaged at higher magnifications. (b) Higher magnified TEM image of a selected area showing a $10-20\,nm$ thick layer surrounding the Ag-NW, which was attributed to citrate. The inset in the top left shows the Ag-NW surface at even higher magnification. In the citrate layer, particles of about $5-10\,nm$ can be observed, which are attributed to AgO, Ag_2O, or Ag. The recorded electron diffraction pattern of the Ag-NW indicates the presence of pure Ag (second inset). (c) High-resolution image of a specific region from (a) showing the citrate layer surrounding the Ag-NW and an additionally 2–3 thick layer on the interface between the NW and citrate layer. (d) Fast Fourier transformation of the marked area (red) in (c) shows an (011) orientation of the nanowire and indicates reflections corresponding to the d values of Ag. One additional set of reflections (red) was found, which matches the (-1-11) plane of Ag_2O or (-111) of AgO. (e) Inverse fast Fourier transformation (FFT) of this additional set of reflections (red in (d)) indicates that it can be assigned to the surface layer.

In addition, reflections due to twinning that is, two or more separate crystals sharing some of the same crystal lattice points in a symmetrical manner, of the Ag-NW occur in accordance with the observations reported in the literature where five-fold twinning is frequently observed for Ag-NWs and nanoparticles [196, 197]. Moreover, diffraction experiments and fast Fourier transformation (FFT) analysis of high-resolution TEM (HRTEM) micrograph analysis taken at various positions along the surface of the Ag-NW and of particles in the citrate layer showed additional weaker reflections attributed to silver oxide. Hence, the particles in the citrate layers are primarily pure Ag particles,

and only some of them are composed of silver oxide. When imaged at a higher magnification, an additional 1 nm thick layer is observed at the interface between the NW and citrate layer, consisting of 2–3 atomic layers (Figure 5.3c). The FFT of the marked area (red) from Figure 5.3c indicates reflections corresponding to the d values of Ag and shows the same orientation as the nanowire in (011) (Figure 5.3d). Furthermore, one additional set of reflections was found (marked red in Figure 5.3d), which corresponds either to the (-1-11) plane of Ag_2O or to the (-111) of AgO. By comparing the inverse FFT of these reflections to the original image, it becomes clear that these reflections stem from the surface layer (Figure 5.3e). Thus, the Ag-NWs possess a thin silver oxide layer, in accordance with data from additional diffraction experiments and FFT analysis (data not shown).

5.2.2 Wide-Field Fluorescence Studies

In order to unravel the optical properties of the Ag-NWs, the luminescence of individual NWs was investigated using a wide-field optical microscope with single-molecule fluorescence sensitivity (see Section 5.2.5). Typically each NW had several localized spots from where luminescence emission occurred. Single particle tracking (SPT) was used to determine the positions of these emitting entities on the silver nanowires by fitting, frame-by-frame, a two-dimensional Gaussian function according to

$$I = A_0 e^{\frac{-(x-x_0)^2}{2\sigma^2}} e^{\frac{-(y-y_0)^2}{2\sigma^2}} \tag{5.2.1}$$

where A_0 and σ^2 are the amplitude and the variance of the two-dimensional Gaussian curve, respectively, and x_0 and y_0 are the coordinates of the position of the individual emitting entities. With this method, the positions of the entities can be determined with a positioning accuracy of up to 5 nm (on glass substrates) depending on the signal-to-noise ratio. Changes in the brightness of the emitting entities, background fluorescence, or other emitters nearby can decrease the signal-to-noise ratio and thereby the positioning accuracy. For experiments requiring an overlay of TEM and fluorescence images, a Si_3N_4 membrane was used as a substrate (see Section 5.2.5). This resulted in a reduced signal-to-noise ratio and thus a lower positioning accuracy (typically about $20-25$ nm) as compared to experiments on glass substrates, which were only used for fluorescence measurements. The fluorescence from the spots was not continuous, but blinking and changes in fluorescence intensity was observed (Figure 5.4). This effect has been reported previously using confocal microscopy [180] and was attributed to random surface diffusion and agglomeration of Ag atoms which form photoactive Ag nanoclusters [198] or photoactivated silver oxide [179]. Interestingly, using the wide-field excitation, we find that oftentimes the emission from several spots on a single NW is highly cooperative; that is, blinking and intensity fluctuations are observed exactly at the same time, given our time resolution of 10 ms. Blinking of both cooperatively emitting sites, as well as that of single emitters, follows a power law (see Figure 5.5).

As an example of the cooperative effect, Figure 5.4 displays three consecutive frames extracted from a sequence of images (movie N1 on the Supplementary CD) showing the synchronous appear-
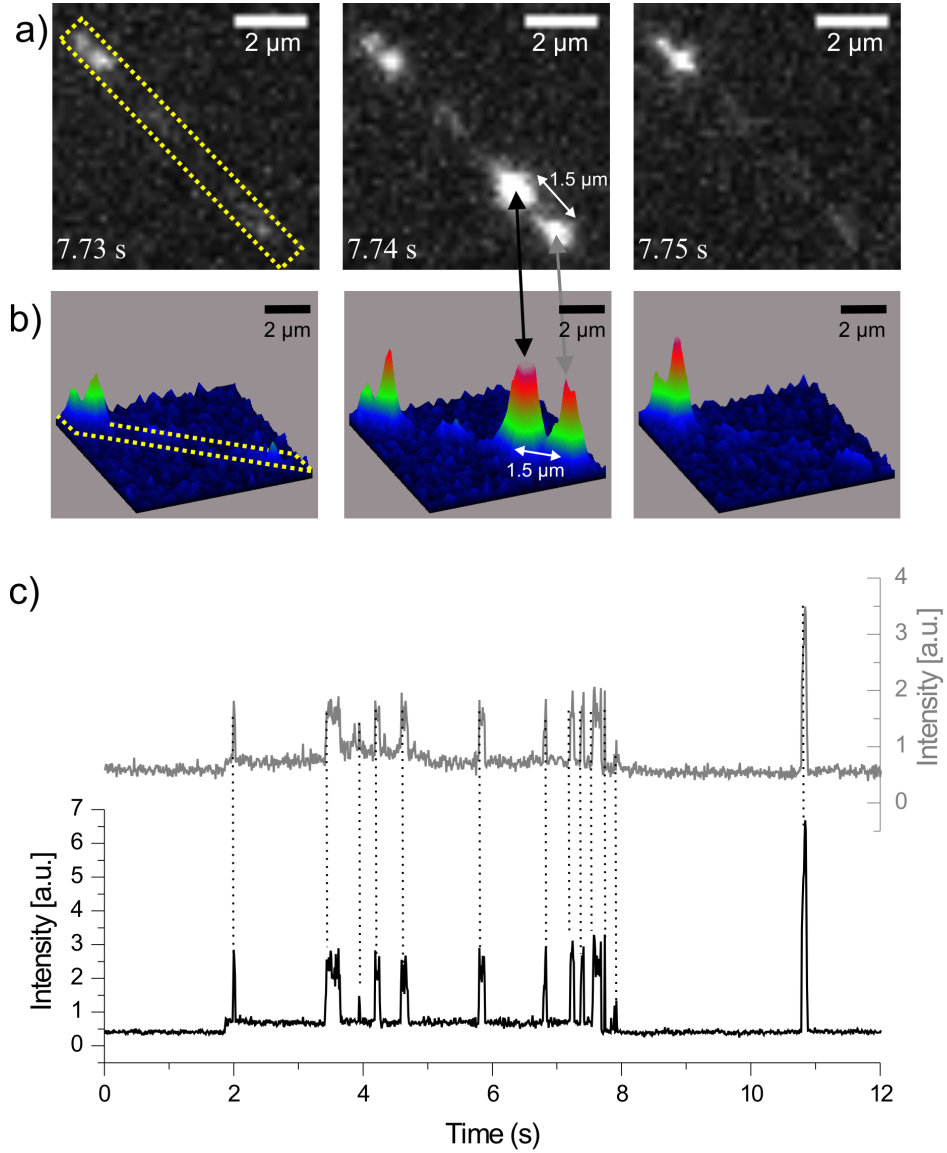
Figure 5.4: Wide-field fluorescence study of a Ag-NW. (a) Series of wide-field images of emitting entities exhibiting a cooperative fluorescence emission. The positions of the emitters are marked with a black and gray arrow in the middle panel. (b) Corresponding 3D surface plots of the fluorescence intensity. (c) Fluorescence intensity trajectories over time for both emitters (gray and black lines matching the color of the respective arrows in (a)). Exemplary synchronous emission events are highlighted by dashed lines.

ance and disappearance of two spatially separated fluorescence spots along a single Ag-NW (the approximate shape of the nanowire as observed using bright-field microscopy (data not shown) is indicated by the yellow striped line). The fluorescence patterns of the spots were fitted with two-dimensional Gaussian functions (Equation 5.2.1). The two centers of emission (marked by arrows

a)

b)
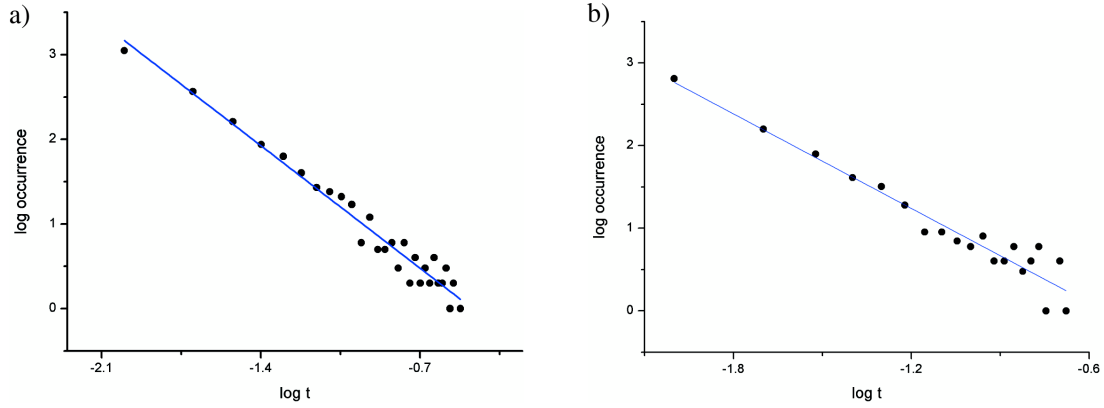
Figure 5.5: Power law analysis of on-times of an exemplary synchronous emitter pair (a) and a single emitter (b). Statistical analysis of 50 coupled emitters and 50 single emitters yielded an exponent of $m_{coupled} = 2.07 \pm 0.01$ and $m_{non-coupled} = 1.91 \pm 0.12$, respectively.
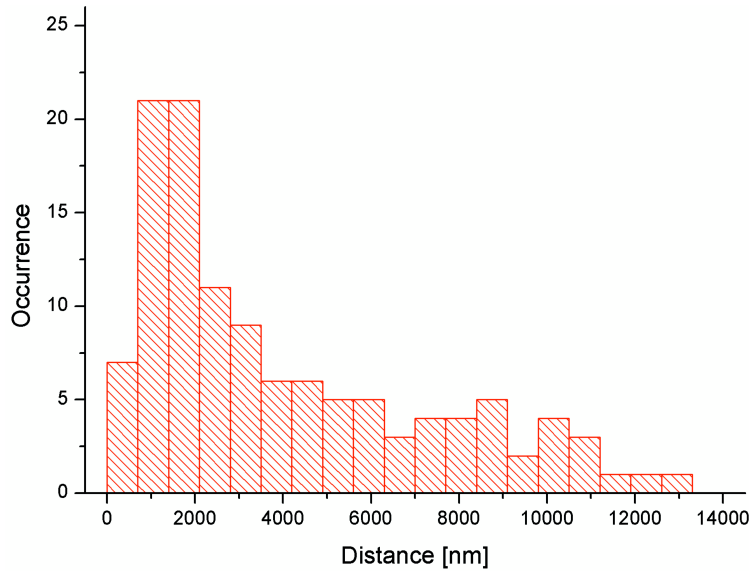
Figure 5.6: Histogram of the determined distances between pairs of coupled emitters. The distribution of these distances is continuous and decays with longer distances, i.e. the probability of finding a pair of coupled emitters is higher for smaller distances. However, due to diffraction of light emitter pairs separated by less than 300 nm cannot be detected and are counted as a single emitter, which is why the first bar of the histogram between is lower than the second.

in Figure 5.4a,b) were separated by a distance of about $1.5\,\mu m$. The recorded trajectories of the fluorescence intensity of both emitters show repetitive correlated blinking events (Figure 5.4c). The time at which emission occurs appears to be stochastic, but the fluorescence emission from both emitters is perfectly synchronized (as indicated by the gray dotted lines). Additionally, a statistical analysis of 120 distances between pairs of synchronous emitters was performed. The distribution of these distances (Figure 5.6) is continuous and decays with longer distances. This observation can

Table 5.1: Pearson correlation for the example of the 8 cooperative emitters from Figure 5.7 for all 5000 frames corresponding to 50 s.

Emitter No.	1	2	3	4	5	6	7	8
1	1	0,97689	0,97117	0,74928	0,82624	0,77227	0,83471	0,87434
2	0,97689	1	0,95427	0,74037	0,81003	0,75332	0,8141	0,8435
3	0,97177	0,95427	1	0,75832	0,82117	0,75837	0,81642	0,8435
4	0,74928	0,74037	0,75832	1	0,75168	0,65169	0,68053	0,69499
5	0,82624	0,810003	0,82117	0,75168	1	0,78592	0,80646	0,0,8074
6	0,77227	0,75332	0,75837	0,65169	0,78592	1	0,93935	0,86399
7	0,8,471	0,8141	0,81642	0,68053	0,80646	0,93935	1	0,93435
8	0,87434	0,84074	0,8435	0,69499	0,8074	0,86399	0,93435	1

be explained by the exponential decay of the intensity of surface plasmons along metal surfaces. This plasmon damping is caused by power loss in the metal. Moreover, while the exemplary trace from Figure 5.4 shows rather long on-times, oftentimes observed on-times were below our time resolution of 10 ms; that is, we observed only a single "on-frame". In our experiments, we investigated more than 200 nanowires and detected cooperative emission for about 35 % of the nanowires, and about 2 % of the NWs exhibited no emission at all while the remaining NWs showed noncoupled blinking of single emission sites. Interestingly, cooperative emission was observed only after an aging time under air atmosphere of at least one day (after growth); we never observed cooperative emission from freshly prepared nanowires. Also, the total number of emitters increased with aging. This indicates that the formation of silver clusters from silver oxide layers is a prerequisite for the occurrence of the observed cooperative emission. Furthermore, emitters on different NWs were never observed to emit simultaneously even when they were at distances smaller than the largest distances (approximately 10 μm) for which the cooperative effect was observed (data not shown). Thus, the coupling of the emitters observed through the cooperative emission occurs via the Ag-NW most likely through surface plasmons.

The question then arises whether the two (or more) cooperative emissive sites are all active or whether some of them behave in a passive fashion (i.e. as scatterers). In the case of one active center, the laser beam would excite one entity which could emit itself but also couple energy to the surface plasmon of the nanowire. This energy could then be transmitted to a passive center (such as a defect site or a nanoparticle), located on the same wire, but separated by some distance. In this case, the emitted fluorescence intensity of all emissive sites should be perfectly correlated. In contrast, we observed for NWs showing more than two coupled emitters, such as the example in Figure 5.7a (movie N2 on the Supplementary CD), that while the emission off all emission sites is highly cooperative at times (Figure 5.7b), there are also emission bursts from only subsets of the emitters (Figure 5.7c). Therefore, it is highly likely that these emitters are active centers rather than passive scatterers.

In order to provide direct evidence that cooperative emitters are active and not passive scattering centers, we performed additional experiments in which we temporarily blocked the excitation of single emitters by inserting a physical mask in the excitation pathway, while at the same time
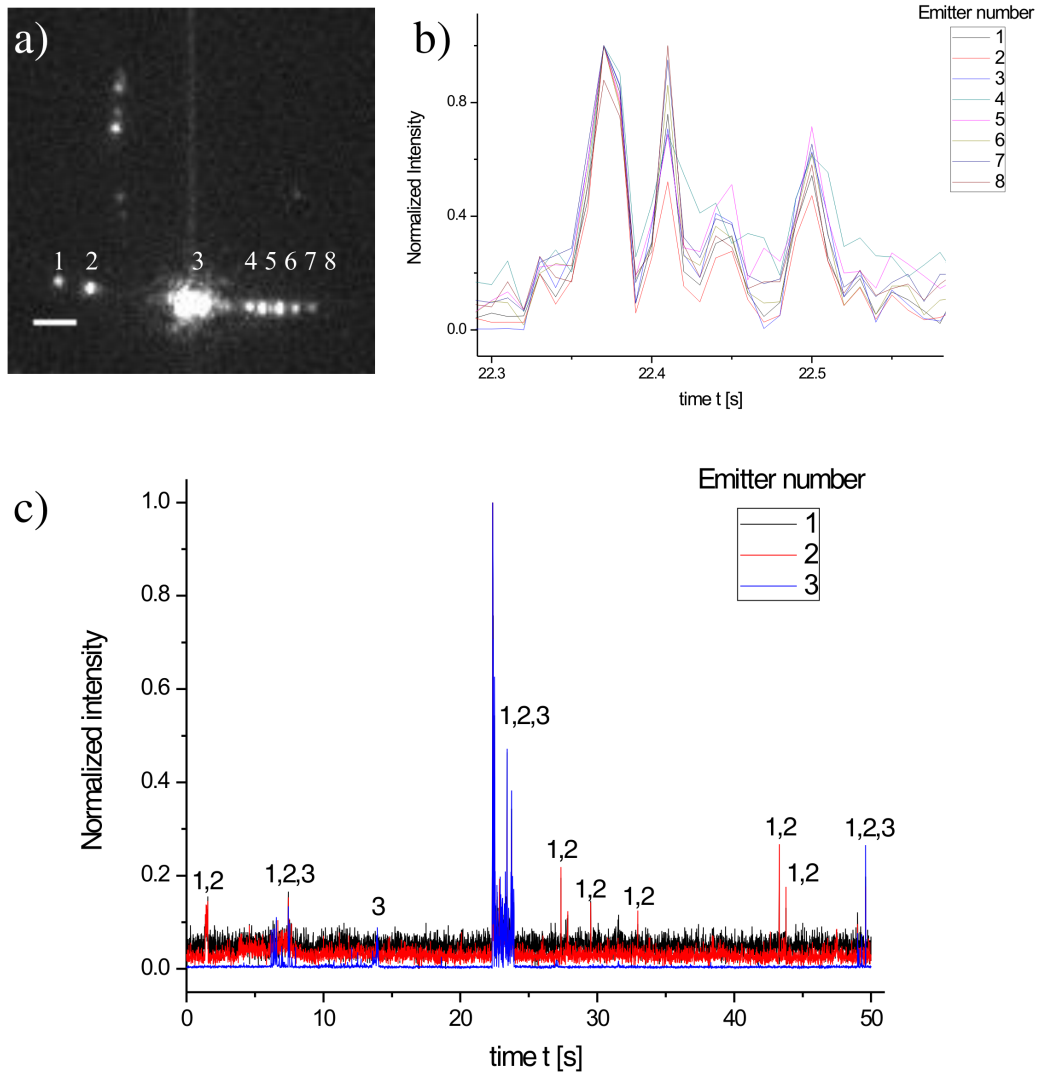
Figure 5.7: Selected wide-field fluorescence image of movie N2 showing cooperative emission from eight emitters on one single nanowire (scale bar is $2\,\mu m$). The computed Pearson's correlation coefficients are given in Table 5.1. (b) Time trajectory of emitted fluorescence intensity from the eight emission sites showing highly correlated intensity fluctuations. The displayed data are only a small fraction of the complete time trajectory. (c) Complete fluorescence time trajectories of cooperative emission from the NW shown in (a). For clarity, only emitters 1, 2, and 3 are displayed. These three emitters exhibit at some times cooperative fluorescence bursts (marked by respective numbers above the trajectory); however, there are also burst events from only two emitters or even from only a single emitter.

always collecting the emission from all emitters. In the case of scattering (i.e. passive emitters), one would still expect to see cooperative emission. However, if there is more than one active center involved, then one will observe emission only at the excited sites and no signal from the sites that

are blocked. The results of an exemplary experiment are shown in Figure 5.8. A single Ag-NW showing cooperative emission from several sites when using wide-field illumination (Figure 5.8a and movie N3a on the Supplementary CD) is shown. If the excitation of either emissive site is physically masked, no fluorescence from it is observed, while the other sites still show emission (Figure 5.8b,c and movie N3b,c on the Supplementary CD). After removing the aperture, the Ag-NW shows again cooperative fluorescence emission (Figure 5.8d and movie N3d on the Supplementary CD) and thus, the emissive centers are active rather than passive scatterers.
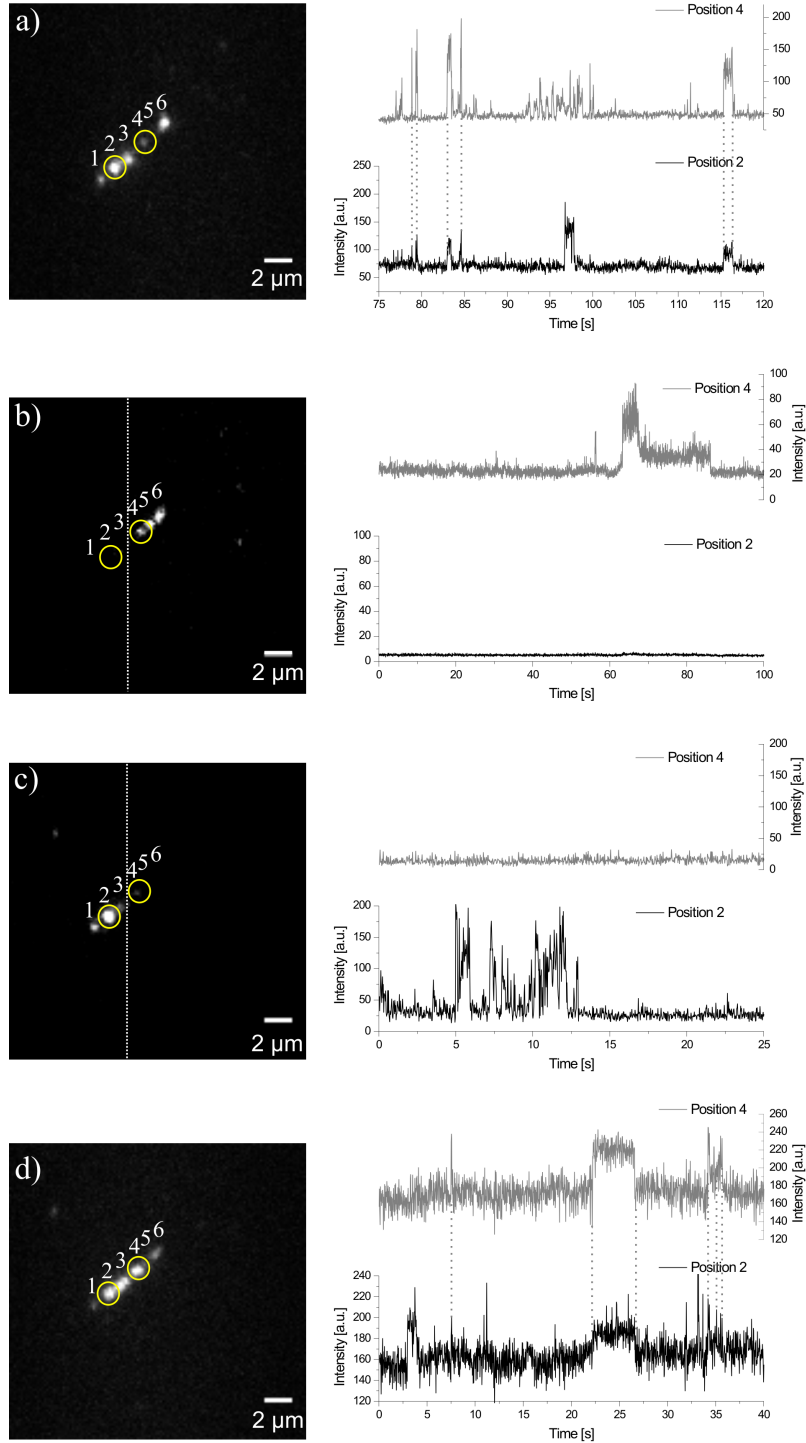
Figure 5.8: Wide-field fluorescence study of two active emitting entities on a Ag-NW. (a) Wide-field image with fluorescence time trajectories for two emitters (positions 2 and 4, marked with yellow circles) exhibiting cooperative fluorescence emission. Using an aperture in the excitation laser pathway from the left (b) or from the right side of the white dotted line (c), only one of these emitters is excited, respectively. Emitters, which are not excited, show no fluorescence emission. (d) Wide-field image and time trajectory taken after the mask has been removed show again cooperative fluorescence emission from positions 2 and 4.
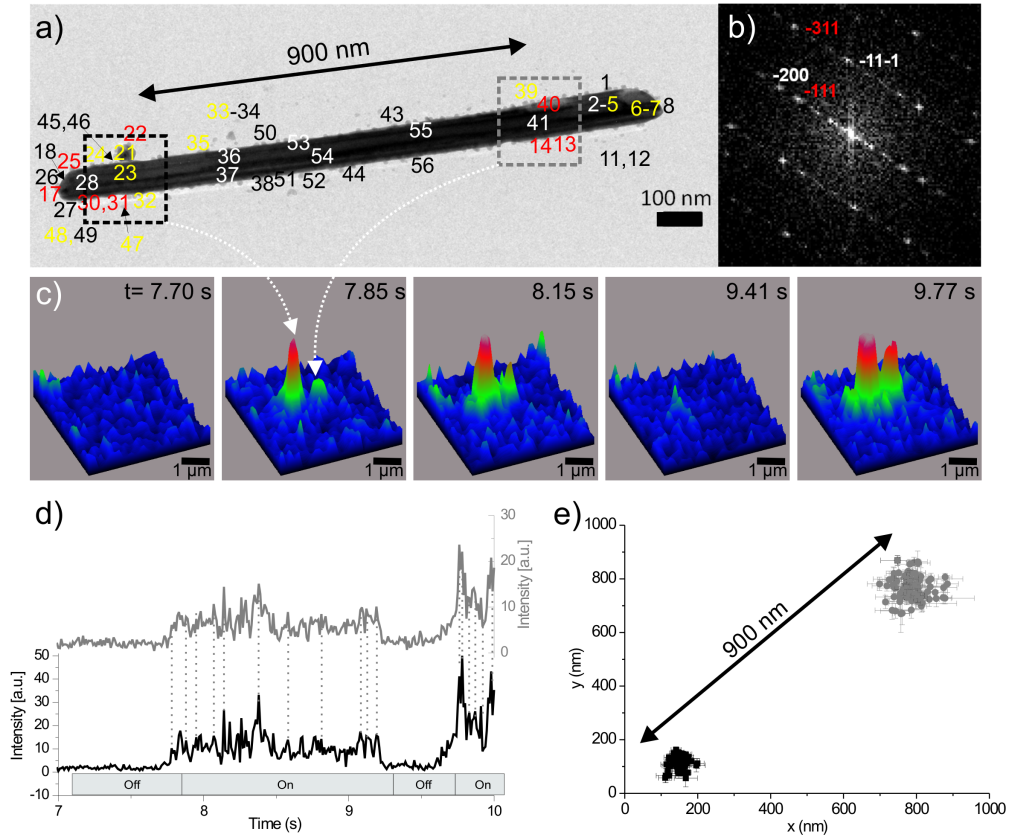
Figure 5.9: (a) Bright-field TEM image of a Ag-NW, showing cooperative fluorescence emission. The position investigated by EDX measurements (data shown in Table 5.2) is marked with numbers (black/white numbers show high Ag values; red numbers contain high Ag and high O values; yellow numbers contain high Ag and high S values). (b) FFT taken from a part of the surface indicates reflections of Ag (marked white) and Ag_2O (marked red) and shows an orientation in [001]. (c) Snapshots of the fluorescence intensity distribution emitted from the same NW displayed by 3D surface plots. The cooperative emission from two spots is marked by arrows. (d) Fluorescence time trajectories of both emitters showing interesting fluctuations of the cooperative effect (marked with dashed lines). (e) Determined positions with corresponding error bars (on average 15 nm (black) and 32 nm (gray)) for both emitters.

5.2.3 Correlation of Optical and Chemical Properties

To unravel structural and chemical reasons for the occurrence of the cooperative effect, we imaged a nanowire by TEM, for which the cooperative effect was observed in the wide-field fluorescence measurements. The TEM image (Figure 5.9a) shows a 1.38 µm long and 80 nm thick Ag-NW surrounded by several small particles. The NW and the nanoparticles were characterized with energy-dispersive X-ray spectroscopy (EDX) measurements in scanning transmission electron microscopy (STEM) mode in detail to correlate optical and chemical properties (Table 5.2).

To find out which parts of the nanowire cause the emission, approximately 50 EDX measurements were performed at different parts of the nanowire and surrounding nanoparticles using an electron

Table 5.2: Values of the quantification of the EDX spectra in order to find out which parts of the nanowire in Figure 5.7a cause the emission, approximately 50 EDX measurements have been performed at different parts of the nanowire and surrounding nanoparicles using a electron beam size of about 1nm.

	1	2	3	4	5	6	7	8	11
O	56,04	38,03	20,34	17,40	17,91	52,91	30,23	13,08	95,60
S	3,32	1,06	1,32	2,33	5,49	4,14	4,69	4,01	2,37
Ag	40,32	60,63	78,33	80,26	76,57	42,95	65,06	82,90	2,01
	12	**13**	**14**	**15**	**17**	**18**	**21**	**22**	**23**
O	87,85	75,65	79,36	47,67	75,26	73,94	34,72	71,15	29,26
S	2,41	0	7,94	4,26	3,45	1,80	7,25	10,59	4,90
Ag	9,27	24,34	12,68	48,05	21,28	24,25	58,02	18,25	65,83
	24	**25**	**28**	**30**	**31**	**32**	**33**	**34**	**35**
O	48,42	75,56	22,77	87,52	88,38	67,01	53,21	40,71	41,25
S	7,03	8,85	4,10	2,81	2,94	11,37	6,48	3,70	7,13
Ag	44,53	15,57	73,10	9,96	8,66	21,61	40,30	55,58	51,81
	36	**37**	**39**	**40**	**41**	**43**	**44**	**45**	**46**
O	8,68	54,61	57,86	26,17	20,74	25,68	19,26	48,97	27,43
S	3,36	2,04	7,67	5,00	2,18	5,52	4,68	6,54	3,67
Ag	87,95	43,26	34,64	68,81	77,06	68,78	76,05	44,47	68,88
	47	**48**	**49**	**50**	**52**	**53**	**54**	**55**	**56**
O	36,71	41,59	26,77	35,91	40,39	36,19	15,78	41,30	42,53
S	6,03	4,49	3,84	4,58	5,80	4,02	3,13	2,92	3,15
Ag	57,25	53,91	69,37	59,49	53,80	59,77	81,08	55,79	54,30

beam size of about 1 nm. Figure 5.9a shows the bright-field image of the Ag-NW together with numbers indicating the positions of the EDX measurements. The values of the quantification of the EDX spectra are given in Table 5.2.

Besides Ag, which was detected at all positions along the nanowire, also O (red numbers) and some traces of S (yellow numbers) were found. The O stems most likely from the thin surface layer described above. The FFT taken from a part of the surface of the Ag-NW (Figure 5.9b) shows reflections of Ag (reflections marked in white) and silver oxide (reflections marked in red). Both the diffraction as well as the FFT data show that most of the particles investigated by EDX contain mainly Ag, and some have a high O content, supporting the presence of silver oxide (e.g. positions 13, 14, 17, 42, 22, 25, 30, and 31). In addition, S, probably originating from air, is detected in parts of the citrate film and in some of the nanoparticles (EDX measurements 5, 6, 7, 14, 21–25, 32, 33, 35, 39, 40, 47, and 48).

The 3D surface plots of the fluorescence intensity (Figure 5.9c) for five frames extracted from a wide-field fluorescence movie (movie N4 on the Supplementary CD) show the coupling of the fluorescence emission between two entities along the nanowire (as imaged by TEM). The corresponding fluorescence intensity time trajectories are depicted in Figure 5.9d (gray and black curves corresponding to the left and right fluorescent spot, respectively). Both appear simultaneously (i.e. within less than 10 ms, the experimental time resolution) at about 7.8 s and disappear simultaneously at about 9.2 s. Between, strong fluorescence intensity fluctuations are detected, which also appear to be synchro-

nized, as highlighted by the dotted line between exemplary simultaneous fluorescence burst events. After 9.6 s, the signals appear again before the measurement stops. For each frame, the determined positions of the two emitters are plotted in Figure 5.9e (gray and black). The average distance between the two cooperative emitters was found to be 911 ± 49 nm.

As the length of this nanowire is 1.38 µm (as determined by TEM), the two emitters are not located at the ends of the NW. However, by inspecting the "map" of the EDX measurements displayed in Figure 5.9a, we were able to identify two regions with high O content (red numbers) separated by about 900 nm (highlighted with the gray and black dotted squares). This observation and the necessity for sample aging in the presence of oxygen for synchronous emission mentioned strongly suggest that one can attribute cooperative emitters to silver clusters which are generated photochemically from silver oxide [187–190] and which are optically coupled through the silver nanowire.

Additional support for the interpretation that the coupled emitters are silver clusters generated photochemically from silver oxide comes from the following observations: TEM studies showed that there is a 2–3 atomic layer thin silver oxide layer around the silver nanowires. During the TEM measurements, it could be observed that exposure of the sample to the electron beam over long time scales damages the citrate layer around the nanowires and also the silver oxide layer. Fluorescence measurements performed directly afterward showed no fluorescence of previously emitting nanowires. Additionally, EDX studies showed that some nanowires, which did not exhibit any fluorescence emission, contained a relatively high amount of sulfide, which might prevent the formation of a silver oxide layer and thus, the generation of a silver cluster.

5.2.4 Conclusions

Single crystalline silver nanowires, synthesized by a seedless wet-chemical approach were investigated using correlated wide-field fluorescence and transmission electron microscopy. While emission of single entities on silver nanostructures is well studied, we observed a coupled emission for some of the investigated NWs (about 35 %). Such a coupled emission can only be observed if several active emitters are investigated simultaneously. Since the emitters are located within a few micrometers on the NW, the coupled emission can be attributed to plasmonic coupling through the wire.

5.2.5 Experimental Part

Crystalline Ag-NWs were synthesized using a seedless, surfactantless wet-chemical fabrication developed by Caswell et al. [186]. This solution, containing about 100 nm thick and up to 15 µm long Ag-NWs, was then spin-coated onto a glass cover slide ($20mm \times 20mm$, thickness 170 µm, Marienfeld). Fluorescence signals from individual nanowires were then collected using a wide-field setup described previously [12]. Briefly, an Eclipse TE200 (Nikon) epi-fluorescence microscope with a high numerical aperture (NA) oil-immersion objective (Nikon Plan Apo 100×, NA = 1.40) was used, and the nanowires were excited at 633 nm with a He-Ne gas laser with an excitation power of 7 mW (measured in front of the microscope). Fluorescence was collected using a combination of filters (dichroic mirror 640 nm cutoff and band-pass 730/140 AHF) and imaged onto a back-illuminated

electron multiplying charge-coupled device (EM-CCD) camera (Andor, iXon DV897). A series of typically 1000 fluorescence images were recorded with a temporal resolution of 10 ms per frame.

In some experiments, we wanted to selectively excite only parts of a Ag-NW. We therefore, placed a physical aperture in the excitation laser pathway in front of the microscope to shrink the excitated area, while keeping the complete detection area.

To combine optical and structural properties, we also performed experiments for which Ag-NWs were deposited on silicon nitride membranes (Si_3N_4, Agar Scientific). For these samples, a different objective lens (Nikon water immersion objective, NA = 1.20, 63×) was used. Some of the optically investigated nanowires were then also studied by TEM in order to correlate fluorescence and structural features. These investigations were done using a FEI Titan 80-300 (S)TEM microscope equipped with a Gatan Tridiem image filter and an EDAX energy-dispersive X-ray spectroscopy detector for analytical measurements. The Titan was operated with 300 kV. A high-angle annular dark-field (HAADF) detector from Fischione Instruments (model 3000) was attached to the microscope for scanning TEM imaging.

Besides the correlative optical and TEM measurements, some Ag-NWs were also investigated only using the TEM measurements, and for these measurements, samples were prepared by placing the Ag-NW on a carbon-coated copper grid (Plano).

6 Appendix

6.1 Ortho-Functionalized Perylenediimides *versus* Fluorescein

In an unpublished study the photostability of three Ortho-functionalized perylenediimid (PDI) derivatives (Ortho-DMB-PDI, Ortho-Ph-PDI, Ortho-PhCOO$^-$-PDI, see Figure 6.1), synthesized in the group of Prof. K. Müllen, were investigated relative to fluorescein.
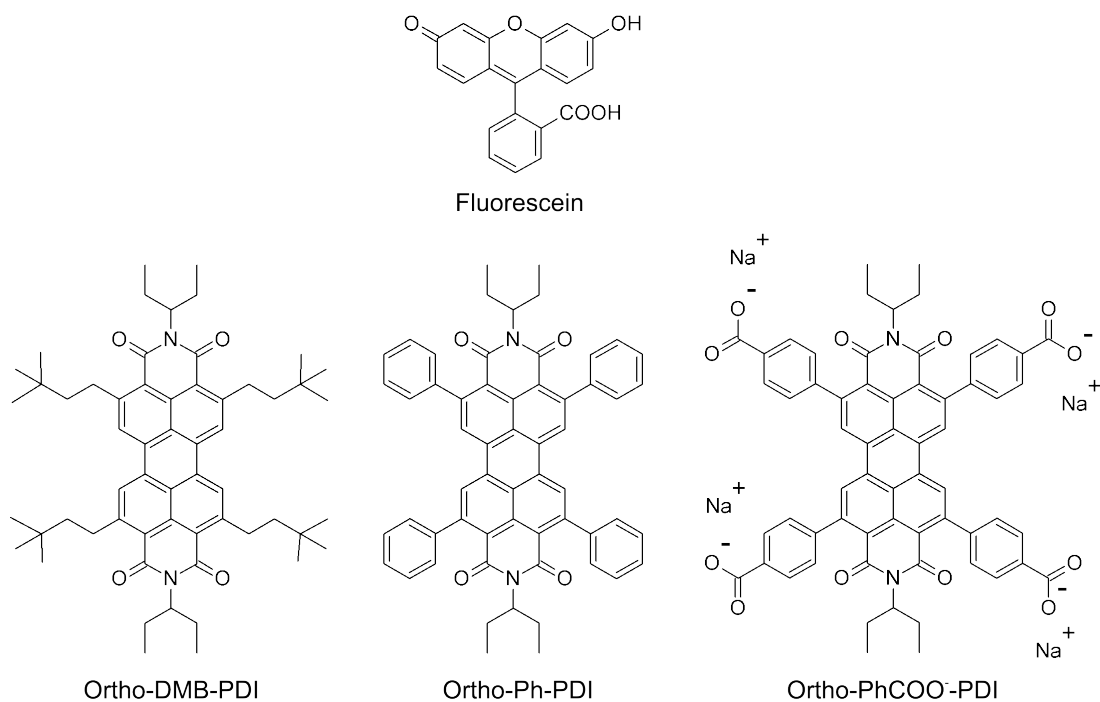
Figure 6.1: Chemical structures of the Ortho-PDI derivatives: Ortho-DMB-PDI, Ortho-Ph-PDI, Ortho-PhCOO$^-$-PDI and Fluorescein.

6.1.1 Single-Molecule Studies

Single-molecule measurements were performed on a homebuilt wide-field microscope (for details see section 6.1.3). The fluorescence intensity trajectories of at least 150 single molecules were recorded for each dye and the number of photon counts from the single-molecule trajectories were obtained. From these data, the probability distribution of photon counts for each dye was calculated (Figure 6.2a). Using the formalism developed by Molski [56], the probability distribution of photon

a)

b)
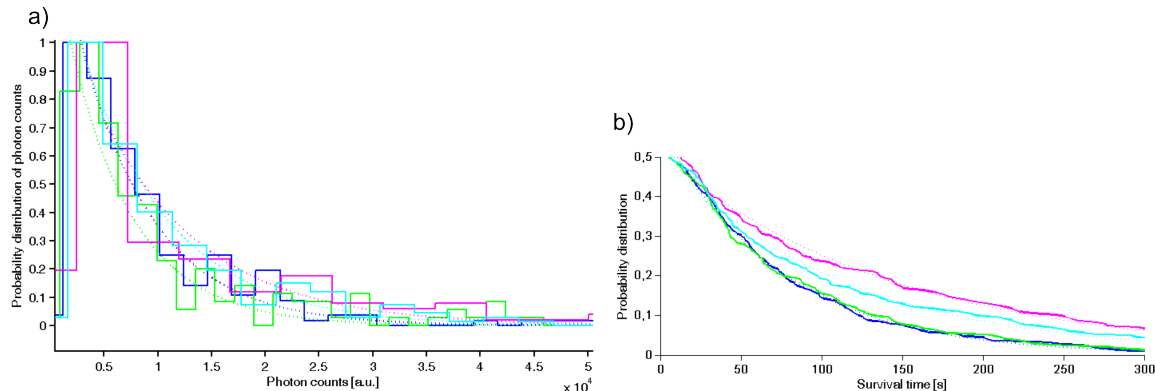
Figure 6.2: (a) Probability distributions of photon counts and (b) survival time for fluorescein (blue) and the PDI derivatives: Ortho-PhCOO⁻-PDI (green), Ortho-DMB-PDI (magenta) and Ortho-Ph-PDI (cyan). All distributions were fitted with a single exponential decay (dot lines).

counts was fitted with a single exponential. From this analysis the characteristic photon counts for each dye were obtained. Furthermore, the survival times of each molecule was obtained from their fluorescence trajectories (Figure 6.2b). The probability distributions of survival times were also calculated and fitted with a single exponential. The median survival times were obtained.

For the purpose of comparison, the results were normalized to the photon counts of fluorescein and are presented in Table 6.1.

Table 6.1: Relative number of photon counts compared to fluorescein and the survival time of different dyes in PMMA.

Fluorophore	Relative number of photon counts compared to fluorescein	Survival time in PMMA [s]
Fluorescein	1.00	73
Ortho-PhCOO⁻-PDI	0.88	77
Ortho-Ph-PDI	1.21	112
Ortho-DMB-PDI	1.41	142

Ortho-PhCOO⁻-PDI showed only 88% of the emitted photon counts relative to fluorescein, whereas Ortho-Ph-PDI (121%) and Ortho-DMB-PDI (141%) had higher numbers of photon counts than fluorescein.

The results show that with the exception of Ortho-PhCOO⁻-PDI the investigated perylene dyes are more photostable than fluorescein. Furthermore, the longer survival time of Ortho-PhCOO⁻-PDI compared to fluorescein together with the shorter number of photon counts clearly shows that this dye has more blinking events, which are characteristic for charged molecules.

6.1.2 Conclusion

Considering the number of relative photon counts to fluorescein and the median survival time, the following trend of the photostability of the investigated dyes can be established:

Ortho-DMB-PDI > Ortho-Ph-PDI > fluorescein > Ortho-PhCOO$^-$-PDI.

Our results show that Ortho-DMB-PDI is most suited for single-molecule studies of the dyes investigated.

6.1.3 Experimental Part

Wide-Field Microscopy: To investigate the photostability of the PDI derivatives (Ortho-DMB-PDI, Ortho-Ph-PDI, Ortho-PhCOO$^-$-PDI) on a single-molecule level, the dyes were fixed in a polymer matrix (poly-(methylmethacrylate), PMMA). Thin polymer films (thickness $100 - 200$ nm) with dye were prepared by spin-coating fluorophores in polymer solutions at a concentration of 10^{-10} – 10^{-11} M (1 min at 3000 rpm, 2 wt %/wt PMMA in chloroform). In addition, the photostability of fluorescein was investigated and used as a reference. The fluorescence signal was monitored by a homebuilt wide-field microscope based on a Nikon Eclipse Ti microscope corpus. The dyes were excited at their side maximum absorption band at 488 nm with a single longitudinal mode Laser (Picarro, Cyan Laser). The excitation power was set to 1.3 mW. The laser beam was expanded and focused onto the back-focal plane of a microscope objective (Nikon ×60 1.49 NA oil immersion objective). Fluorescence was collected by the same objective, separated from backscattered laser light with a combination of filters (dichroic mirror R405/488/561/635, Chroma and band-pass BP525/50, Semrock), and imaged onto a back-illuminated EMCCD detector (Andor Ixon887 camera). Movies were recorded with an integration time of 500 ms per frame for all measurements. The number of emitted photon counts and the survival time was extracted from the fluorescence time trajectories of individual molecules by a custom-written Matlab program.

List of Abbreviations

1D	one-dimensional
2D	two-dimensional
3D	three-dimensional
AFM	Atomic force microscopy
Ag-NW	Silver nanowire
APD	Avalanche photodiode
BF	Bright-field
Brij 56	Decaethylene glycol hexadecyl ether or
	Polyoxyethylene 10 cetyl ether
CCD	Charge coupled device
CMC	Critical micelle concentration
CTAB	Cetyltrimethylammoniumăbromide
DNA	Deoxyribonucleic acid
EDX	Energy dispersive X-ray spectroscopy
e.g.	Exempli gratia
EISA	Evaporation-induced self-assembly
EM-CCD	Electron multiplying charge coupled device
et al.	Et alii
FFT	Fast Fourier transformation
FRET	Förster resonance energy transfer
fps	Frames per second
HAADF	High-angle annular dark-field
HRTEM	High resolution transmission electron microscopy
IC	Internal conversion
i.e.	Id est
ISC	Intersystem crossing
IUPAC	International Union of Pure and Applied Chemistry
LASER	Light amplification by stimulated emission of radiation
LSPRs	Localized surface plasmon resonance
MCM	Mobil catalytic material
MIMIC	Micromolding in Capillary
MSD	Mean square displacement
NA	Numerical aperture
NMR	Nuclear magnetic resonance
OD	Optical density
PDI	Perylene diimide
PDMS	Poly-(dimethylsiloxane)
PEG	Polyethylene glycol
PFOTS	1H,1H,2H,2H-Perfluorooctyltriethoxysilane
Pluronic F127	Poly(oxyethylene)-poly(oxypropylene) triblock copolymer
Pluronic P123	Poly(ethylene oxide)$_{20}$-poly(propylene oxide)$_{70}$-
	poly(ethylene oxide)$_{20}$

PMMA	Polymethyl methacrylat
PVA	Polyvinylalkohol
PVP	Polyvinylpyrrolidone
rpm	Rounds per minute
SBA	Santa Barbara Acidic
SEM	Scanning electron microscopy
SMS	Single-molecule spectroscopy
SMT	Single-molecule tracking
SPR	Surface plasmon resonance
STEM	Scanning transmission electron microscopy
SPT	Single particle tracking
TDI	Terrylene diimide
TEM	Transmission electron microscopy
TEOS	Tetraethyl orthosilicate
TIRF	Total internal reflection
UV-Vis	Ultraviolet-visible
XRD	X-ray diffraction

Bibliography

[1] W. E. Moerner and L. Kador. Optical detection and spectroscopy of single molecules in a solid. *Phys. Rev. Lett.*, 62(21):2535–2538, 1989.

[2] M. Orrit and J. Bernard. Single pentacene molecules detected by fluorescence excitation in a p-terphenyl crystal. *Phys. Rev. Lett.*, 65(21):2716–2719, 1990.

[3] Chemistry 1st Nobel Conference of "Single Molecules in Physics and Biology". *Single Molecule Spectroscopy: Nobel Conference Lectures.* Springer Berlin Heidelberg (2001), 1998.

[4] Chemistry 2nd Nobel Conference of "Single Molecules in Physics and Biology". *Single Molecule Spectroscopy in Chemistry, Physics and Biology Nobel Symposium*, volume 96 of *Springer Series in Chemical Physics.* Springer Berlin Heidelberg (2010), 2008.

[5] S. Weiss. Fluorescence Spectroscopy of Single Biomolecules. *Science*, 283(5408):1676–1683, 1999.

[6] P. Tamarat, A. Maali, B. Lounis, and M. Orrit. Ten Years of Single-Molecule Spectroscopy. *J. Phys. Chem. A*, 104(1):1–16, 1999.

[7] W. E. Moerner. A Dozen Years of Single-Molecule Spectroscopy in Physics, Chemistry, and Biophysics. *J. Phys. Chem. B*, 106(5):910–927, 2002.

[8] R. Lewis, H. Dürr, K.P. Hopfner, and J. Michaelis. Conformational changes of a Swi2/Snf2 ATPase during its mechano-chemical cycle. *Nucleic Acids Research*, 36(6):1881–1890, 2008.

[9] K. Mapa, M. Sikor, V. Kudryavtsev, K. Waegemann, S. Kalinin, C. A. M. Seidel, W. Neupert, D. C. Lamb, and D. Mokranjac. The conformational dynamics of the mitochondrial Hsp70 chaperone. *Molecular Cell*, 38(1):89 – 100, 2010.

[10] H. P. Lu, L. Xun, and X. S. Xie. Single-molecule enzymatic dynamics. *Science*, 282(5395):1877–1882, 1998.

[11] M. B. J. Roeffaers, B. F. Sels, H. Uji-i, F. C. De Schryver, P. A. Jacobs, D. E. De Vos, and J. Hofkens. Spatially resolved observation of crystal-face-dependent catalysis by single turnover counting. *Nature*, 439(7076):572–575, 2006.

[12] J. Kirstein, B. Platschek, C. Jung, R. Brown, T. Bein, and C. Bräuchle. Exploration of nanostructured channel systems with single-molecule probes. *Nat. Mater.*, 6(4):303–310, 2007.

[13] G. Seisenberger, M. U. Ried, T. Endress, H. Buning, M. Hallek, and C. Bräuchle. Real-time single-molecule imaging of the infection pathway of an adeno-associated virus. *Science*, 294(5548):1929–32, 2001.

[14] A. Yildiz, J. N. Forkey, S. A. McKinney, T. Ha, Y. E. Goldman, and P. R. Selvin. Myosin V walks hand-over-hand: single fluorophore imaging with 1.5 nm localization. *Science*, 300(5628):2061–5, 2003.

[15] F. Feil, S. Naumov, J. Michaelis, R. Valiullin, D. Enke, J. Kärger, and C. Bräuchle. Single-particle and ensemble diffusivities-test of ergodicity. *Angewandte Chemie*, 124(5):1178–1181, 2012.

[16] J. W. Lichtman and J. A. Conchello. Fluorescence microscopy. *Nat Meth*, 2(12):910–919, 2005.

[17] E. M. Davies. Synthese und Charakterisierung von Silbernanodrähten sowie Plasmonenver-stärkung von Fluoreszenzfarbstoffen. *Master Thesis, LMU München*, 2009.

[18] C. Jung. Single molecule traffic in mesoporous materials and new photostable water-soluble terrylenediimide derivatives. *PhD Thesis, LMU München*, 2007.

[19] U. Kubitscheck, O. Kuckmann, T. Kues, and R. Peters. Imaging and tracking of single gfp molecules in solution. *Biophysical Journal*, 78(4):2170–9, 2000.

[20] G. J. Schütz, H. Schindler, and T. Schmidt. Single-molecule microscopy on model membranes reveals anomalous diffusion. *Biophysical Journal*, 73(2):1073–1080, 1997.

[21] C.M. Anderson, G.N. Georgiou, I.E. Morrison, G.V. Stevenson, and R.J. Cherry. Tracking of cell surface receptors by fluorescence digital imaging microscopy using a charge-coupled device camera. low-density lipoprotein and influenza virus receptor mobility at 4 degrees C. *Journal of Cell Science*, 101(2):415–425, 1992.

[22] M. K. Cheezum, W. F. Walker, and W. H. Guilford. Quantitative comparison of algorithms for tracking single fluorescent particles. *Biophysical Journal*, 81(4):2378–2388, 2001.

[23] J. U. Kirstein. Diffusion of single molecules in nanoporous mesostructured materials. *PhD Thesis, LMU München*, 2007.

[24] R. Brown. A brief account of microscopical observations made in the months of june, july and august 1827, on the particles contained in the pollen of plants; and on the general existence of active molecules in organic and inorganic bodies. *Philosophical Magazine*, 4(21):161–173, 1828.

[25] H.C. Berg. *Random Walks in Biology.* Princeton University Press, new, expanded edition, 1993.

[26] M.J. Saxton. Lateral diffusion in an archipelago. single-particle diffusion. *Biophysical Journal*, 64(6):1766 – 1780, 1993.

[27] M. Saxton and K. Jacobson. Single-particle tracking: Applications to membrane dynamics. *Annu. Rev. Biophys. Biomol. Struct.*, 26:373–399, 1997.

[28] T.J. Feder, I. Brust-Mascher, J.P. Slattery, B. Baird, and W.W. Webb. Constrained diffusion or immobile fraction on cell surfaces: a new interpretation. *Biophysical Journal*, 70(6):2767 – 2773, 1996.

[29] K. V. Datye. *Colourage Annu.*, 3:0, 1988.

[30] J. Lee. Textile wet processing: Preparation, dyeing and finishing of today's textile fabrics. *Conference*, VIII/0, 1998.

[31] V. G. Agnihotri. *Colourage*, 23:1, 1976.

[32] H. Zollinger. *Color Chemistry.* Wiley-VCH, New York, 3rd edition, 2001.

[33] C. Jung, N. Ruthardt, R. Lewis, J. Michaelis, B. Sodeik, F. Nolde, K. Peneva, K. Müllen, and C. Bräuchle. Photophysics of new water-soluble terrylenediimide derivatives and applications in biology. *Chemphyschem*, 10(1):180–190, 2009.

[34] C. Jung, B. K. Müller, D. C. Lamb, F. Nolde, K. Müllen, and C. Bräuchle. A new photo-stable terrylene diimide dye for applications in single molecule studies and membrane labeling. *Journal of the American Chemical Society*, 128(15):5283–5291, 2006.

[35] X. Michalet, A. N. Kapanidis, T. Laurence, F. Pinaud, S. Doose, M. Pflughoefft, and S. Weiss. The power and prospects of fluorescence microscopies and spectroscopies. *Annual review of biophysics and biomolecular structure*, 32:161–82, 2003.

[36] S. Weiss. Measuring conformational dynamics of biomolecules by single molecule fluorescence spectroscopy. *Nature structural biology*, 7(9):724–9, 2000.

[37] T. Ha. Single-molecule fluorescence resonance energy transfer. *Methods*, 25(1):78–86, 2001.

[38] X. Michalet and S. Weiss. Single-molecule spectroscopy and microscopy. *Phys.*, 3:619, 2002.

[39] E. Haustein and P. Schwille. Single-molecule spectroscopic methods. *Current opinion in structural biology*, 14(5):531–40, 2004.

[40] E. J. Peterman, H. Sosa, and W. E. Moerner. Single-molecule fluorescence spectroscopy and microscopy of biomolecular motors. *Annual review of physical chemistry*, 55:79–96, 2004.

[41] J. Lippincott-Schwartz, E. Snapp, and A. Kenworthy. Studying protein dynamics in living cells. *Nature reviews. Molecular cell biology*, 2(6):444–56, 2001.

[42] K. G. de Bruin, C. Fella, M. Ogris, E. Wagner, N. Ruthardt, and C. Bräuchle. Dynamics of photoinduced endosomal release of polyplexes. *Journal of controlled release*, 130(2):175–82, 2008.

[43] A. M. Sauer, A. Schlossbauer, N. Ruthardt, V. Cauda, T. Bein, and C. Bräuchle. Role of Endosomal Escape for Disulfide-Based Drug Delivery from Colloidal Mesoporous Silica Evaluated by Live-Cell Imaging. *Nano Lett.*, 10(9):3684–3691, 2010.

[44] G. J. Schutz, M. Sonnleitner, P. Hinterdorfer, and H. Schindler. Single molecule microscopy of biomembranes (review). *Molecular membrane biology*, 17(1):17–29, 2000.

[45] K. Kolmakov, V. N. Belov, J. Bierwagen, C. Ringemann, V. Müller, C. Eggeling, and S. W. Hell. Red-emitting rhodamine dyes for fluorescence microscopy and nanoscopy. *Chemistry*, 16(1):158–66, 2010.

[46] Y. Avlasevich, C. Li, and K. Müllen. Synthesis and applications of core-enlarged perylene dyes. *Journal of Materials Chemistry*, 20(19):3814–3826, 2010.

[47] A. C. Grimsdale and K. Müllen. The chemistry of organic nanomaterials. *Angewandte Chemie-International Edition*, 44(35):5592–5629, 2005.

[48] H. Langhals. Control of the interactions in multichromophores: Novel concepts. perylene bis-imides as components for larger functional units. *Helvetica Chimica Acta*, 88(6):1309–1343, 2005.

[49] F. Nolde, J. Q. Qu, C. Kohl, N. G. Pschirer, E. Reuther, and K. Müllen. Synthesis and modification of terrylenediimides as high-performance fluorescent dyes. *Chemistry-a European Journal*, 11(13):3959–3967, 2005.

[50] A. Margineanu, J. Hofkens, M. Cotlet, S. Habuchi, A. Stefan, J. Qu, C. Kohl, K. Müllen, J. Vercammen, Y. Engelborghs, T. Gensch, and F. C. De Schryver. Photophysics of a water-soluble rylene dye: Comparison with other fluorescent molecules for biological applications. *The Journal of Physical Chemistry B*, 108(32):12242–12251, 2004.

[51] K. Peneva, G. Mihov, A. Herrmann, N. Zarrabi, M. Börsch, T. M. Duncan, and K. Müllen. Exploiting the nitrilotriacetic acid moiety for biolabeling with ultrastable perylene dyes. *Journal of the American Chemical Society*, 130(16):5398–5399, 2008.

[52] F. Würthner, C. Thalacker, Si. Diele, and C. Tschierske. Fluorescent J-type aggregates and thermotropic columnar mesophases of perylene bisimide dyes. *Chemistry - A European Journal*, 7(10):2245–2253, 2001.

[53] S. B. Brichkin, M. A. Kurandina, T. M. Nikolaeva, and V. F. Razumov. Effects of surfactants on the spectral properties of carbocyanine dyes in solutions. *High Energy Chemistry*, 38(6):373–381, 2004.

[54] S. Das, K. G. Thomas, K. J. Thomas, V. Madhavan, D. Liu, P. V. Kamat, and M. V. George. Aggregation behavior of water soluble bis(benzothiazolylidene)squaraine derivatives in aqueous media. *The Journal of Physical Chemistry*, 100(43):17310–17315, 1996.

[55] J. Franck and E. Teller. Migration and photochemical action of excitation energy in crystals. *J. Chem. Phys.*, 6(12):861–872, 1938.

[56] A. Molski. Statistics of the bleaching number and the bleaching time in single-molecule fluorescence spectroscopy. *The Journal of chemical physics*, 114(3):1142–1147, 2001.

[57] R. Zondervan, F. Kulzer, M. A. Kolchenk, and M. Orrit. Photobleaching of rhodamine 6G in poly(vinyl alcohol) at the ensemble and single-molecule levels. *The Journal of Physical Chemistry A*, 108(10):1657–1665, 2004.

[58] T. A. Vida and S. D. Emr. A new vital stain for visualizing vacuolar membrane dynamics and endocytosis in yeast. *The Journal of cell biology*, 128(5):779–92, 1995.

[59] S. Fischer-Parton, R. M. Parton, P. C. Hickey, J. Dijksterhuis, H. A. Atkinson, and N. D. Read. Confocal microscopy of FM4-64 as a tool for analysing endocytosis and vesicle trafficking in living fungal hyphae. *Journal of microscopy*, 198(Pt 3):246–59, 2000.

[60] H. Kaiser, J. Lindner, and H. Langhals. Synthese von nichtsymmetrisch substituierten perylen-fluoreszenzfarbstoffen. *Chemische Berichte*, 124(3):529–535, 1991.

[61] M. R. Hansen, T. Schnitzler, W. Pisula, R. Graf, K. Müllen, and H. W. Spiess. Cooperative molecular motion within a self-assembled liquid-crystalline molecular wire: the case of a teg-substituted perylenediimide disc. *Angewandte Chemie*, 48(25):4621–4, 2009.

[62] F. Nolde, W. Pisula, S. Müller, C. Kohl, and K. Müllen. Synthesis and self-organization of core-extended perylene tetracarboxdiimides with branched alkyl substituents. *Chemistry of Materials*, 18(16):3715–3725, 2006.

[63] D. Magde, R. Wong, and P. G. Seybold. Fluorescence quantum yields and their relation to lifetimes of rhodamine 6G and fluorescein in nine solvents: improved absolute standards for quantum yields. *Photochemistry and photobiology*, 75(4):327–34, 2002.

[64] J. R. Lakowicz. *Principles of Fluorescence Spectroscopy*. Plenum Press, New York, 2nd edition, 1999.

[65] M. Davies, C. Jung, P. Wallis, T. Schnitzler, C. Li, K. Müllen, and C. Bräuchle. Photophysics of new photostable rylene derivatives: applications in single-molecule studies and membrane labelling. *Chemphyschem*, 12(8):1588–95, 2011.

[66] J. Qu, C. Kohl, M. Pottek, and K. Müllen. Ionic perylenetetracarboxdiimides: highly fluorescent and water-soluble dyes for biolabeling. *Angewandte Chemie*, 43(12):1528–31, 2004.

[67] T. Weil, T. Vosch, J. Hofkens, K. Peneva, and K. Müllen. The rylene colorant family–tailored nanoemitters for photonics research and applications. *Angewandte Chemie*, 49(48):9068–93, 2010.

[68] T. Cordes, J. Vogelsang, M. Anaya, C. Spagnuolo, A. Gietl, W. Summerer, A. Herrmann, K. Müllen, and P. Tinnefeld. Single-molecule redox blinking of perylene diimide derivatives in water. *Journal of the American Chemical Society*, 132(7):2404–9, 2010.

[69] K. Peneva, G. Mihov, F. Nolde, S. Rocha, J. Hotta, K. Braeckmans, J. Hofkens, H. Uji-i, A. Herrmann, and K. Müllen. Water-soluble monofunctional perylene and terrylene dyes: powerful labels for single-enzyme tracking. *Angewandte Chemie*, 47(18):3372–5, 2008.

[70] S. Nakazono, Y. Imazaki, H. Yoo, J. Yang, T. Sasamori, N. Tokitoh, T. Cedric, H. Kageyama, D. Kim, H. Shinokubo, and A. Osuka. Regioselective Ru-catalyzed direct 2,5,8,11-alkylation of perylene bisimides. *Chemistry*, 15(31):7530–3, 2009.

[71] J. E. Bullock, M. T. Vagnini, C. Ramanan, D. T. Co, T. M. Wilson, J. W. Dicke, T. J. Marks, and M. R. Wasielewski. Photophysics and redox properties of rylene imide and diimide dyes alkylated ortho to the imide groups. *The Journal of Physical Chemistry B*, 114(5):1794–1802, 2010.

[72] V. Kamm, G. Battagliarin, I. A. Howard, W. Pisula, A. Mavrinskiy, C. Li, K. Müllen, and F. Laquai. Polythiophene:perylene diimide solar cells - the impact of alkyl-substitution on the photovoltaic performance. *Advanced Energy Materials*, 1(2):297–302, 2011.

[73] C. Feng, Y. Liu, S. Peng, Q. Shuai, G. Deng, and C. J. Li. Ruthenium-catalyzed tertiary amine formation from nitroarenes and alcohols. *Organic letters*, 12(21):4888–91, 2010.

[74] N. A. Owston, A. J. Parker, and J. M. Williams. Highly efficient ruthenium-catalyzed oxime to amide rearrangement. *Organic letters*, 9(18):3599–601, 2007.

[75] F. Shibahara, J. F. Bower, and M. J. Krische. Diene hydroacylation from the alcohol or aldehyde oxidation level via ruthenium-catalyzed c-c bond-forming transfer hydrogenation: synthesis of beta,gamma-unsaturated ketones. *Journal of the American Chemical Society*, 130(43):14120–2, 2008.

[76] P. A. Slatford, M. K. Whittlesey, and J. M. J. Williams. C-C bond formation from alcohols using a xantphos ruthenium complex. *Tetrahedron Letters*, 47(38):6787–6789, 2006.

[77] S. Ueno, E. Mizushima, N. Chatani, and F. Kakiuchi. Direct observation of the oxidative addition of the aryl carbon-oxygen bond to a ruthenium complex and consideration of the relative reactivity between aryl carbon-oxygen and aryl carbon-hydrogen bonds. *Journal of the American Chemical Society*, 128(51):16516–7, 2006.

[78] F. Kakiuchi and N. Chatani. Catalytic methods for c-h bond functionalization: Application in organic synthesis. *Advanced Synthesis & Catalysis*, 345(9-10):1077–1101, 2003.

[79] C. E. McKenna and J. Schmidhuser. Functional selectivity in phosphonate ester dealkylation with bromotrimethylsilane. *Journal of the Chemical Society, Chemical Communications*, 0(17):739–739, 1979.

[80] L. Jimenez-Garcia, A. Kaltbeitzel, W. Pisula, J. Gutmann, M. Klapper, and K. Müllen. Phosphonated hexaphenylbenzene: A crystalline proton conductor. *Angewandte Chemie International Edition*, 48(52):9951–9953, 2009.

[81] L. Jimenez-Garcia, A. Kaltbeitzel, W. Pisula, J. Gutmann, M. Klapper, and K. Müllen. Phosphoniertes hexaphenylbenzol - ein kristalliner Protonenleiter. *Angewandte Chemie*, 121(52):10135–10138, 2009.

[82] K. E. Borbas, P. Mroz, M. R. Hamblin, and J. S. Lindsey. Bioconjugatable porphyrins bearing a compact swallowtail motif for water solubility. *Bioconjugate chemistry*, 17(3):638–653, 2006.

[83] M. V. Reddington. Synthesis and properties of phosphonic acid containing cyanine and squaraine dyes for use as fluorescent labels. *Bioconjugate chemistry*, 18(6):2178–2190, 2007.

[84] M. J. Wirth, R. W. P. Fairbank, and H. O. Fatunmbi. Mixed self-assembled monolayers in chemical separations. *Science*, 275(5296):44–47, 1997.

[85] M. J. Wirth, D. J. Swinton, and M. D. Ludes. Adsorption and Diffusion of Single Molecules at Chromatographic Interfaces. *J. Phys. Chem. B*, 107(26):6258–6268, 2003.

[86] Avelino Corma. From Microporous to Mesoporous Molecular Sieve Materials and Their Use in Catalysis. *Chem. Rev.*, 97(6):2373–2420, 1997.

[87] M. Jaroniec. Molecular Sieves: Science and Technology. *J. Am. Chem. Soc.*, 124(48):14506–14506, 2002.

[88] P.C. Pandey, S. Upadhyay, and H.C. Pathak. A new glucose sensor based on encapsulated glucose oxidase within organically modified sol-gel glass. *Sensors and Actuators B: Chemical*, 60(2-3):83–89, 1999.

[89] C. Y. Lai, B. G. Trewyn, D. M. Jeftinija, K. Jeftinija, S. Xu, S. Jeftinija, and V. S.-Y. Lin. A Mesoporous Silica Nanosphere-Based Carrier System with Chemically Removable CdS Nanoparticle Caps for Stimuli-Responsive Controlled Release of Neurotransmitters and Drug Molecules. *J. Am. Chem. Soc.*, 125(15):4451–4459, 2003.

[90] D. J. Bharali, I. Klejbor, E. K. Stachowiak, P. Dutta, I. Roy, N. Kaur, E. J. Bergey, P. N. Prasad, and M. K. Stachowiak. Organically modified silica nanoparticles: A nonviral vector for in vivo gene delivery and expression in the brain. *Proc. Natl. Acad. Sci. U. S. A.*, 102(32):11539–11544, 2005.

[91] V. Kukla, J. Kornatowski, D. Demuth, I. Girnus, H. Pfeifer, L. V. C. Rees, S. Schunk, K. K. Unger, and J. Kärger. NMR Studies of Single-File Diffusion in Unidimensional Channel Zeolites. *Science*, 272(5262):702–704, 1996.

[92] O. Terasaki, Z. Liu, T. Ohsuna, H. J. Shin, and R. Ryoo. Electron Microscopy Study of Novel Pt Nanowires Synthesized in the Spaces of Silica Mesoporous Materials. *Microsc. Microanal.*, 8(01):35–39, 2002.

[93] N. E. Benes, H. Jobic, and H. Verweij. Quasi-elastic neutron scattering study of the mobility of methane in microporous silica. *Microporous Mesoporous Mater.*, 43(2):147–152, 2001.

[94] R. M. Barrer and G. S. Perry. 179. Sorption of mixtures, and selectivity in alkylammonium montmorillonites. Part I. Monomethylammonium bentonite. *J. Chem. Soc.*, 0(0):842–849, 1961.

[95] C. T. Kresge, M. E. Leonowicz, W. J. Roth, J. C. Vartuli, and J. S. Beck. Ordered mesoporous molecular sieves synthesized by a liquid-crystal template mechanism. *Nature*, 359(6397):710–712, 1992.

[96] G. J. de AA. Soler-Illia, C. Sanchez, B. Lebeau, and J. Patarin. Chemical Strategies To Design Textured Materials: from Microporous and Mesoporous Oxides to Nanonetworks and Hierarchical Structures. *Chem. Rev.*, 102(11):4093–4138, 2002.

[97] C. G. Goltner and M. Antonietti. Mesoporous materials by templating of liquid crystalline phases. *Adv. Mater.*, 9(5):431–436, 1997.

[98] D. Zhao, P. Yang, N. Melosh, J. Feng, B. F. Chmelka, and G. D. Stucky. Continuous Mesoporous Silica Films with Highly Ordered Large Pore Structures. *Adv. Mater.*, 10(16):1380–1385, 1998.

[99] I. A. Aksay, M. Trau, S. Manne, I. Honma, N. Yao, L. Zhou, P. Fenter, P. M. Eisenberger, and S. M. Gruner. Biomimetic Pathways for Assembling Inorganic Thin Films. *Science*, 273(5277):892–898, 1996.

[100] M. Ogawa. A simple sol-gel route for the preparation of silica-surfactant mesostructured materials. *Chem. Commun.*, 0(10):1149–1150, 1996.

[101] H. Yang, A. Kuperman, N. Coombs, S. Mamiche-Afara, and G. A. Ozin. Synthesis of oriented films of mesoporous silica on mica. *Nature*, 379(6567):703–705, 1996.

[102] C. J. Brinker, Y. Lu, A. Sellinger, and H. Fan. Evaporation-Induced Self-Assembly: Nanostructures Made Easy. *Adv. Mater.*, 11(7):579–585, 1999.

[103] Y. Lu, R. Ganguli, C. A. Drewien, M. T. Anderson, C. J. Brinker, W. Gong, Y. Guo, H. Soyez, B. Dunn, M. H. Huang, and J. I. Zink. Continuous formation of supported cubic and hexagonal mesoporous films by sol-gel dip-coating. *Nature*, 389(6649):364–368, 1997.

[104] M. Ogawa. Formation of Novel Oriented Transparent Films of Layered Silica-Surfactant Nanocomposites. *J. Am. Chem. Soc.*, 116(17):7941–7942, 1994.

[105] D. A. Doshi, A. Gibaud, V. Goletto, M. Lu, H. Gerung, B. Ocko, S. M. Han, and C. J. Brinker. Peering into the Self-Assembly of Surfactant Templated Thin-Film Silica Mesophases. *J. Am. Chem. Soc.*, 125(38):11646–11655, 2003.

[106] D. Grosso, F. Babonneau, P. A. Albouy, H. Amenitsch, A. R. Balkenende, A. Brunet-Bruneau, and J. Rivory. An in Situ Study of Mesostructured CTAB-Silica Film Formation during Dip Coating Using Time-Resolved SAXS and Interferometry Measurements. *Chem. Mater.*, 14(2):931–939, 2002.

[107] B. Smarsly, A. Gibaud, W. Ruland, D. Sturmayr, and C. J. Brinker. Quantitative SAXS Analysis of Oriented 2D Hexagonal Cylindrical Silica Mesostructures in Thin Films Obtained from Nonionic Surfactants. *Langmuir*, 21(9):3858–3866, 2005.

[108] D. Grosso, A. R. Balkenende, P. A. Albouy, A. Ayral, H. Amenitsch, and F. Babonneau. Two-Dimensional Hexagonal Mesoporous Silica Thin Films Prepared from Block Copolymers: Detailed Characterization and Formation Mechanism. *Chem. Mater.*, 13(5):1848–1856, 2001.

[109] J. S. Beck, J. C. Vartuli, W. J. Roth, M. E. Leonowicz, C. T. Kresge, K. D. Schmitt, C. T. W. Chu, D. H. Olson, and E. W. Sheppard. A new family of mesoporous molecular sieves prepared with liquid crystal templates. *J. Am. Chem. Soc.*, 114(27):10834–10843, 1992.

[110] G. S. Attard, J. C. Glyde, and C. G. Goltner. Liquid-crystalline phases as templates for the synthesis of mesoporous silica. *Nature*, 378(6555):366–368, 1995.

[111] D. Wan, Y.and Zhao. On the Controllable Soft-Templating Approach to Mesoporous Silicates. *Chem. Rev.*, 107(7):2821–2860, 2007.

[112] C. Jung, P. Schwaderer, M. Dethlefsen, R. Köhn, J. Michaelis, and C. Bräuchle. Visualization of the self-assembly of silica nanochannels reveals growth mechanism. *Nature Nanotechnology*, 6(2):87–92, 2011.

[113] C. Sanchez, C. Boissière, D. Grosso, C. Laberty, and L. Nicole. Design, Synthesis, and Properties of Inorganic and Hybrid Thin Films Having Periodically Organized Nanoporosity. *Chem. Mater.*, 20(3):682–737, 2008.

[114] R. Fan, S. Huh, R. Yan, J. Arnold, and P. Yang. Gated proton transport in aligned mesoporous silica films. *Nat. Mater.*, 7(4):303–307, 2008.

[115] H. Luo, D. Wang, J. He, and Y. Lu. Magnetic Cobalt Nanowire Thin Films. *J. Phys. Chem. B*, 109(5):1919–1922, 2005.

[116] P. Yang, G. Wirnsberger, H. C. Huang, S. R. Cordero, M. D. McGehee, B. Scott, T. Deng, G. M. Whitesides, B. F. Chmelka, S. K. Buratto, and G. D. Stucky. Mirrorless Lasing from Mesostructured Waveguides Patterned by Soft Lithography. *Science*, 287(5452):465–467, 2000.

[117] Ohsuna T. Edura T. Wu, C.-W. and K. Kuroda. Orientational Control of Hexagonally Packed Silica Mesochannels in Lithographically Designed Confined Nanospaces. *Angew. Chem., Int. Ed.*, 46(28):5364–5368, 2007.

[118] Tatsumi N. Kataoka S. Daiguji, H. and A. Endo. One-Dimensional Alignment of SBA-15 Films in Microtrenches. *Langmuir*, 25(19):11221–11224, 2009.

[119] Xia Y. Kim, E. and G. M. Whitesides. Polymer microstructures formed by moulding in capillaries. *Nature*, 376(6541):581–584, 1995.

[120] M. Trau, N. Yao, E. Kim, Y. Xia, G. M. Whitesides, and I. A. Aksay. Microscopic patterning of orientated mesoscopic silica through guided growth. *Nature*, 390(6661):674–676, 1997.

[121] Firouzi A. Stucky G. D. Tolbert, S. H. and B. F. Chmelka. Magnetic Field Alignment of Ordered Silicate-Surfactant Composites and Mesoporous Silica. *Science*, 278(5336):264–268, 1997.

[122] H. Miyata and K. Kuroda. Preferred Alignment of Mesochannels in a Mesoporous Silica Film Grown on a Silicon (110) Surface. *J. Am. Chem. Soc.*, 121(33):7618–7624, 1999.

[123] H. Miyata, Y. Kawashima, M. Itoh, and M. Watanabe. Preparation of a Mesoporous Silica Film with a Strictly Aligned Porous Structure through a Sol-Gel Process. *Chem. Mater.*, 17(21):5323–5327, 2005.

[124] D. Zhao, J. Feng, Q. Huo, N. Melosh, G. H. Fredrickson, B. F. Chmelka, and G. D. Stucky. Triblock Copolymer Syntheses of Mesoporous Silica with Periodic 50 to 300 Angstrom Pores. *Science*, 279(5350):548–552, 1998.

[125] S. P. Naik, S. Yamakita, M. Ogura, and T. Okubo. Studies on mesoporous silica films synthesized using F127, a triblock co-polymer. *Microporous Mesoporous Mater.*, 75(1-2):51–59, 2004.

[126] B. Rühle, M. Davies, T. Lebold, C. Bräuchle, and T. Bein. Highly Oriented Mesoporous Silica Channels Synthesized in Microgrooves and Visualized with Single-Molecule Diffusion. *ACS Nano*, 6(3):1948–1960, 2012.

[127] H. Miyata and K. Kuroda. Formation of a Continuous Mesoporous Silica Film with Fully Aligned Mesochannels on a Glass Substrate. *Chem. Mater.*, 12(1):49–54, 1999.

[128] H. Miyata, T. Noma, M. Watanabe, and K. Kuroda. Preparation of Mesoporous Silica Films with Fully Aligned Large Mesochannels Using Nonionic Surfactants. *Chem. Mater.*, 14(2):766–772, 2002.

[129] T. Lebold, L. A. Mühlstein, J. Blechinger, M. Riederer, H. Amenitsch, R. Köhn, K. Peneva, K. Müllen, J. Michaelis, C. Bräuchle, and T. Bein. Tuning Single-Molecule Dynamics in Functionalized Mesoporous Silica. *Chemistry - A European Journal*, 15(7):1661–1672, 2009.

[130] T. Lebold, A. Schlossbauer, K. Schneider, L. Schermelleh, H. Leonhardt, T. Bein, and C. Bräuchle. Controlling The Mobility Of Oligonucleotides In The Nanochannels Of Mesoporous Silica. *Adv. Funct. Mater.*, 22(1):106–112, 2012.

[131] F. Feil, V. Cauda, T. Bein, and C. Bräuchle. Direct Visualization of Dye and Oligonucleotide Diffusion in Silica Filaments with Collinear Mesopores. *Nano Lett.*, 12(3):1354–1361, 2012.

[132] S. L. Burkett, S. D. Sims, and S. Mann. Synthesis of hybrid inorganic-organic mesoporous silica by co-condensation of siloxane and organosiloxane precursors. *Chem. Commun.*, 0(11):1367–1368, 1996.

[133] D. J. Macquarrie. Direct preparation of organically modified MCM-type materials. Preparation and characterisation of aminopropyl-MCM and 2-cyanoethyl-MCM. *Chem. Commun.*, 0(16):1961–1962, 1996.

[134] M. H. Lim and A. Stein. Comparative Studies of Grafting and Direct Syntheses of Inorganic-Organic Hybrid Mesoporous Materials. *Chem. Mater.*, 11(11):3285–3295, 1999.

[135] A. Zürner, J. Kirstein, M. Döblinger, C. Bräuchle, and T. Bein. Visualizing single-molecule diffusion in mesoporous materials. *Nature*, 450(7170):705–708, 2007.

[136] F. Feil, C. Jung, J. Kirstein, J. Michaelis, C. Li, F. Nolde, K. Müllen, and C. Bräuchle. Diffusional and orientational dynamics of various single terylene diimide conjugates in mesoporous materials. *Microporous Mesoporous Mater.*, 125(1-2):70 – 78, 2009.

[137] C. Jung, J. Kirstein, B. Platschek, T. Bein, M. Budde, I. Frank, K. Müllen, J. Michaelis, and C. Bräuchle. Diffusion of Oriented Single Molecules with Switchable Mobility in Networks of Long Unidimensional Nanochannels. *J. Am. Chem. Soc.*, 130(5):1638–1648, 2008.

[138] E. Limpert, W. A. Stahel, and M. Abbt. Log-normal Distributions across the Sciences: Keys and Clues. *Bioscience*, 51(5):341–352, 2001.

[139] F. O. Holtrup, G. R. J. Müller, H. Quante, S. De Feyter, F. C. De Schryver, and K. Müllen. Terrylenimides: New NIR Fluorescent Dyes. *Chemistry - A European Journal*, 3(2):219–225, 1997.

[140] C. Hellriegel, J. Kirstein, and C. Bräuchle. Tracking of single molecules as a powerful method to characterize diffusivity of organic species in mesoporous materials. *New Journal of Physics*, 7(1):23, 2005.

[141] C. Hellriegel, J. Kirstein, C. Bräuchle, V. Latour, T. Pigot, R. Olivier, S. Lacombe, R. Brown, V. Guieu, C. Payrastre, A. Izquierdo, and P. Mocho. Diffusion of Single Streptocyanine Molecules in the Nanoporous Network of Sol-Gel Glasses. *J. Phys. Chem. B*, 108(38):14699–14709, 2004.

[142] V. Sharma, M. Dhayal, Govind, S.M. Shivaprasad, and S.C. Jain. Surface characterization of plasma-treated and peg-grafted pdms for micro fluidic applications. *Vacuum*, 81(9):1094–1100, 2007.

[143] C. Duez, C. Ybert, C. Clanet, and L. Bocquet. Making a splash with water repellency. *Nat Phys*, 3(3):180–183, 2007.

[144] P. N. Nge, J. V. Pagaduan, M. Yu, and A. T. Woolley. Microfluidic chips with reversed-phase monoliths for solid phase extraction and on-chip labeling. *Journal of Chromatography A*, 1261(0):129–135, 2012.

[145] D. Sun, F. Wang, K. Wu, J. Chen, and Y. Zhou. Electrochemical determination of hesperidin using mesoporous SiO2 modified electrode. *Microchimica Acta*, 167(1-2):35–39, 2009.

[146] J. Zhao, W. Huang, and X. Zheng. Mesoporous silica-based electrochemical sensor for simultaneous determination of honokiol and magnolol. *Journal of Applied Electrochemistry*, 39(12):2415–2419–, 2009.

[147] C. Zhou, Z. Liu, Y. Dong, and D. Li. Electrochemical Behavior of o-Nitrophenol at Hexagonal Mesoporous Silica Modified Carbon Paste Electrodes. *Electroanalysis*, 21(7):853–858, 2009.

[148] P. Alexandridis and T. A. Hatton. Poly(ethylene oxide)-poly(propylene oxide)-poly(ethylene oxide) block copolymer surfactants in aqueous solutions and at interfaces: thermodynamics, structure, dynamics, and modeling. *Colloids and Surfaces A: Physicochemical and Engineering Aspects*, 96(1–2):1 – 46, 1995.

[149] M. Almgren, W. Brown, and S. Hvidt. Self-aggregation and phase behavior of poly(ethylene oxide)-poly(propylene oxide)-poly(ethylene oxide) block copolymers in aqueous solution. *Colloid and Polymer Science*, 273:2–15, 1995.

[150] G. Wanka, H. Hoffmann, and W. Ulbricht. Phase Diagrams and Aggregation Behavior of Poly(oxyethylene)-Poly(oxypropylene)-Poly(oxyethylene) Triblock Copolymers in Aqueous Solutions. *Macromolecules*, 27(15):4145–4159, 1994.

[151] A. Galarneau, H. Cambon, F. Di Renzo, R. Ryoo, M. Choi, and F. Fajula. Microporosity and connections between pores in SBA-15 mesostructured silicas as a function of the temperature of synthesis. *New Journal of Chemistry*, 27(1):73–79, 2003.

[152] O. C. Gobin, Y. Wan, D. Zhao, F. Kleitz, and S. Kaliaguine. Mesostructured Silica SBA-16 with Tailored Intrawall Porosity Part 1: Synthesis and Characterization. *Journal of Physical Chemistry C*, 111(7):3053–3058, 2007.

[153] V. Kocherbitov and V. Alfredsson. Assessment of Porosities of SBA-15 and MCM-41 Using Water Sorption Calorimetry. *Langmuir*, 27(7):3889–3897, 2011.

[154] M. Kruk, M. Jaroniec, C. H. Ko, and R. Ryoo. Characterization of the Porous Structure of SBA-15. *Chemistry of Materials*, 12(7):1961–1968, 2000.

[155] P. I. Ravikovitch and A. V. Neimark. Characterization of Micro- and Mesoporosity in SBA-15 Materials from Adsorption Data by the NLDFT Method. *Journal of Physical Chemistry B*, 105(29):6817–6823, 2001.

[156] R. Ryoo, C. H. Ko, M. Kruk, V. Antochshuk, and M. Jaroniec. Block-Copolymer-Templated Ordered Mesoporous Silica: Array of Uniform Mesopores or Mesopore-Micropore Network. *Journal of Physical Chemistry B*, 104(48):11465–11471, 2000.

[157] C. Kohl, T. Weil, J. Qu, and K. Müllen. Towards Highly Fluorescent and Water-Soluble Perylene Dyes. *Chemistry - A European Journal*, 10(21):5297–5310, 2004.

[158] R. Kolesov, B. Grotz, G. Balasubramanian, R. J. Stohr, A. A. L. Nicolet, P. R. Hemmer, F. Jelezko, and J. Wrachtrup. Wave-particle duality of single surface plasmon polaritons. *Nature Physics*, 5(7):470–474, 2009.

[159] W. L. Barnes, A. Dereux, and T. W. Ebbesen. Surface plasmon subwavelength optics. *Nature*, 424(6950):824–830, 2003.

[160] E. Ozbay. Plasmonics: Merging photonics and electronics at nanoscale dimensions. *Science*, 311(5758):189–193, 2006.

[161] L. Novotny. Effective wavelength scaling for optical antennas. *Physical review letters*, 98(26), 2007.

[162] P. Mohanty, I. Yoon, T. Kang, K. Seo, K. S. Varadwaj, W. Choi, Q. H. Park, J. P. Ahn, Y. D. Suh, H. Ihee, and B. Kim. Simple vapor-phase synthesis of single-crystalline ag nanowires and single-nanowire surface-enhanced raman scattering. *Journal of the American Chemical Society*, 129(31):9576–7, 2007.

[163] J. M. Baik, S. J. Lee, and M. Moskovits. Polarized surface-enhanced raman spectroscopy from molecules adsorbed in nano-gaps produced by electromigration in silver nanowires. *Nano Letters*, 9(2):672–676, 2009.

[164] Y. R. Fang, H. Wei, F. Hao, P. Nordlander, and H. X. Xu. Remote-excitation surface-enhanced raman scattering using propagating ag nanowire plasmons. *Nano Letters*, 9(5):2049–2053, 2009.

[165] I. Yoon, T. Kang, W. Choi, J. Kim, Y. Yoo, S. W. Joo, Q. H. Park, H. Ihee, and B. Kim. Single nanowire on a film as an efficient sers-active platform. *Journal of the American Chemical Society*, 131(2):758–762, 2009.

[166] J. C. Ashley and L. C. Emerson. Dispersion-relations for non-radiative surface plasmons on cylinders. *Surface Science*, 41(2):615–618, 1974.

[167] J. Takahara, S. Yamagishi, H. Taki, A. Morimoto, and T. Kobayashi. Guiding of a one-dimensional optical beam with nanometer diameter. *Optics Letters*, 22(7):475–477, 1997.

[168] J. C. Weeber, A. Dereux, C. Girard, J. R. Krenn, and J. P. Goudonnet. Plasmon polaritons of metallic nanowires for controlling submicron propagation of light. *Physical Review B*, 60(12):9061–9068, 1999.

[169] R. M. Dickson and L. A. Lyon. Unidirectional plasmon propagation in metallic nanowires. *Journal of Physical Chemistry B*, 104(26):6095–6098, 2000.

[170] J. R. Krenn, B. Lamprecht, H. Ditlbacher, G. Schider, M. Salerno, A. Leitner, and F. R. Aussenegg. Non diffraction-limited light transport by gold nanowires. *Europhysics Letters*, 60(5):663–669, 2002.

[171] B. J. Murray, Q. Li, J. T. Newberg, J. C. Hemminger, and R. M. Penner. Silver oxide microwires: Electrodeposition and observation of reversible resistance modulation upon exposure to ammonia vapor. *Chemistry of Materials*, 17(26):6611–6618, 2005.

[172] S. E. Brunker, K. B. Cederquist, and C. D. Keating. Metallic barcodes for multiplexed bioassays. *Nanomedicine*, 2(5):695–710, 2007.

[173] S. L. Pan and L. J. Rothberg. Enhancement of platinum octaethyl porphyrin phosphorescence near nanotextured silver surfaces. *Journal of the American Chemical Society*, 127(16):6087–6094, 2005.

[174] S. L. Pan, Z. J. Wang, and L. J. Rothberg. Enhancement of adsorbed dye monolayer fluorescence by a silver nanoparticle overlayer. *Journal of Physical Chemistry B*, 110(35):17383–17387, 2006.

[175] S. H. Guo, D. G. Britti, J. J. Heetderks, H. C. Kan, and R. J. Phaneuf. Spacer layer effect in fluorescence enhancement from silver nanowires over a silver film; switching of optimum polarization. *Nano Letters*, 9(7):2666–2670, 2009.

[176] A. V. Akimov, A. Mukherjee, C. L. Yu, D. E. Chang, A. S. Zibrov, P. R. Hemmer, H. Park, and M. D. Lukin. Generation of single optical plasmons in metallic nanowires coupled to quantum dots. *Nature*, 450(7168):402–406, 2007.

[177] C. Grillet, C. Monat, C. L. C. Smith, B. J. Eggleton, D. J. Moss, S. Frederick, D. Dalacu, P. J. Poole, J. Lapointe, G. Aers, and R. L. Williams. Nanowire coupling to photonic crystal nanocavities for single photon sources. *Optics Express*, 15(3):1267–1276, 2007.

[178] Z. Y. Fang, L. R. Fan, C. F. Lin, D. Zhang, A. J. Meixner, and X. Zhu. Plasmonic coupling of bow tie antennas with ag nanowire. *Nano Letters*, 11(4):1676–1680, 2011.

[179] L. A. Peyser, A. E. Vinson, A. P. Bartko, and R. M. Dickson. Photoactivated fluorescence from individual silver nanoclusters. *Science*, 291(5501):103–106, 2001.

[180] D. A. Clayton, D. M. Benoist, Y. Zhu, and S. L. Pan. Photoluminescence and spectroelectrochemistry of single ag nanowires. *Acs Nano*, 4(4):2363–2373, 2010.

[181] B. Wild, L. Cao, Y. Sun, B. P. Khanal, E. R. Zubarev, S. K. Gray, N. F. Scherer, and M. Pelton. Propagation lengths and group velocities of plasmons in chemically synthesized gold and silver nanowires. *Acs Nano*, 6(1):472–482, 2011.

[182] R. L. Zong, J. Zhou, Q. Li, B. Du, B. Li, M. Fu, X. W. Qi, L. T. Li, and S. Buddhudu. Synthesis and optical properties of silver nanowire arrays embedded in anodic alumina membrane. *Journal of Physical Chemistry B*, 108(43):16713–16716, 2004.

[183] N. R. Jana, L. Gearheart, and C. J. Murphy. Wet chemical synthesis of silver nanorods and nanowires of controllable aspect ratio. *Chemical Communications*, (7):617–618, 2001.

[184] Y. G. Sun, B. Gates, B. Mayers, and Y. N. Xia. Crystalline silver nanowires by soft solution processing. *Nano Letters*, 2(2):165–168, 2002.

[185] B. Wiley, Y. G. Sun, and Y. N. Xia. Synthesis of silver nanostructures with controlled shapes and properties. *Accounts of Chemical Research*, 40(10):1067–1076, 2007.

[186] K. K. Caswell, C. M. Bender, and C. J. Murphy. Seedless, surfactantless wet chemical synthesis of silver nanowires. *Nano Letters*, 3(5):667–669, 2003.

[187] R. Kötz and E. Yeager. Raman studies of the silver/silver oxide electrode. *Journal of Electroanalytical Chemistry and Interfacial Electrochemistry*, 111(1):105–110, 1980.

[188] T. Watanabe, O. Kawanami, K. Honda, and B. Pettinger. Evidence for surface Ag+ complexes as the sers-active sites on Ag electrodes. *Chemical Physics Letters*, 102(6):565–570, 1983.

[189] E. S. Brandt. Selective enhanced raman-scattering from an oxacarbocyanine dye and 1-phenyl-5-mercaptotetrazole adsorbed to silver and silver-halide surfaces in photographic films. *Applied Spectroscopy*, 47(1):85–93, 1993.

[190] X. Wang, H. Wen, T. J. He, J. Zuo, C. Y. Xu, and F. C. Liu. Enhancement mechanism of SERS from cyanine dyes adsorbed on Ag2O colloids. *Spectrochimica Acta Part a-Molecular and Biomolecular Spectroscopy*, 53(14):2495–2504, 1997.

[191] X. S. Xie. Single-molecule spectroscopy and dynamics at room temperature. *Accounts of Chemical Research*, 29(12):598–606, 1996.

[192] R. M. Dickson, A. B. Cubitt, R. Y. Tsien, and W. E. Moerner. On/off blinking and switching behaviour of single molecules of green fluorescent protein. *Nature*, 388(6640):355–358, 1997.

[193] A. P. Bartko and R. M. Dickson. Imaging three-dimensional single molecule orientations. *Journal of Physical Chemistry B*, 103(51):11237–11241, 1999.

[194] W. E. Moerner and M. Orrit. Illuminating single molecules in condensed matter. *Science*, 283(5408):1670–+, 1999.

[195] C. Scheu. Electron microscopy and analytical techniques. *Lecture, LMU München*, 2011.

[196] H. Chen, Y. Gao, H. Zhang, L. Liu, H. Yu, H. Tian, S. Xie, and J. Li. Transmission-electron-microscopy study on fivefold twinned silver nanorods. *The Journal of Physical Chemistry B*, 108(32):12038–12043, 2004.

[197] C. Damm, D. Segets, G. Yang, B. F. Vieweg, E. Spiecker, and W. Peukert. Shape transformation mechanism of silver nanorods in aqueous solution. *Small*, 7(1):147–156, 2011.

[198] X. Y. Wu and E. K. L. Yeow. Fluorescence blinking dynamics of silver nanoparticle and silver nanorod films. *Nanotechnology*, 19(3), 2008.

Acknowledgements

I want to express my great thanks to many people that have always accompanied and supported me during the last three years, and made this thesis possible.

First of all, I wish to thank my supervisor, Professor Christoph Bräuchle, for giving me the opportunity to work on this fascinating field of Nanoscience. During all this project he gave great advice and support to me. Without his motivation and the way he trust me, this work would have not been the same.

I am also especially grateful to my co-supervisor Professor Jens Michaelis for his expert knowledge, fruitful discussions and inspiration for new experiments.

In addition, I thank all collaborating group leaders I have been working with: Professor Thomas Bein, Professor Christina Scheu, Professor Klaus Müllen and Dr. Chen Li. It was very interesting, exciting and helpful to discuss with you.

I especially want to thank Bastian Rühle, who synthesized all mesoporous channels I was investigating in this work. He helped me so much during these years for many diverse things and it was always fun working in such close collaboration. Thank you also for the great 3D graphics in our papers.

I also want to thank Angela Wochnik for TEM measurements and searching the size of a pin in a haystack. Finally we found the right Ag-Nanowire.

I was privileged to share the office with Christophe Jung, Florian Feil, Timo Lebold, Stephan Mackowiak and Leonhard Möckl. Thank you guys for teaching me so many things and supporting me. I enjoyed each and every day working with you. Special thanks to Stephan Mackowiak for all the ideas and inspiration for new experiments, the fun we had in and outside the lab. It has been great working with you. Also special thanks to Frauke König, Julia Blechinger, Anna Sauer, Veronika Weiß, Ellen Broda and Adriano Torrano for being great colleagues and for the nice atmosphere that made working in this group a pleasure.

I further want to thank my students Philipp Wallis, Tobias Stürzer, Gergely Rozsa and Matthias Roos for the nice time we had while working on the projects.

Thanks to the entire Bräuchle, Michaelis, Lamb, Scheu, Bein group and especially to Silke Steger and Moritz Ehrl for all the bureaucratic procedures.

Words of special gratitude are addressed to my parents, Brychan and Eva, my brother Oliver, my granddad and all my family. Thank you for always supporting and believing in me.

List of Publications

Publications

Parts of this thesis have been published previously in somewhat modified form or are currently being prepared for publication:

- M. Davies, S. Goette, P. Klüfers and T. Schwarz. Methyl 4,6-O-benzylidene-2,3-dideoxy-3-hydroxyimino-α-D-erythropyranoside methanol solvate. *Acta Crystallogr.*, 63(E):4765, 2007.

- M. Davies, C. Jung, P. Wallis, T. Schnitzler, C. Li, K. Müllen, and C. Bräuchle. Photophysics of new photostable rylene derivatives: applications in single-molecule studies and membrane labelling. *Chemphyschem*, 12(8):1588–95, 2011.

- G. Battagliarin, M. Davies, S. Mackowiak, C. Li, and K. Müllen. Ortho-Functionalized Perylenediimides for Highly Fluorescent Water-Soluble Dyes. *Chemphyschem*,13 (4):923–926, 2012.

- B. Ruehle*, M. Davies*, T. Lebold, C. Bräuchle, and T. Bein. Highly Oriented Mesoporous Silica Channels Synthesized in Microgrooves and Visualized with Single–Molecule Diffusion. *ACS Nano*, 6(3):1948–1960, 2012.

- M. Davies*, A. Wochnik*, F. Feil*, C. Jung, C. Bräuchle, C. Scheu, and J. Michaelis, Synchronous Emission from Nanometric Silver Particles through Plasmonic Coupling on Silver Nanowires. *ACS Nano*, 6(7):6049–6057, 2012.

- B. Rühle*, M. Davies*, T. Bein, and C. Bräuchle, Fluorescence Microscopy Studies of Porous Silica Compounds, *Z. Naturforsch.* 68(b):1–22, 2013.

- M. Davies*, B. Rühle*, C. Li, K.Müllen, T. Bein, and C. Bräuchle, Electrophoresis of Single Dye Molecules in Highly Oriented Mesoporous Silica Channels, *JACS*, in preparation.

*These autors contributed equally.

Contributions to Conferences and Presentations

- Summer School of the International Doctorate Program NanoBioTechnology 2010, Aiterbach am Chiemsee, Germany.

- *Optical investigations of plasmons generated in silver nanowires and their influence on the emission of dye molecules*, 74rd Annual conference of the German Physical Society 2010, Universität Regensburg, Regensburg, Germany.

- *Oriented Mesoporous Silica Thin Films as Model Systems for Single Molecule Diffusion Studies*, 16th International Zeolith Conference 2010, Hilton Sorrento Palace, Sorrento, Italy.

- Summer Retreat of the Nanosystems Initative Munich (NIM) 2010, Herrsching, Germany.

- Winterschool of the Nanosystems Initative Munich (NIM) 2011, St. Christoph, Austria.

- *Investigation of Single Molecule Diffusion with Oriented Mesoporous Silica Thin Film Model Systems*, 22st German Zeolite Conference 2010, Ludwig-Maximilians-Universität München, Munich, Germany.

- *Single Molecule Investigations of Large Oriented Silica Mesoporous Channel Systems*, 23st German Zeolite Conference 2011, Friedrich-Alexander-Universität, Erlangen-Nürnberg, Germany.

- *Single Molecule Investigations of Large Oriented Microgrooves and Visualized with Single Molecule Diffusion*, CeNS Workshop 2011, Venice, Italy.

- Summer Retreat of the Nanosystems Initative Munich (NIM) 2011, Kampenwand, Germany.

Curriculum Vitae

Personal Information

Name:	Eva Melari Davies
Date of Birth:	15th of October 1985
Place of Birth:	Munich
Citizenship:	German

Education

01/2010 – 07/2013	PhD in physical chemistry in the group of Prof. Dr. C. Bräuchle, LMU Munich, Germany
10/2007 – 11/2009	M. Sc. in chemistry, LMU Munich, Germany
10/2004 – 10/2007	B. Sc. in chemistry and biochemistry, LMU Munich, Germany
09/1995 – 06/2004	Christoph–Probst Gymnasium (secondary school), Gilching, Germany

Awards and scholarschips

2012	CeNS publication award for: M. Davies, A. Wochnik, F. Feil, C. Jung, C. Bräuchle, C. Scheu, and J. Michaelis, Synchronous Emission from Nanometric Silver Particles through Plasmonic Coupling on Silver Nanowires. *ACS Nano*, 6(7):6049–6057, 2012.
2010	Römer prize of the faculty of chemistry for the master thesis, LMU Munich
2010 – 2013	Funded by the International Doctorate Program NanoBioTechnology (IDK–NBT)
2010 – 2013	Funded by the cluster of excellence Nanosystems Initiative Munich (NIM)
2007 – 2010	Refund of university tuition fees due to belonging to the 10% best graduates of the fall semester 2009/2010 of the masters course